![USGS logo: science for a changing world]

Questa Baseline and Pre-Mining Ground-Water-Quality Investigation. 12. Geochemical and Reactive-Transport Modeling Based on Tracer Injection-Synoptic Sampling Studies for the Red River, New Mexico, 2001-2002

Scientific Investigations Report 2005-5149

Prepared in cooperation with the
New Mexico Environment Department

U.S. Department of the Interior
U.S. Geological Survey

Questa Baseline and Pre-Mining Ground-Water-Quality Investigation. 12. Geochemical and Reactive-Transport Modeling Based on Tracer Injection-Synoptic Sampling Studies for the Red River, New Mexico, 2001-2002

By James W. Ball, Robert L. Runkel, and D. Kirk Nordstrom

U.S. Department of the Interior
U.S. Geological Survey

U.S. Department of the Interior
Gale A. Norton, Secretary

U.S. Geological Survey
P. Patrick Leahy, Acting Director

U.S. Geological Survey, Boulder, Colorado: 2005

Contents

Figures

Tables

Conversion Factors

SI to Inch/Pound

Multiply	By	To obtain
Length		
kilometer (km)	0.6214	mile (mi)
meter (m)	3.281	foot (ft)
centimeter (cm)	0.3937	inch (in.)
millimeter (mm)	0.03937	inch (in.)
Area		
square kilometer (km^2)	247.1	acre
square kilometer (km^2)	0.3861	square mile (mi^2)
square meter (m^2)	10.76	square foot (ft^2)
square centimeter (cm^2)	0.1550	square inch (ft^2)
Volume		
cubic meter (m^3)	35.31	cubic foot (ft^3)
cubic meter (m^3)	264.2	gallon (gal)
liter (L)	0.2642	gallon (gal)
liter (L)	1.057	quart (qt)
liter (L)	33.82	ounce, fluid (fl. oz)
cubic centimeter (cm^3)	0.06102	cubic inch (in^3)
Flow rate		
cubic meter per second (m^3/s)	35.31	cubic foot per second (ft^3/s)
cubic meter per second (m^3/s)	22.83	million gallons per day (Mgal/d)
liter per second (L/s)	15.85	gallon per minute (gal/min)
Mass		
ton, short (2,000 lb)	0.9072	metric tom
kilogram (kg)	2.205	pound avoirdupois (lb)
gram (g)	0.03527	ounce, avoirdupois (oz)

Temperature in degrees Celsius (°C) may be converted to degrees Fahrenheit (°F) as follows:
$$°F=(1.8×°C)+32$$
Vertical coordinate information is referenced to the National Geodetic Vertical Datum of 1929 (NGVD 29)
Horizontal coordinate information is referenced to North American Datum of 1927 (NAD 27)
Altitude, as used in this report, refers to distance above the vertical datum.
Specific conductance is given in microSiemens per centimeter at 25 degrees Celsius (μS/cm at 25°C).

Abbreviations used in this report:

AE	algebraic equation
cm	centimeter
DIC	dissolved inorganic carbon
DOC	dissolved organic carbon
ft^3/s	cubic feet per second
g/s	grams per second
H_T^+	total excess hydrogen
h	hour
HFO	hydrous ferric oxide
ICP	inductively-coupled plasma
km	kilometer
km^2	square kilometer
log	common logarithm
m	meter
m^3/s	cubic meters per second
mg/L	milligrams per liter
mm	millimeter
MPV	most probable (median) value
μg/L	micrograms per liter
μm	micrometer
μS/cm	microsiemens per centimeter at 25 degrees Celsius
NMED	New Mexico Environment Department
NRP	National Research Program
PDE	partial differential equation
QC	quality control
QSP	quartz-sericite-pyrite
s	second
SI	saturation index
USGS	U.S. Geological Survey

Questa Baseline and Pre-Mining Ground-Water-Quality Investigation. 12. Geochemical and Reactive-Transport Modeling Based on Tracer Injection-Synoptic Sampling Studies for the Red River, New Mexico, 2001-2002

By James W. Ball, Robert L. Runkel, and D. Kirk Nordstrom

Abstract

Reactive-transport processes in the Red River, downstream from the town of Red River in north-central New Mexico, were simulated using the OTEQ reactive-transport model. The simulations were calibrated using physical and chemical data from synoptic studies conducted during low-flow conditions in August 2001 and during March/April 2002. Discharge over the 20-km reach from the town of Red River to the USGS streamflow-gaging station near the town of Questa ranged from 395 to 1,180 L/s during the 2001 tracer and from 234 to 421 L/s during the 2002 tracer. The pH of the Red River ranged from 7.4 to 8.5 during the 2001 tracer and from 7.1 to 8.7 during the 2002 tracer, and seep and tributary samples had pH values of 2.8 to 9.0 during the 2001 tracer and 3.8 to 7.2 during the 2002 tracer.

Mass-loading calculations allowed identification of several specific locations where elevated concentrations of potential contaminants entered the Red River. These locations, characterized by features on the north side of the Red River that are known to be sources of low-pH water containing elevated metal and sulfate concentrations, are: the initial 2.4 km of the study reach, including Bitter Creek, the stream section from 6.2 to 7.8 km, encompassing La Bobita well and the Hansen debris fan, Sulphur Gulch, at about 10.5 km, the area near Portal Springs, from 12.2 to 12.6 km, and the largest contributors of mass loading, the 13.7 to 13.9 km stream section near Cabin Springs and the 14.7 to 17.5 km stream section from Shaft Spring to Thunder Bridge, Goathill Gulch, and Capulin Canyon.

Speciation and saturation index calculations indicated that although solubility generally limits the concentration of aluminum above pH 5.0, at pH values above 7 and aluminum concentrations below 0.3 mg/L inorganic speciation and mineral solubility controls no longer dominate and aluminum-organic complexing may occur.

The August 2001 reactive-transport simulations included dissolved iron(II) oxidation, constrained using measured concentrations of dissolved iron(II) and dissolved iron(total). Both simulations included precipitation of amorphous $Al(OH)_3$ and hydrous ferric oxide as $Fe(OH)_3$, and sorption of copper and zinc to the precipitated hydrous ferric oxide. Simulations revealed that hydrogen, iron, aluminum, copper, and zinc were non-conservative and that mineral precipitation can account for iron and aluminum concentrations. Copper and zinc concentrations can be accounted for by simulating their sorption to hydrous ferric oxide forming in the water column of the Red River, although hydrous manganese oxides also may be important sorption substrates.

INTRODUCTION

Molycorp, Inc. operates a molybdenum mine east of the town of Questa, northern New Mexico, in the Red River Valley (fig. 1). The Red River approximates the southern boundary of the mine site and flows from east to west where it joins the Rio Grande. Molycorp is subject to New

Mexico's mine closure regulations and operates in a highly mineralized area likely to have solute concentrations greater than existing ground-water quality standards. The Water Quality Act, under the jurisdiction of the New Mexico Water Quality Control Commission, requires an operator to develop and complete an approved closure plan that prevents the exceedence of (1) ground-water quality standards set forth in New Mexico Water Quality Control Commission Regulations (§20.6.2.3103 NMAC) or (2) background concentrations. Although Molycorp installed production wells in the mid-1960's to support milling operations, no water-chemistry data were reported until 1992. Consequently, there are no pre-mining ground-water analyses and pre-mining water quality must be inferred (Nordstrom, 2002). In April 2001, the U.S. Geological Survey (USGS) and the New Mexico Environment Department began a cooperative study to infer the pre-mining ground-water chemistry at the Molycorp molybdenum mine site in the Red River Valley (fig. 1).

Tracer-injection studies with synoptic sampling were performed in August 2001 and in March/April 2002. These two studies provide the most quantitative information yet obtained on ground-water inflows to the Red River. Data from these studies can be used to simulate reactive transport in the Red River.

Reactive-transport modeling integrates the processes of ground- and surface-water inflow to, and in-stream chemistry of, the receiving stream. Reactive-transport modeling can establish a quantitative framework for mixing of tributaries with the Red River from both mined and unmined watersheds in the Red River valley and resulting in-stream processes. Such processes include mixing with inflowing surface and ground water, oxidation and reduction, adsorption and desorption, and mineral precipitation and dissolution. These reactions are constrained by chemical thermodynamics, fluid flow, and mixing properties for water in a mountain stream setting.

Purpose and Scope

The purpose of this report is to present results of aluminum geochemical speciation modeling calculations using the WATEQ4F speciation code (Ball and Nordstrom, 1991), including detailed examination of the hypothesis of a solubility control for aluminum at pH $\geq$ 4.5, and reactive-transport modeling simulations using physical and chemical data from two tracer-injection/synoptic-sampling studies conducted in August 2001 and in March/April 2002. The physical and chemical data used as input to the computer code were documented and discussed in a separate report (McCleskey and others, 2003. The WATEQ4F, OTIS (Runkel, 1998), and OTEQ (Runkel and others, 1996a) computer codes were used for the simulations because (1) they have a long history of research and development, (2) they have citable documentation in the scientific literature, and (3) they have been applied many times to the chemical speciation and transport of metal contaminants in mountain stream environments.

Mass-loading calculations were used to determine possible ground-water and tributary stream sources, and geochemical speciation modeling was done to determine aluminum speciation and saturation indices. These data were needed to guide the reactive-transport modeling.

Physical Setting

The Red River is located in Taos County in north-central New Mexico (fig. 1). The terrain is rugged and altered with steep slopes and V-shaped valleys. The main area of study within the Red River Valley extends from the town of Red River to USGS streamflow-gaging station number 08265000 (Red River near Questa) and includes approximately 163 km^2 of the drainage basin and approximately 20 km of river reach. The Molycorp, Inc. Questa molybdenum mine, referred to as the mine site, is located east of the Ranger Station on the north side of State Highway No. 38 and the Red River. The mine site is approximately 16 km^2 in area (U.S. Department of Agriculture Forest Service, 2001), and encompasses three tributary valleys to the Red River: Capulin Canyon, Goathill Gulch, and Sulphur Gulch, from west to east, respectively (fig. 1).
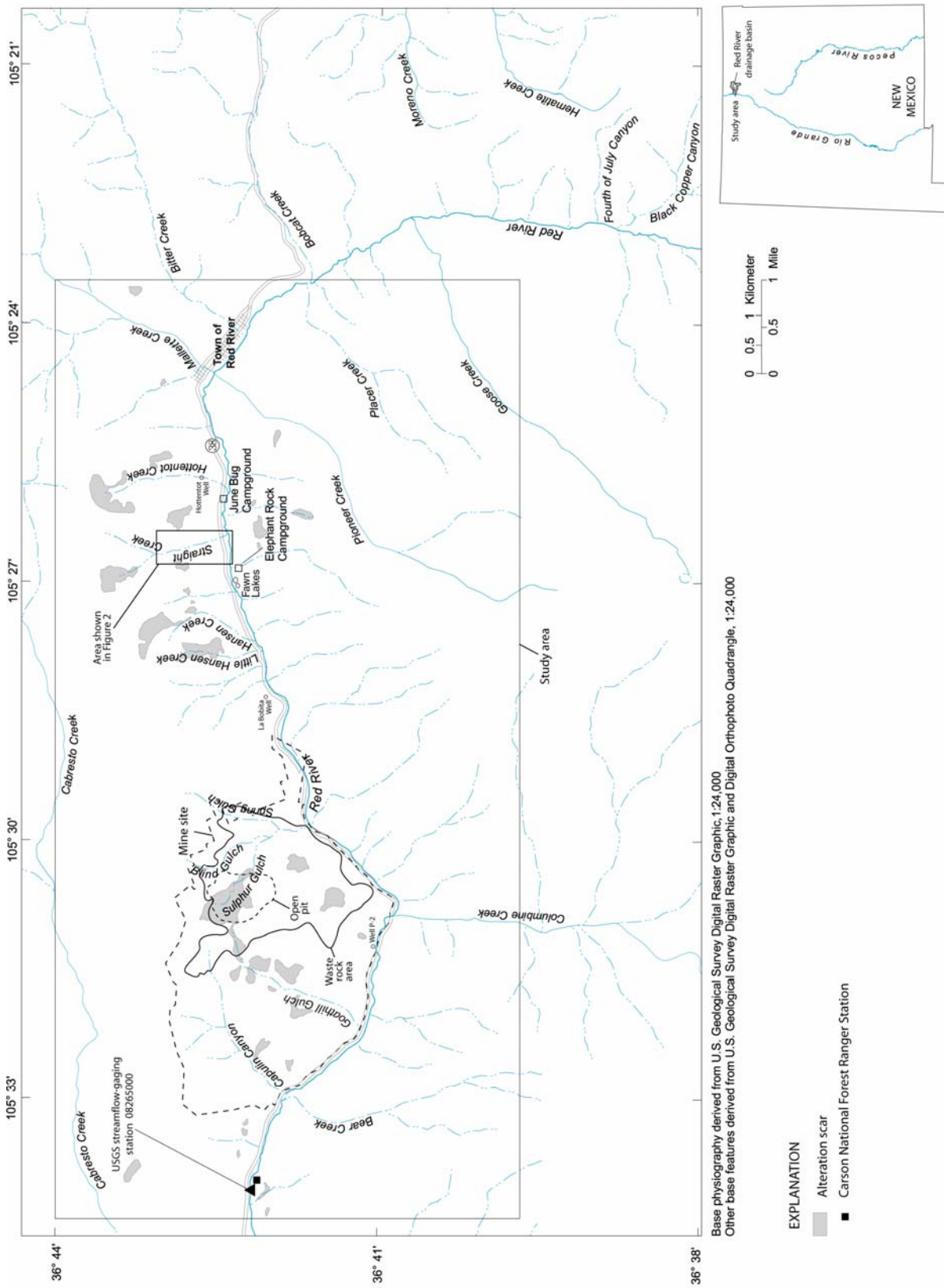
Figure 1. Location of the Questa mine site, drainages sampled, and study area within the Red River basin.

Mining activities produced extensive underground workings and an open pit approximately 914 m in diameter (covering approximately 0.66 km^2) near or in Sulphur Gulch (URS, 2001). Waste-rock piles cover steep slopes on the north side of the Red River between Capulin Canyon and Spring Gulch (a tributary valley of Sulphur Gulch). Hydrothermally altered bedrock is found in the Capulin, Goathill, Sulphur, Hansen, Straight, and Hottentot drainages (fig. 1). Weathering of extensively altered rock has resulted in steep, highly erosive, sparsely vegetated "scars" that are clearly visible from the ground and in aerial photographs.

Climate and Vegetation

The Red River Valley is located within a semi-arid desert that receives precipitation throughout the year and sustains moderate biodiversity. Between 1915 and 2004, the annual average temperature was 4 °C and the annual average precipitation and snowfall were approximately 52.1 and 371 cm, respectively. Daily temperatures generally fluctuated by 18 °C throughout the year (Western Regional Climate Center, 2005; Station 297323, elevation 2646 m, located at N 36° 42', W 105° 24').

Climate and vegetation vary greatly within short distances, primarily because of differences in topography. Topography in the study area is steep, rising rapidly from the basin floor altitude of approximately 2,270 m at the streamflow-gaging station near Questa to ridge crests at altitudes exceeding 3,200 m. Orographic effects of mountainous topography lead to precipitation on the windward slopes and localized storms within tributary valleys. Runoff from thunderstorms is responsible for mass wasting in hydrothermally altered areas, producing debris flows that form debris fans at the mouths of most tributaries to the Red River (K. Vincent, USGS, written commun., 2003). Winter snowpack contributes to ground-water recharge through infiltration during snowmelt, usually occurring during March/April.

Prevalent vegetation in the Red River Valley is representative of the following altitude zones: piñon-juniper woodland (1,830 to 2,290 m in altitude), mixed conifer woodland (2,290 to 2,740 m in altitude), and spruce-fir woodland (2,740 to 3,660 m in altitude) (Knight, 1990).

Willows, cottonwoods, shrubs, perennial grasses, and flowering vegetation are common near the banks of the Red River. Widely spaced piñon pines and junipers extend upslope from the river. Gains in altitude give rise to an abundance of ponderosa and limber pines, while douglas and white fir also are found at higher altitudes. This typical mountain community, while diverse, is dominated by ponderosa pines (L. Gough, USGS, oral commun., 2003).

Hydrogeology

Ground water passes through, and geochemically interacts with, various earth materials in the Red River Valley. Major rock types, minerals, and water-bearing units in the valley and generalized aquifer and ground-water-chemistry information are described in this section. The geology and mineralogy of the Red River Valley have been described by Schilling (1956), Rehrig (1969), Lipman (1981), Meyer (1991), and Meyer and Leonardson (1990; 1997). Information in this section draws largely upon these sources, with additional information from Ludington and others (2004) and other USGS scientists participating in this study.

The Red River Valley is located along the southern edge of the Questa caldera and contains complex structural features (Caine, 2003) and extensive hydrothermal alteration. Volcanic and intrusive rocks of Tertiary age are underlain by metamorphic rocks of Precambrian age that were intruded by granitic stocks in the basin. The volcanic rocks have primarily intermediate to felsic composition (andesite to rhyolite); granitic and porphyritic intrusions in the volcanics are the apparent source of hydrothermal fluids and molybdenite mineralization.

The mineral deposits in the Red River Valley are considered Climax-type deposits that are associated with silica- and fluorine-rich rhyolite porphyry and granitic intrusives. Climax-type hydrothermal alteration produces zones of alteration assemblages with a central zone of fluorine-rich potassic alteration, a quartz-sericite-pyrite (QSP) zone (often with a carbonate-fluorite veinlet overprint), and a propylitic zone. In the potassic zone, rocks are altered to a mixture of biotite, potassium feldspar, quartz, fluorite, and molybdenite; these rocks usually contain less than 3 percent sulfide, including molybdenite. QSP

alteration, as the name implies, produces a mixture of quartz, pyrite (up to 10 percent), and fine-grained mica (sericite) or illite. Chlorite, epidote, albite, and calcite typically are found in the propylitic assemblages.

Ore deposits in the Red River Valley contain quartz, molybdenite, pyrite, fluorite, calcite, manganiferous calcite, dolomite, and rhodochrosite. Lesser amounts of galena, sphalerite, chalcopyrite, magnetite, and hematite also are present. The hydrothermal alteration related to mineralization overprints an older, regional, propylitic alteration. In these areas, rocks can contain a mixture of quartz, pyrite, and illite clays replacing feldspars, chlorite, carbonates, and epidote. Abundant minerals in waste rock produced by mining activities include chlorite, gypsum, illite, illite-smectite, jarosite, kaolinite, and muscovite (Gale and Thompson, 2001).

Andesite volcanic and volcaniclastic rocks are present in most scar-area bedrock outcrops, rhyolitic tuffs, quartz latites, and rhyolite porphyries. The dominant alteration type in all scars is QSP; carbonate minerals also are found in all scar areas. Most of the andesite and quartz latites have been propylitically altered and contain plagioclase feldspar and chlorite, with fewer QSP alteration minerals. Rhyolite porphyries and tuffs do not appear to have been substantially affected by propylitization. In Straight Creek, unweathered bedrock exposed in the creek bottom is propylitized andesite with a QSP overprint. Other dominant rock types include rhyolite porphyries and rhyolitic tuffs. Depending on location within the weathering profile, altered rocks contain variable amounts of quartz, illite, chlorite, and plagioclase feldspar, with smaller amounts of pyrite, gypsum, rutile, jarosite, and goethite (Livo and Clark, 2002; Ludington and others, 2004).

There are four main types of water-bearing units present in the Red River Valley: fractured bedrock, waste rock piles, debris-flow deposits, and Red River alluvium. Bedrock constitutes the largest aquifer in the study area in terms of rock mass, but probably contains only small amounts of ground water because of low porosity and hydraulic conductivity that are controlled by fractures. Although debris-flow deposits and Red River alluvium are restricted in areal extent and thickness compared to bedrock

aquifers, they contain most of the ground water in the valley. Waste rock piles and scars with associated debris fans are geochemically reactive and have high porosity and a fast rate of infiltration.

Debris fans are composed of sediments transported from watersheds tributary to the Red River. Where the tributary watersheds contain scars, the debris fans are large and active and contain both coarse- and fine-grained debris-flow sediments. The chemistry of these sediments reflects the chemistry of their rapidly eroding and altered erosion scars. In contrast, alluvial sediments deposited by the Red River consist of well washed, rounded sands, gravels, and cobbles and are composed of a mix of the lithologies found in the entire Red River Basin. The Red River aggraded behind the largest debris fans during the Quaternary Period. Thus shallow ground water likely flows alternately through Red River alluvium and debris fan deposits (K. Vincent, USGS, written commun., 2003). Debris fans and the Red River alluvium are less than 1,000 feet (305 m) wide and less than 200 feet (61 m) thick (K. Vincent, USGS, written commun., 2003).

Although chemical analyses of ground-water were not obtained prior to mining in the Red River Valley, substantial amounts of historical ground-water data collected after mining was initiated are available (LoVetere and others, 2004). Most wells developed in the Red River Valley were installed to monitor water quality downgradient from mining operations (waste rock and tailings piles) and (or) scar areas. Bedrock, debris-flow, and alluvial ground waters are dominantly of the calcium-sulfate type.

Surface Water

The Red River originates at an altitude of approximately 3,660 m near Wheeler Peak and flows roughly 56 km to its confluence with the Rio Grande at an altitude of 2,010 m. Total basin drainage area is 492 km^2; the drainage area upstream from the Questa Ranger Station gaging station is 293 km^2. Peak streamflow usually occurs from late May to mid-June, with snowmelt-related flows beginning in late March and increasing through mid-April. Summer thunderstorms are prevalent in July and August. Between 1930 and 2001, the annual mean

discharge of the Red River at the Questa Ranger Station gage has ranged from 360 to 2,920 L/s, while the daily average discharge ranged from 71 to 21,200 L/s with an average of 1,330 L/s (U.S. Geological Survey, 2004).

The main drainages in the vicinity of the mine site are Capulin Canyon, Goathill Gulch, and Sulphur Gulch on the north side of the Red River (fig. 1). Upstream from the mine site on the north side of the Red River, Little Hansen, Hansen, Straight, Hottentot, and Bitter Creeks drain scar areas, whereas Mallette Creek drains a non-scar area. Figure 2 shows the Straight Creek drainage basin and the locations of monitoring wells installed as part of the study to determine off-site natural background ground-water chemistry. Placer, Pioneer, Columbine, and Bear Creeks drain largely unmineralized land on the south side of the river. Bear Creek and upper Pioneer Creeks contain some mineralization. Downstream from the mine site the Red River is joined by Cabresto Creek, entering from the north, before discharging to the Rio Grande.

Springs and shallow alluvial ground waters discharge to the Red River rendering it a gaining stream over much of its length (Smolka and Tague, 1989). Between the town of Red River and the gaging station near Questa, there are approximately 25 ephemeral seeps and springs along the banks of the Red River and approximately 20 intermittent seeps and springs in tributary drainages on the north side of the river (South Pass Resources, Inc., 1995a; 1995b; Steffen, Robertson, and Kirsten, 1995; Robertson GeoConsultants, Inc., 2000; 2001). Most seeps and springs are acidic (pH 2 to 4) with high conductance and elevated dissolved solids and metal concentrations. Aluminum hydroxide often precipitates following mixing of Red River water with water from springs downgradient from scar and mined areas on the north side of the Red River, affecting the color and turbidity of the river (Vail Engineering, Inc., 1989).

Mining History

Much of the information in this section was obtained from Molycorp, Inc. ([n.d.]) at *www.molycorp.com/*. Further history and related information on the Questa Molycorp Mine is available from the same Molycorp, Inc. web site and from the U.S. Environmental Protection Agency (USEPA; *www.epa.gov/superfund/sites/npl/nar1599.htm*).

Prior to 1916, prospectors discovered outcrops of rich yellow weathered rock that looked like sulfur (hence the name, Sulphur Gulch) and a greasy mineral that looked like graphite. The graphitic mineral was identified as molybdenite in 1916 and the yellow mineral as ferrimolybdite, an oxidized product derived from the weathering of molybdenite (Schilling, 1956). By 1920 the Molybdenum Corporation of America had acquired the property to mine the deposit. The company subsequently shortened its name to Molycorp, Incorporated. By 1923 a mill and flotation plant had been set up for production, and small-scale underground mining of high-grade veins (averaging 4 percent with a maximum of 35 percent molybdenite) continued until 1958. During the 1950s exploration geologists identified a large low-grade deposit (~0.3 percent molybdenite) below the high-grade deposit and the decision was made to extract this ore by open-pit methods. Extraction of open-pit ore began in 1965 and tailings were transported by a nine-mile-long pipeline to a tailings facility in the Rio Grande Valley just west of Questa. The peak molybdenite production of 5.23 million kg occurred in 1976. In 1977 Molycorp, Incorporated became a wholly-owned subsidiary of Union Oil Company of California.

Open-pit mining ceased in 1983 and a new phase of underground mining was initiated in Goathill Gulch. Waste rock was no longer dumped onto piles at the mine site but the volume of tailings slurry transported by pipeline to the tailings facility increased. Low market values for molybdenum during 1986 to 1989 and 1992 to 1995 caused mining operations to shut down. Presently, mining operations start and stop in response to market demand (Molycorp, Inc., [n.d.]).
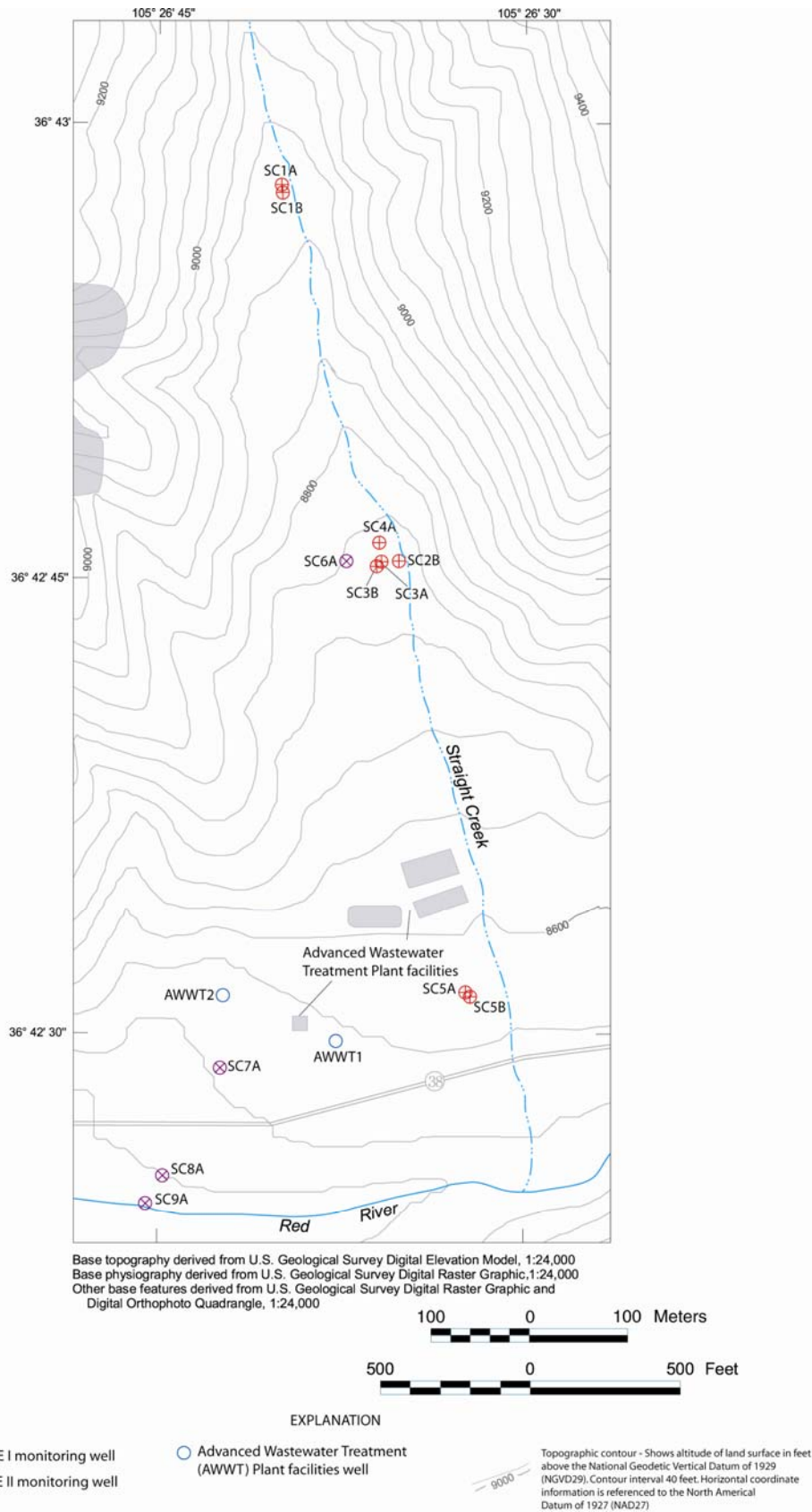
Figure 2. Location of monitoring wells within the Straight Creek basin.

METHODS

In August 2001, the Red River between the town of Red River and the Carson National Forest Questa Ranger Station (Ranger Station) was sampled in three sections. Three tracer injections at low flow were accomplished by pumping a concentrated NaBr solution into the Red River at a constant rate. After tracer concentrations in the stream reached steady state, synoptic samples were collected from 62 inflows and 95 stream sites along the three sections of the main stem of Red River. Similarly, in March/April 2002, the Red River was divided into three sections between the town of Red River and the Ranger Station, and three tracer injections were done in the same manner as described above. At the steady-state tracer concentration in the stream, synoptic samples were collected from 31 inflows and at 57 stream sites along the three sections of the main stem of Red River. Bromide concentrations from the six synoptic sampling events were used to determine stream discharge using the tracer-dilution method (Kilpatrick and Cobb, 1985). Analytical results from 2001 and 2002 synoptic samples were used for calibration of the OTEQ modeling code, a solute-transport framework that couples a one-dimensional transport model with a chemical-equilibrium submodel (Runkel and others, 1996a; 1996b; 1999).

Sampling Locations

The six tracer-injection/synoptic-sampling sections discussed above had lengths ranging from about 2.0 km to about 7.4 km. For the August 2001 tracer, the first (upper) section was 5.7 km of the Red River extending from the town of Red River downstream to Fawn Lakes, the second (middle) section was 7.4 km, extending from Fawn Lakes downstream to Columbine Creek, and the third (lower) section was 7.3 km, extending from Columbine Creek downstream to the USGS streamflow-gaging station at the Ranger Station (fig. 3). The sum of the three sections is greater than 20 km because the sections overlapped each other. For the March/April 2002 tracer, the first (upper) section was 2.0 km extending from upstream from Hottentot Creek downstream to Fawn Lakes, the second (middle) section was 4.9 km extending from Fawn Lakes to near Sulphur Gulch, and the third (lower) section was 6.5 km extending from Columbine Creek downstream to the USGS streamflow-gaging station at the Ranger Station (fig. 4). The sum of the distances for the three sections is less than 20 km because some sections of the Red River were not included in the March/April 2002 tracer-injection/synoptic-sampling study. Sampling locations and analytical results can be found in McCleskey and others (2003).

Measurement of Onsite Parameters

Instantaneous stream-flow measurements were made at selected sites on the main stem of the Red River using approved USGS methods (Buchanan and Somers, 1969). Stream temperature was measured onsite at the time of sample collection. For both the August 2001 and March/April 2002 tracer studies, grab samples were collected in half-gallon plastic bottles and transported to a nearby sample-processing station near Cabin Springs just downstream from Columbine Creek. Samples were filtered and preserved and the on-site field parameters specific conductance and pH were measured at the sample-processing station. A single set of calibrated meters was used to minimize variations that might occur among several measurement systems. The precision and accuracy of specific conductance and pH measurements were demonstrated to be within ± 5 percent (specific conductance) and ± 0.05 pH unit based on replicate measurements and frequent meter calibration checks and recalibrations. Additional

Figure 3. Map showing sampling locations for the August 2001 tracer.

9
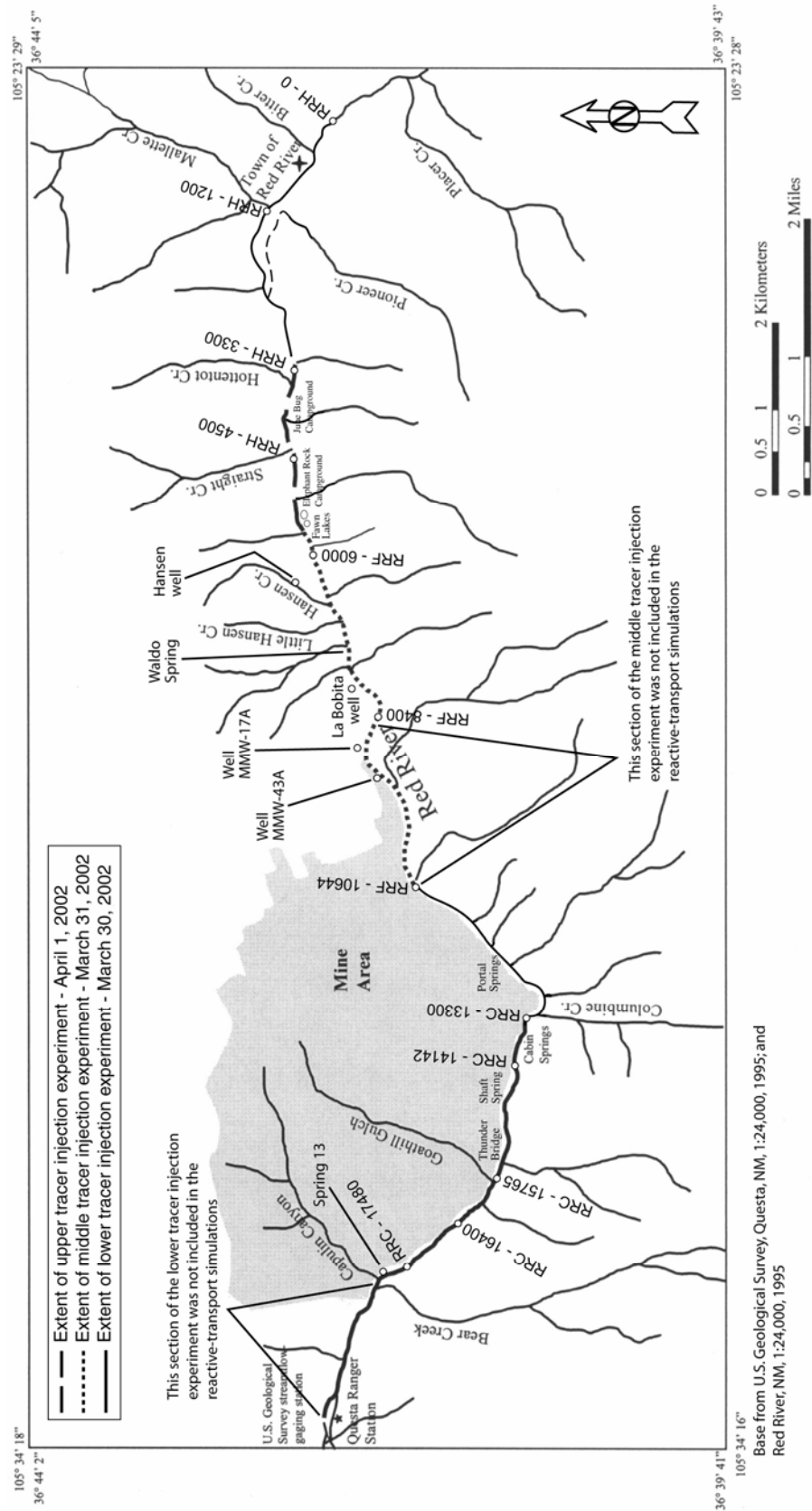
Figure 4. Map showing sampling locations for the March/April 2002 tracer.

details of sample collection and processing can be found in McCleskey and others (2003).

Water-Quality Parameters

Synoptic sample analyses included alkalinity, dissolved anions, dissolved iron(II), dissolved iron(total), and dissolved and total-recoverable metals. Dissolved iron(total) includes dissolved iron (II and III) species. At tributary sites, samples for determination of alkalinity and concentrations of dissolved anions, dissolved iron(II), dissolved iron(total), and dissolved metals were filtered through a 0.45-μm-pore-size tangential filter using a Minitan filtration apparatus. At main-stem sites, samples for determination of alkalinity and concentrations of dissolved anions and dissolved metals were filtered through a 0.45-μm-pore-size tangential filter using a Minitan filtration apparatus; in addition, subsamples for determination of dissolved iron(II), dissolved iron(total), and dissolved metals were filtered through a 10,000-Dalton tangential filter using a Minitan filtration apparatus. Concentrations determined on the 10,000-Dalton splits were not used for this study because a more consistent set of data was obtained for the 0.45-micron splits (see McCleskey and others (2004) for discussion of quality assurance/quality control considerations for this data set). In this report, the dissolved fraction of a sample is operationally defined as that portion of a whole water sample passing through a 0.45-μm-pore-size tangential filter. Total-recoverable metal concentrations represent dissolved-plus-suspended values determined by analyzing an unfiltered, acidified sample split. The suspended fraction of a sample is operationally defined as that portion of a whole water sample retained by the 0.45-μm-pore-size filter. Concentration in the suspended fraction is calculated by subtracting the dissolved concentration from the total-recoverable concentration. Filtered samples for dissolved metals and unfiltered samples for total-recoverable metals were acidified at the central sample-processing station to pH less than 2 with concentrated HNO_3. Filtered samples for dissolved iron(II) and dissolved iron(total) determinations were acidified to pH less than 2 with 6 M HCl. No preservative was added to samples for dissolved anions and alkalinity titrations.

Analytical Methods and Quality Control

Analytes, analytical methods, and operational detection limits are discussed by McCleskey and others (2003). Dissolved iron(II) and dissolved iron(total) were determined using a modification (To and others, 1999) of the FerroZine method of Stookey (1970). To ensure data validity, laboratory quality control (QC) samples were analyzed by the USGS analytical laboratory in Boulder, Colorado. These samples included method blanks, sample duplicates, and standard reference water samples. Laboratory QC samples were analyzed at a rate of one per 20 samples or one per analytical batch, whichever was the greater frequency, for all methods. Complete analytical results and descriptions of the analytical and quality control methods used for both tracer studies can be found in McCleskey and others (2003; 2004).

MASS LOADING FOR THE AUGUST 2001 TRACER STUDY

This discussion is limited to aspects of mass loading for the August 2001 tracer study that are applicable to the reactive-transport modeling. The term "loading ratio," used in this report, is the ratio of a constituent's output load to its input load, and is calculated by dividing a constituent's load at the downstream end of the study reach (output load) by its load at the upstream end of the study reach (input load). This simplified approach to mass loading differs from that of Kimball and others (written commun., 2005), who compared cumulative in-stream loads with cumulative inflow loads to indicate areas of the Red River where unsampled inflows were important, and identified locations where substantial gains and losses of load occurred in the main stem of the Red River by examining changes in instream loads. Mass-loading statistics are presented in table 1. A loading ratio of about 5 to 10 reflects no excessive inflow loading. Loading ratios (or component concentrations) near the same value for both dissolved and total-recoverable fractions are an indication that a component is likely behaving conservatively.

Reactive behavior is suggested by total-recoverable concentrations substantially greater than dissolved concentrations. Although reactive behavior, such as precipitation or sorption (to either suspended material or the stream bed), could masquerade as conservative behavior if solutes were being quantitatively removed from the water column shortly after their introduction, such complete removal appears unlikely based on the results of this study.

Data for the mass-loading plots (figs. 5 to 11) were smoothed by deleting values that were identified as analytical outliers (see McCleskey and others, 2003; 2004 for discussions of sources of analytical errors). Dissolved calcium (fig. 5), magnesium and sodium (table 1), and chloride (fig. 6) have loading ratios less than 10, suggesting that these four components are behaving conservatively and any gains or losses of load are not substantial. While the dissolved chloride loading ratio approaches 10, its concentration remains low, increasing only from about 1 mg/L to 3 mg/L.

Sulfate

Pyrite oxidation and gypsum dissolution are geochemical processes that have a substantial impact on the water quality of the Red River (Ludington and others, 2004; Naus and others, 2005). Because it is a signature component for both these processes, sulfate was selected for detailed examination. Dissolved sulfate (fig. 5) had a loading ratio of 22 (table 1), indicating that there are sources of substantial sulfate loading along the study reach. A closer look at figure 5 reveals that there are six locations where identifiable increases in sulfate mass loading occur:

- 0.375 km to 2.4 km (downstream from Bitter Creek, factor of 4 increase in load)
- 6.2 km to 7.8 km (downstream from Hansen debris fan, Waldo Spring, and La Bobita, a factor of 1.6 increase in load over this distance and a cumulative factor of 7 increase from 0.375 km)
- 10.5 km to 10.6 km (near Sulphur Gulch and the mill yard, a 13 percent increase in load over this distance and

a cumulative factor of 8 increase from 0.375 km)
- 12.2 km to 12.6 km (near Portal Springs, a 5 percent increase in load over this distance and a cumulative factor of 8.5 increase from 0.375 km)
- 13.7 km to 13.9 km (downstream from Cabin Springs, a 14 percent increase in load over this distance and a cumulative factor of 11 increase from 0.375 km)
- 14.7 km to 17.5 km (downstream from Shaft Spring and the Questa Mine head frame shaft, near Thunder Bridge and Goathill Gulch, a 78 percent increase in load over this distance and a cumulative factor of 20 increase from 0.375 km).

All of these locations correspond to areas where substantial ground- or surface-water inflows enter the Red River from the north, and clear linkages between ground water and surface water are indicated. Thus, ground water at these six locations appears to be the source of sulfate loading to the Red River.

Fluoride

Fluoride had a loading ratio of about 29 over the entire stream reach (table 1), indicating that substantial loads of fluoride entered the Red River. Figure 6 demonstrates that considerable fluoride loading was evident in a single 2.4-km segment of the Red River, from about 13.2 km to about 15.6 km. Columbine Creek, Portal Springs, Cabin Springs, and Shaft Spring all entered the Red River along this reach. Fluoride concentrations in samples from Columbine Creek were about 0.3 mg/L but were an order of magnitude less than the 3 mg/L found in samples from Shaft Spring, Cabin Springs, and several manganocrete seeps on both sides of the Red River. The change in chemistry of the Red River appears to be attributable to the chemistries of these high-fluoride ground-water sources.

Aluminum

Aluminum had a loading ratio of 57 for the dissolved fraction and 108 for the total-recoverable fraction (fig. 7), indicating that there

Table 1. Mass-loading statistics for August 2001 tracer study, Red River, New Mexico.
[g/s, grams per second; Fe(T), total of iron(II) and iron(III); --, not applicable; loading ratio is output load divided by input load]

	Component	Input Load	Output Load	Instream Load Increase	Loading Ratio	Increase Attributable to the Five Major Tributaries		Ratio of Total Recoverable to Dissolved Load Increase
		----------- g/s -----------			Ratio	g/s	percent	Load Increase
Dissolved	**Alkalinity**	32	62	30	1.9	17	59	--
	Ca	12	56	43	4.5	7.9	18	--
	Mg	1.8	12	10	6.6	1.1	11	--
	Na	1.0	6.9	5.8	6.7	0.91	16	--
	Cl	0.41	3.6	3.1	8.6	0.33	11	--
	SO$_4$	5.8	127	122	22	7.9	6.5	--
	Fe(II)	[1]0.0008	0.059	0.059	[1]75	0.0048	8.3	--
	Mn	0.0008	0.47	0.47	598	0.0048	1.0	--
	F	0.026	0.74	0.72	29	0.078	11	--
	Al	0.0043	0.25	0.24	57	0.011	4.4	--
	Fe(T)	0.0033	[2]0.0047	0.0014	[2]1.4	0.0064	455	--
	Fe(III)	0.0009	0.056	0.055	63	0.0015	2.7	--
	Cu	0.0007	0.004	0.003	5.9	0.0015	42	--
	Zn	[1]0.0016	0.10	0.10	[1]61	0.0053	5.6	--
Total Recoverable	**Al**	0.020	2.1	2.1	108	0.033	1.6	8.6
	Fe(T)	0.020	2.1	2.1	108	0.033	1.6	1488
	Fe(III)	[1]0.019	2.1	2.0	[1]109	0.030	1.5	37
	Cu	0.0002	0.017	0.017	109	0.0006	3.4	4.9
	Zn	[1]0.0016	0.142	0.140	[1]90	0.0019	1.4	1.5

[1] Input concentration was less than the method detection limit for this component. Load and loading ratio were calculated by setting input concentration equal to the detection limit; thus input loads represent maximum values and loading ratios represent minimum values.

[2] Output concentration was less than the method detection limit for this component. Load and loading ratio were calculated by setting output concentration equal to the detection limit; thus output load and loading ratio represent maximum values.
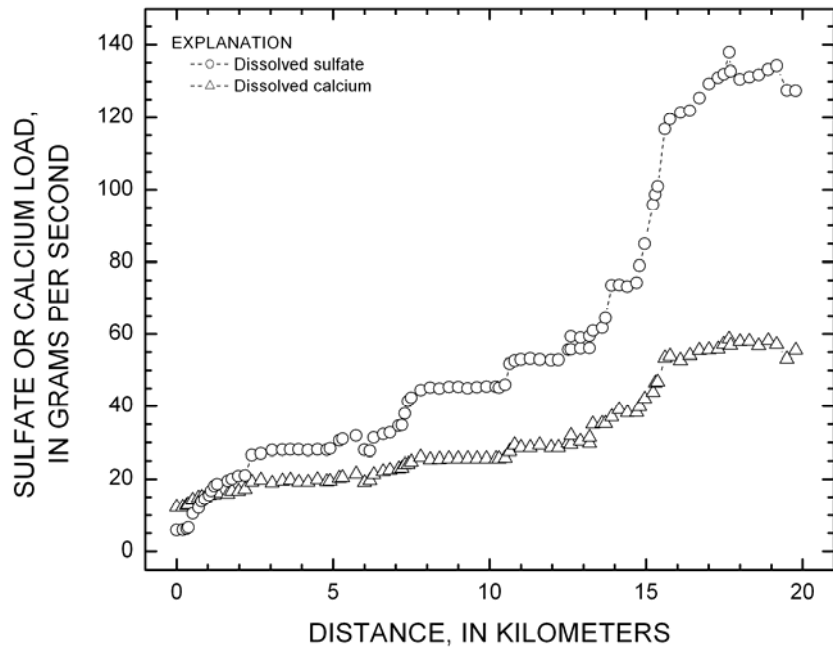
Figure 5. Dissolved sulfate and calcium loads as a function of downstream distance for the Red River, New Mexico, August 2001.
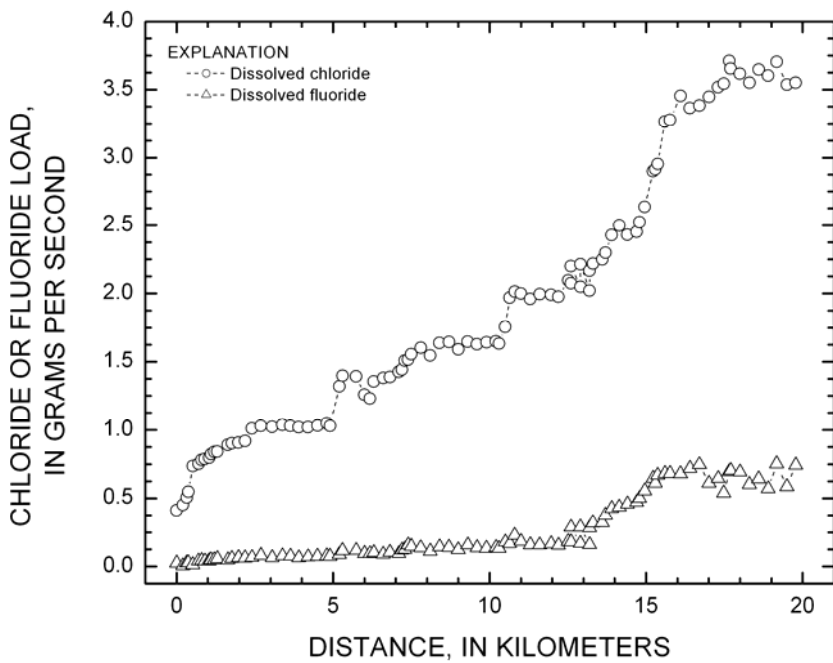
Figure 6. Dissolved chloride and fluoride loads as a function of downstream distance for the Red River, New Mexico, August 2001.

were substantial aluminum inflow loads over the study reach. Figure 7 reveals that considerable aluminum loads entered the Red River at three locations along the study reach. The first location is between 0.375 km and 0.8 km, where dissolved and total-recoverable aluminum loads increased by factors of about 10 and 6, respectively. The second location is from about 7.2 km to about 8.1 km (downstream from the Hansen debris fan, Waldo Spring, and La Bobita) where the dissolved and total-recoverable aluminum loads approximately doubled. The third location is over a 3.8-km distance from about 12.6 km to about 16.4 km (starting near Portal Springs and Columbine Creek and ending downstream from Goathill Gulch) where the dissolved and total-recoverable aluminum loads increased by factors of about 5 and 2, respectively. This relation is consistent with acidic, high-aluminum water entering the Red River and undergoing neutralization, followed by aluminum hydrolysis and precipitation, with most of the precipitate remaining in the water column. Seep and spring inflows entering from the north, with chemistry consistent with the chemical changes observed in the Red River, were observed at all three of these locations. The ordinate in figure 7 is displayed on a logarithmic scale to better display differences between the smaller loads that occur in the upstream part of the study reach.

Manganese

The loading ratio for dissolved manganese was 598. The manganese load (fig. 8) began at about 0.0007 g/s at the upper injection site, increased by a factor of 48 (from 0.0012 to 0.059 g/s) from 0.375 km to 2.4 km, and approximately doubled again between 7.2 km and 7.8 km (downstream from the Hansen debris fan; an overall factor of about 80 increase from 0.375 km). Several seeps and springs in this area contained manganese concentrations between 2.5 and 11 mg/L and were most likely the sources of manganese entering the Red River in this area.

The manganese load nearly quadrupled again from about 13.7 km to 13.9 km (near Cabin Springs; a factor of about 255 increase from 0.375 km), with essentially all the manganese remaining in solution. Cabin Springs and nearby manganocrete seeps, containing manganese at concentrations averaging 20 mg/L, likely were

representative of the ground-water sources influencing the manganese chemistry in this section of the Red River. A considerable, but more gradual, increase in manganese loads occurred for an additional 2.7 km along this reach of the Red River, from about 14.8 km until about 17.5 km, resulting in the overall loading ratio of about 598. Several seeps and springs along this section of the stream contained manganese at concentrations from 2 to 16 mg/L.

Iron

There was considerable scatter in the analytical results for the dissolved iron redox species, and most measured concentrations of dissolved iron(II) and dissolved iron(total) in the Red River were near the method detection limit. Dissolved iron(total) concentrations were determined by both the FerroZine colorimetric and ICP methods. The dissolved iron(total) and total-recoverable iron loads calculated using the more consistent ICP results (McCleskey and others, 2003; 2004) are plotted on figure 9. The ordinate in figure 9 is displayed on a logarithmic scale to better display differences between the smaller loads that occur in the upstream part of the study reach.

The dissolved iron(total) concentration at the most downstream location of the lower study reach was less than the method detection limit of 0.004 mg/L. Thus, to establish constraints on loads and loading ratios the output dissolved iron(total) concentration was set equal to the method detection limit. Dissolved iron(total) and total-recoverable iron loads increased steadily (by factors of 14 and 9, respectively) for the first 3 km of the study reach. The dissolved iron(total) and total-recoverable iron loading characteristics diverged considerably after the first 3 km. The dissolved iron(total) load doubled between 2.4 km and 3.4 km, then remained constant from 3.4 km to 6.8 km, whereupon it decreased by a factor of about 5 over the next 600 m, then remained relatively constant (between 0.005 and 0.014 g/s) from 7.4 km to 12.5 km. From 12.5 km to 13.9 km the dissolved iron(total) load decreased to near zero, followed by little variation for the remaining 6 km of the study reach (only four of 26 dissolved iron(total) concentrations were greater than the method detection limit, with the greatest of those = 0.006 mg/L).

15

Figure 7. Semi-logarithmic plot of total recoverable and dissolved aluminum loads as a function of downstream distance for the Red River, New Mexico, August 2001.

Figure 8. Total recoverable and dissolved manganese loads as a function of downstream distance for the Red River, New Mexico, August 2001.

16
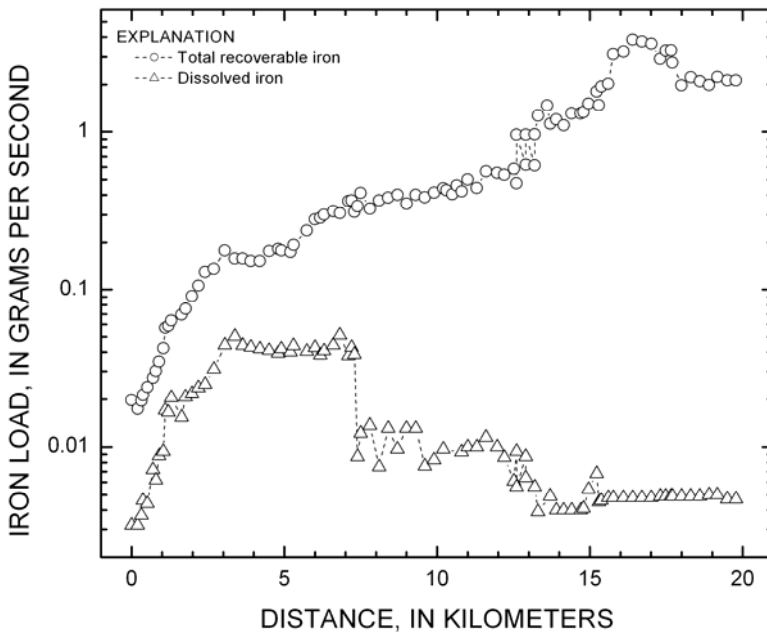
Figure 9. Semi-logarithmic plot of total recoverable and dissolved iron loads as a function of downstream distance for the Red River, New Mexico, August 2001.

From 3 km to 12.5 km the total-recoverable iron load increased by a factor of 3.5, followed by a doubling of load between 12.5 and 16 km. There was perhaps a slight decrease in total-recoverable iron load for the remaining 4 km of the study reach. The loading ratios for iron(total) determined by ICP were 1.4 for dissolved iron(total) and 108 for the total-recoverable iron(total), indicating that iron is behaving nonconservatively. These loading ratios, and the downstream profiles of dissolved and total-recoverable iron, strongly suggested that two things were happening. First, a substantial portion of the dissolved iron in the Red River hydrolyzed and precipitated but remained in the water column. Second, additional iron entered the Red River along the study reach but either entered from flowing tributaries in particulate form and remained suspended in the water column or entered from seeps in dissolved form but hydrolyzed and precipitated almost immediately, then remained suspended in the water column.

Copper

Loading ratios of 5.9 and 109 were seen for the respective dissolved and total-recoverable copper portions (table 1). With the exception of the first 1.1 km of the study reach, the increase in the copper load was almost exclusively in the suspended fraction. Copper loads increased substantially at two locations (fig. 10). The first location is from 0.4 to 1.1 km in the upstream portion of the study reach, where the respective dissolved and total-recoverable loads increased by factors of 10 and 30. The dissolved copper load remained virtually constant from 1.1 km through the remainder of the study reach. From 13.6 km (near Cabin Springs) to about 16.7 km the total-recoverable copper load increased by another factor of 3, then remained constant for the remainder of the study reach.

17
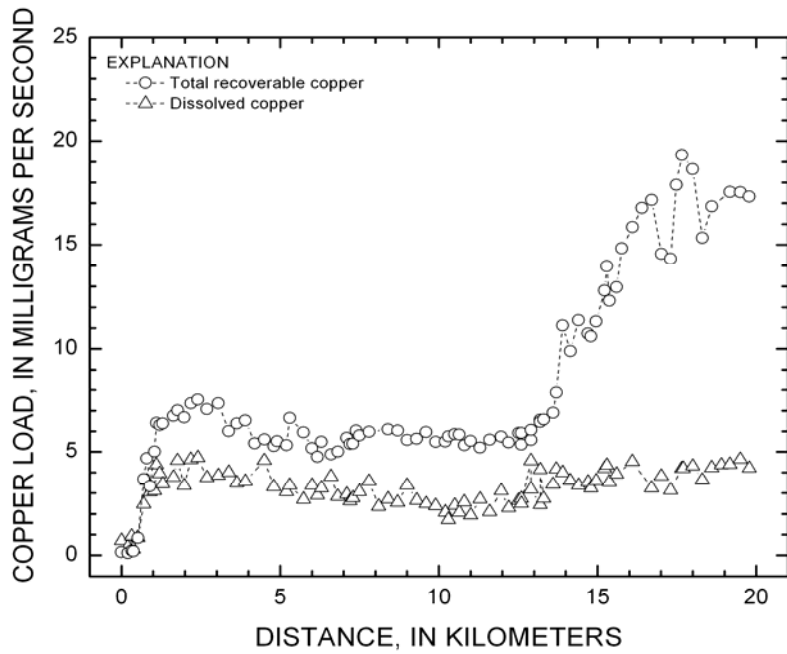
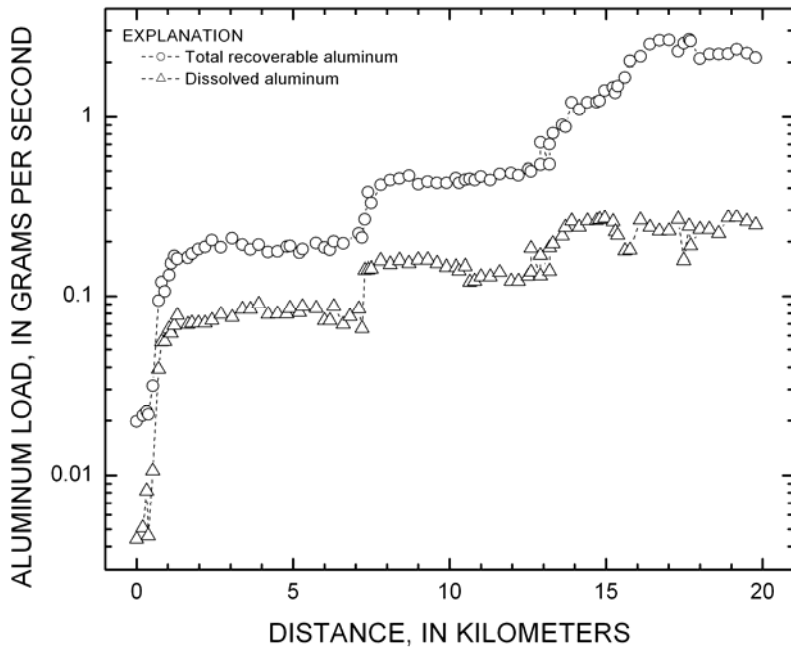**Figure 10**. Total recoverable and dissolved copper loads as a function of downstream distance for the Red River, New Mexico, August 2001.
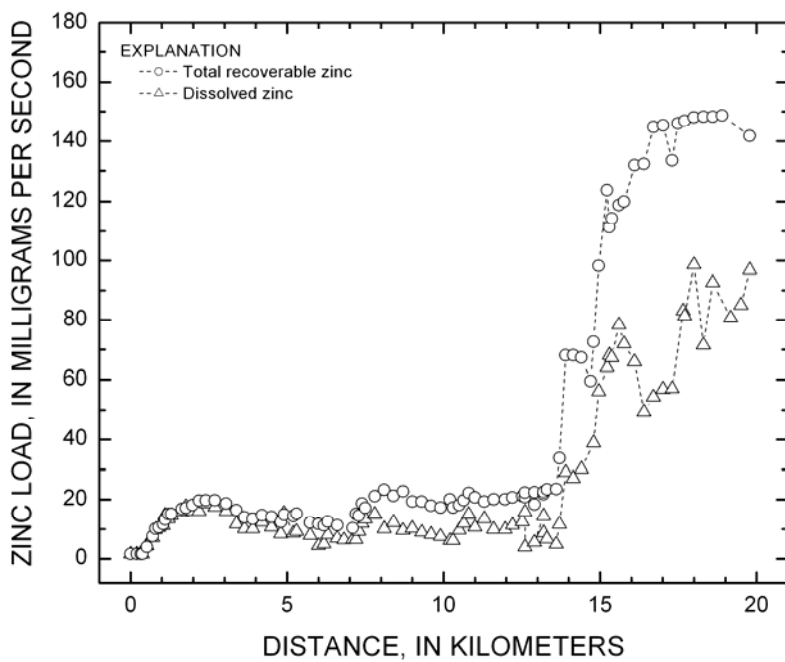
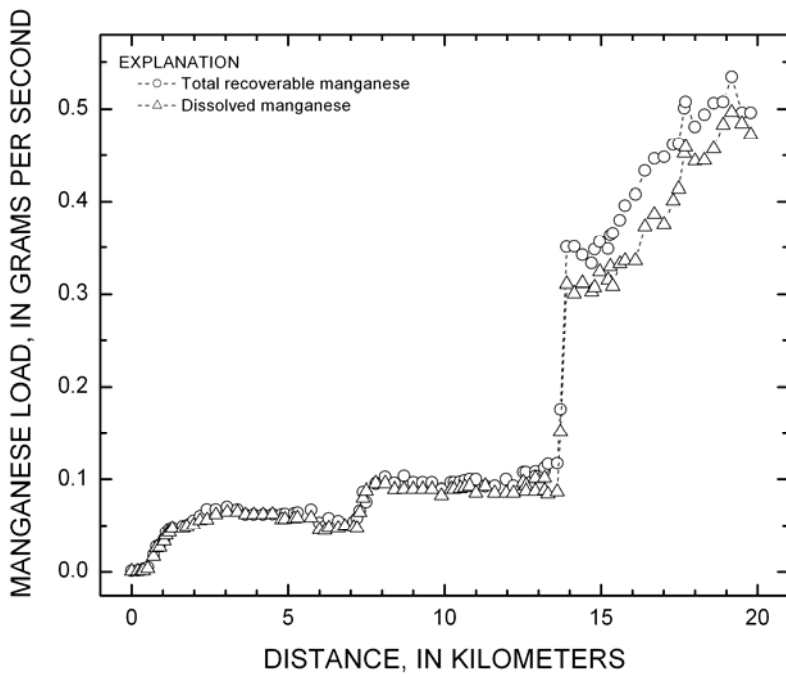**Figure 11**. Total recoverable and dissolved zinc loads as a function of downstream distance for the Red River, New Mexico, August 2001.

Zinc

Dissolved and total-recoverable zinc concentrations at the most upstream locations of the upper study reach both were less than the analytical detection limit of 0.004 mg/L. Thus, to establish constraints on loads and loading ratios the input dissolved and total-recoverable zinc concentrations were set equal to the analytical detection limit. Using these input concentrations, loading ratios of at least 61 and 90, respectively (table 1) were calculated for dissolved and total-recoverable zinc. These are minimum values because the input dissolved and total-recoverable zinc concentrations were almost certainly less than 0.004 mg/L. Gradual increases in the dissolved and total-recoverable zinc loads over the first 2.2 km of the study reach were at least a factor of 10 and were nearly equal to each other. Little change in mass loading for either fraction occurred for the next 5 km (fig. 11). From 7.2 km to 8.1 km there was an additional gradual increase of about 50 percent in zinc mass loading for the total-recoverable fraction, whereas mass loading for the dissolved fraction initially increased, then decreased to its value at the 7.2-km distance. The dissolved and total-recoverable zinc loads remained essentially invariant from 8.1 km to 13.6 km. Because the dissolved zinc concentration at 13.6 km was below the analytical detection limit of 0.004 mg/L, the 28-fold load increase for dissolved zinc between 13.6 km and 17.5 km, to about 68 times the initial load, is a minimum value. Over this same distance, the total-recoverable zinc load increased by an additional factor of 6 to about 92 times the initial load. From about 16.7 km to the end of the study reach the dissolved zinc load decreased somewhat to yield the overall loading ratio of 61 while the total-recoverable load remained essentially constant.

Identifying Sources of Mass-Loading

Inflows can come from surface-water tributaries, seeps, and ground-water inflow. Two approaches were used to identify mass-loading sources: element ratios and mixing curves.

Identifying Sources Using Element Ratios

The compositions of the inflow waters other than the five main surface tributary streams are closely related to the compositions of nearby ground waters along the Red River study reach. This conclusion is confirmed by examining mass ratios of several key dissolved components. Mass ratios of calcium to magnesium, calcium to sulfate, manganese to sulfate, manganese to zinc, and sodium to sulfate are plotted on figure 12A for the study reach near La Bobita, and on figure 12B for the study reach from Columbine Creek to Thunder Bridge. Figures 12A and 12B show these five element mass ratios for two representative inflows used as input to the reactive-transport modeling calculations and mass ratios using most probable values (MPVs, or median values) calculated from monitoring data from Naus and others (2005, La Bobita and Hottentot wells) and Molycorp (written commun., 2005, well P-2) for ground waters located nearby the sampled inflows and for a ground water upstream from the sampled inflows (Hottentot well).

La Bobita well, plotted as stars, and Hottentot well, plotted as filled circles, are compared with the inflow at 7.588 km in figure 12A. In figure 12B, monitoring well P-2, plotted as open circles, and Hottentot well, plotted as filled circles, are compared with the inflow at 19.04 km. Locations of the three wells are shown on figure 1. All five of the element mass ratios from the nearby ground waters compare more favorably with those from the sampled inflows selected for the reactive-transport modeling calculations, whereas the element mass ratios from the representative upstream ground water (Hottentot well) compare less favorably. These two plots demonstrate that nearby ground-water compositions correspond closely to the compositions of sampled inflows that provided the best reactive-transport modeling fit to observed concentrations in the two downstream sections of the Red River, whereas ground-water compositions from the upstream section correspond considerably less well. Thus, it is unlikely that ground water similar in composition to the Hottentot well is discharging to the Red River in these areas. These findings do not concur with those of Vail Engineering, Inc. (1989).
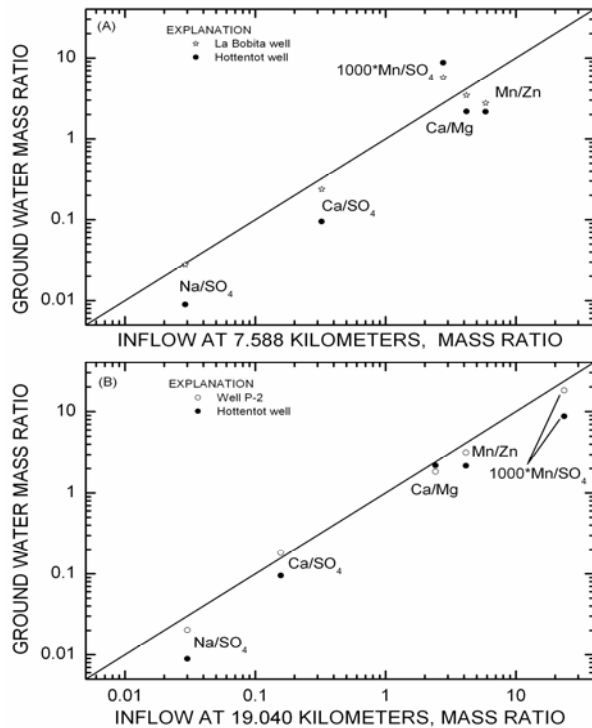
Figure 12. Comparison of mass ratios for sampled inflows with mass ratios calculated using most-probable (median) concentration values for representative ground waters for the (A) middle and (B) lower sections of the August 2001 tracer injection/synoptic study.

Identifying Sources Using Mixing Curves

Another approach to identifying water sources contributing to the Red River is to calculate ratios of selected elements to sulfate and develop mixing lines that assume conservative behavior on mixing. This approach has been used to discriminate among sources of solutes in ground waters and their mixing either with other ground waters or with surface waters (Pinder and Jones, 1969; Nordstrom and others, 1989; Davis and others, 1998; Herczeg and Edmunds, 2000). The basis for the approach comes from simple mass balance considerations (see Appelo and Postma, 1993, pp. 315-323). For mixing of two end-member waters:

$$C_1Q_1 + C_2Q_2 = C_3Q_3 \qquad (1)$$

and

$$Q_1 + Q_2 = Q_3, \qquad (2)$$

where the first end-member water, 1, has a concentration C_1 of a constituent and a water flux, or discharge, Q_1. The second end-member water and the mixture are shown by concentrations and discharges subscripted 2 and 3, respectively. By dividing through equation 2 by Q_3 the second equation becomes an identity that represents the fractions of water mixed, and setting $Q_1/Q_3 = x$ yields $Q_2/Q_3 = 1-x$. Dividing both sides of equation 1 by Q_3 and substituting these relations into the result gives:

$$C_1x + C_2(1-x) = C_3. \qquad (3)$$

Hence, if the two end-member compositions are known the mixing line is simply the calculation of C_3 for the range of x from 0 to 1.

For the following calculations, MPVs based on the monitoring results of Naus and others (2005) for the Straight Creek wells and Nordstrom and others (2005) for the Hottentot, La Bobita, and Hansen wells were used for all ground waters and August 2001 analytical results were used for all surface waters. Well SC-7A, the farthest-downstream Straight Creek well (fig. 2), was chosen as the higher-concentration end-member, and Red River water at 7.20 km, upstream from the identified mixing zone, was chosen as the dilute end-member. Calcium-to-sulfate mole ratios and magnesium-to-sulfate mass ratios are plotted as a function of sulfate concentration on figures 13A and 13B, respectively. These two figures illustrate that Red River water at 7.80 km, the four inflowing tributaries at 7.27 km, 7.30 km, 7.457 km, and 7.588 km used as input to the OTEQ reactive transport model, the Hansen well, the La Bobita well, well SC-8A, and well MMW-17A fall close to the mixing line between water from SC-7A and the Red River at 7.20 km, suggesting that all these waters have chemical signatures consistent with the changes in chemistry of Red River water over this reach and thus are also related to each other. The similarity between water from well MMW-17A and La Bobita is an indication that the natural acidic drainage signature gets this far downstream but not much farther as indicated by the differing chemical signature for water from well MMW-43A. The calcium- and magnesium-to-sulfate ratios for the Hottentot well and well
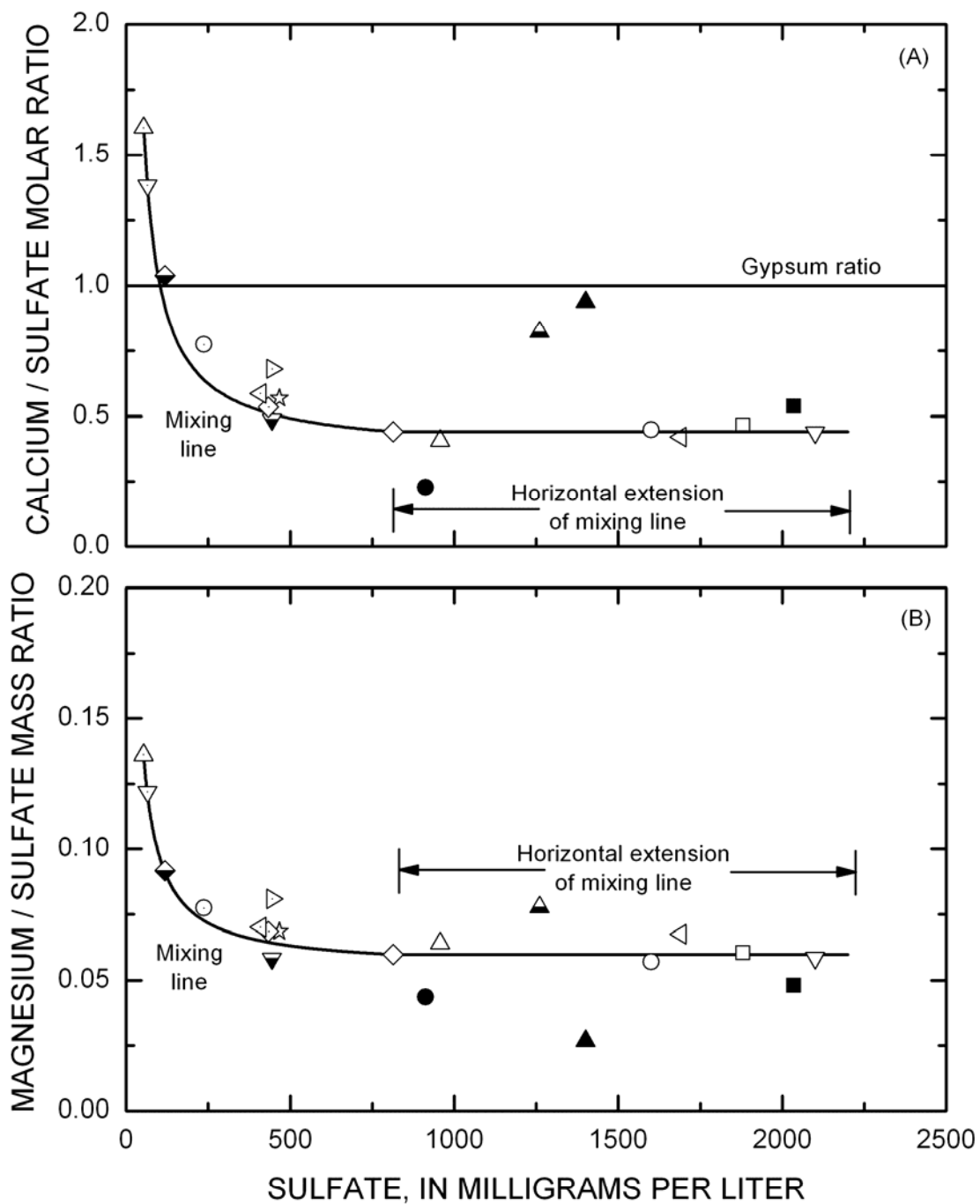
Figure 13. Mixing curves for water from Straight Creek Well 7A and Red River water at 7,200 meters for (A) calcium-to-sulfate molar ratios and (B) magnesium-to-sulfate mass ratios for the Red River, selected tributary inflows, and nearby wells, August 2001.

SC-5B do not plot as close to the mixing line, strongly suggesting that these wells are not contributing substantially to the composition of the water entering this reach of the Red River.

The calcium-to-sulfate and magnesium-to-sulfate ratios for water from wells SC-5A, SC-3A, SC-4A, SC-6A, and SC-1A all plot close to a horizontal line extending the mixing line from the SC-7A sulfate concentration of 815 mg/L to the SC-1A sulfate concentration of 2,100 mg/L. The close proximity of these ratios to the horizontal line is strong evidence that the primary mechanism responsible for changes in the calcium and magnesium concentrations is dilution with relatively clean water rather than mixing with more contaminated water from another source.

The ratios of manganese and zinc to sulfate as a function of sulfate concentration for many of the ground waters considered here (figs. 14A and 14B) plot remarkably close to the mixing lines for SC-7A water and Red River water at 7.20 km, especially considering the over 100-fold-lower concentrations of these two constituents compared with those for calcium and magnesium. The more concentrated waters from the Straight Creek wells plot above the mixing line and correspondence for manganese and zinc is somewhat reduced compared with that for calcium and magnesium, indicating that shallow inflow waters likely have signatures of depleted manganese and zinc. Manganese is redox-active and has low solubility in its oxidized forms. Zinc is likely to become adsorbed to hydrous iron and manganese oxides that form with increasing pH caused by dilution. Thus, these two reactive components are likely being removed from solution along the ground-water flow path by oxidation and precipitation for manganese and sorption for zinc. It is notable that, in contrast to ground water from other nearby sources, water from La Bobita well does not have a depleted manganese and zinc signature.

Summary of Ground-water and Surface-water Sources of Mass Loading

The chemical compositions of the five main surface tributary streams to the Red River--Bitter, Mallette, Pioneer, Columbine, and Bear Creeks--accounted for a smaller fraction, relative to their flow, of the mass loading observed. Inflow discharges of the five main surface tributary streams were estimated by differencing main stem flows, calculated from the tracer-injection experiment, above and below the respective tributaries and assuming that all the flow increases were attributable to the respective streams. Using this assumption, the five main tributary streams accounted for 32 percent of the flow increase over the entire study reach. However, with the exceptions of carbonate alkalinity and dissolved iron(total), their inflow loads accounted for only 1 percent (Mn) to 18 percent (Ca) of the cumulative instream loads (table 1). Thus, while the remaining inflow sources accounted for 68 percent of the inflow discharge, they accounted for 82 to 99 percent of the cumulative instream mass loads.

Increases in mass loading of constituents occur at a small number of key locations along the study reach characterized by the presence of ground-water sources with chemical compositions that can be used to explain changes in mass loading observed in the Red River. Two stream sections, from 13.7 to 13.9 km (near Cabin Springs) and from 14.7 to 17.5 km, encompassing the areas near Thunder Bridge, Goathill Gulch, and Capulin Canyon, contribute by far the largest mass loading of the components of interest for this study, and the chemical signature of the mass loading source closely approximates the chemical signatures found in ground waters adjacent to the Red River. Example representative ground waters include those from wells P-1, P-2, P-3, P4B, P5A, P5B, and Columbine #2, among others. These seven wells are not shown but all are within 300 meters downstream from the Cabin Springs area shown on figure 3. Other segments of the Red River that experience substantial increases in mass loading include the initial 2.4 km of the study reach (Bitter Creek) and the segments from 6.2 to 7.8 km (Hansen and La Bobita areas), 10.5 km (near Sulphur Gulch), and from 12.2 to 12.6 km (near Portal Springs).
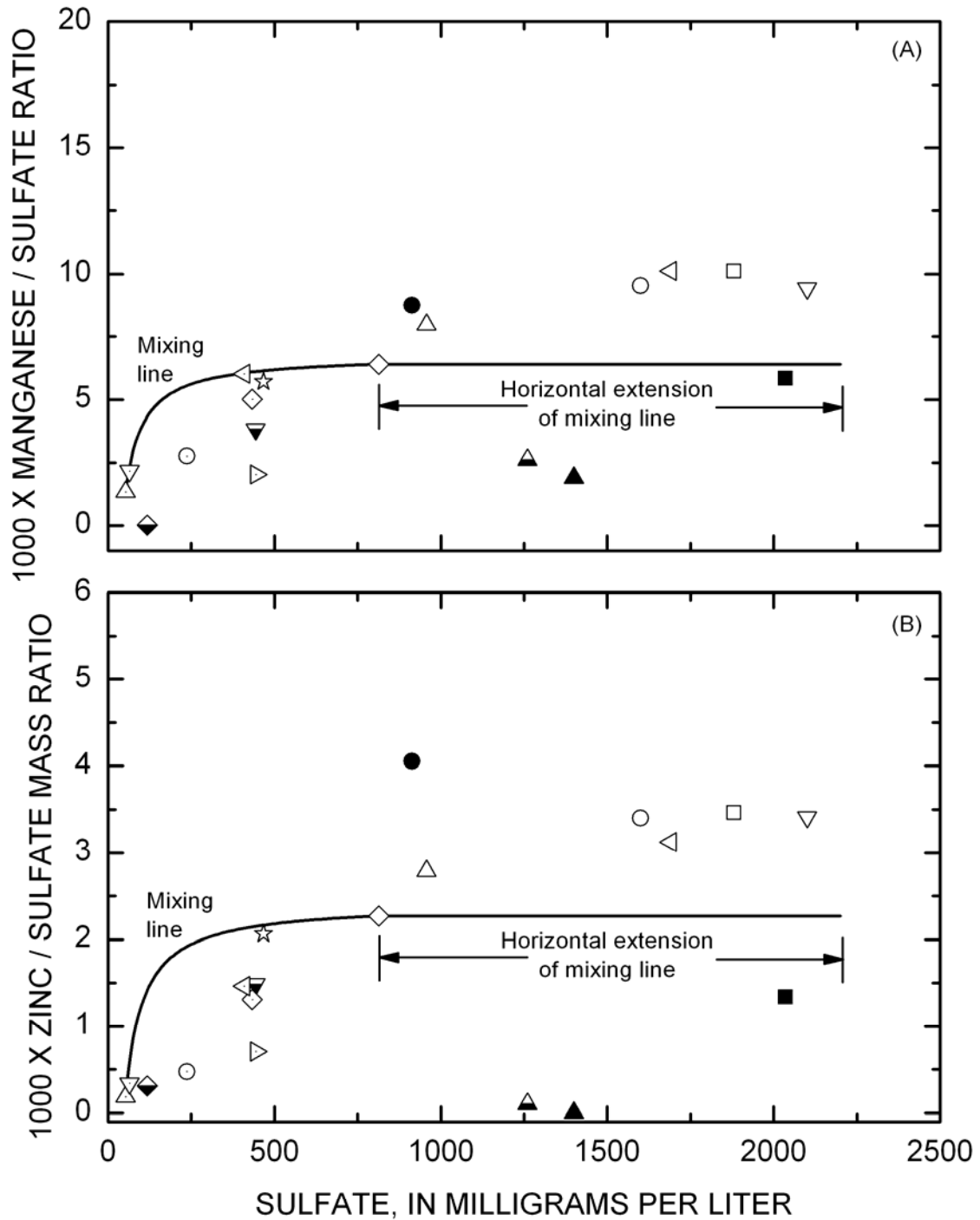
Figure 14. Mixing curves for water from Straight Creek Well 7A and Red River water at 7,200 meters for (A) the manganese-to-sulfate mass ratios and (B) the zinc-to-sulfate mass ratios for the Red River, New Mexico, August 2001.

ALUMINUM SPECIATION MODELING

Previous studies in similar mountain terrains have shown that for streams receiving acid mine drainage, pH variations and iron and aluminum precipitation are the dominant reactive processes during downstream transport and are the main challenges for simulation of reactive transport processes (Broshears and others, 1996; Runkel and Kimball, 2002; Ball and others, 2004). Furthermore, these three processes are closely interrelated so that a change in the simulation for one process affects another. The simulation of mineral precipitation also is affected strongly by the equilibrium solubility-product constant chosen for the mineral and to a lesser extent by the enthalpy of the reaction. For precipitation of aluminum minerals in acid-sulfate waters there are several possible mineral phases (Nordstrom, 1982).

In previous studies, it has been shown that acid surface waters that increase in pH with downstream distance as a result of dilution and buffering begin to precipitate aluminum at a pH of 4.5 to 5.0 (Nordstrom and Ball, 1986). The resulting loss of aluminum has been simulated successfully using the solubility range for microcrystalline to amorphous $Al(OH)_3$ (log K_{sp} from 9.35 to 10.8, respectively; Nordstrom and others, 1990), even though the precipitating phase contains sulfate and is approximated by the composition of basaluminite (Bigham and Nordstrom, 2000). For the purposes of this study, it seemed prudent to examine more closely the speciation of aluminum and the hypothesis of a solubility control at pH $\geq$ 4.5.

Aluminum solubility in the Red River appears to be greater than that indicated by the geochemical speciation modeling results. The apparently increased solubility is seen in the decrease in saturation indices for amorphous $Al(OH)_3$ at pH values greater than 7 and in the slight non-linearity in the relation of the free aluminum-ion activity to pH. The apparently increased solubility also is seen in the nearly constant aluminum concentrations in the Red River between pH values of 7 and 9 and in the deviation from 4 of the slope of this relation at pH values greater than 7. A slope of 4 would have

indicated control of aluminum solubility in this pH range by the $Al(OH)_4^-$ complex.

Speciation and Saturation Indices

Ion speciation and mineral saturation indices were computed with the WATEQ4F code (Ball and Nordstrom, 1991) using the ion association model. The saturation index (SI) is defined as the logarithm of the ratio of the ion-activity product, IAP, to the solubility-product constant, K_{sp} (Nordstrom and Munoz, 1994):

$$SI = \log\left[\frac{IAP}{K_{sp}}\right] \qquad (4)$$

If the solution is in equilibrium with a mineral of known composition and known equilibrium solubility, IAP = K_{sp} and SI = 0. If SI > 0, the solution is supersaturated and the mineral would tend to precipitate; if SI < 0, the solution is undersaturated and the mineral, if present, would tend to dissolve. For example, the SI for $Al(OH)_{3(s)}$ would be

$$SI[Al(OH)_{3(s)}] = \log\frac{[Al^{3+}][H_2O]^3[H^+]^{-3}}{K_{sp(Al(OH)_{3(s)})}} \qquad (5)$$

where concentrations have been converted to ionic activities, [], water activities near one can be neglected, and log K_{sp}=10.8 at 25°C (Nordstrom and others, 1990) for the reaction

$$Al(OH)_{3(am)} + 3H^+ = Al^{3+} + 3H_2O. \qquad (6)$$
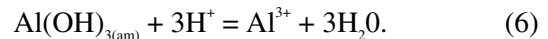
Temperature and ionic strength corrections are made for all equilibrium reactions.

Trends in Aluminum Speciation and Saturation Indices

The SI values for amorphous $Al(OH)_3$ for all Red River inflow and stream samples are shown in figure 15 as a function of pH for both synoptic surveys. This plot illustrates that samples from the Red River with pH from 7.4 to nearly 9.0 are within -2 to +0.5 SI units of equilibrium saturation for amorphous $Al(OH)_3$. The samples
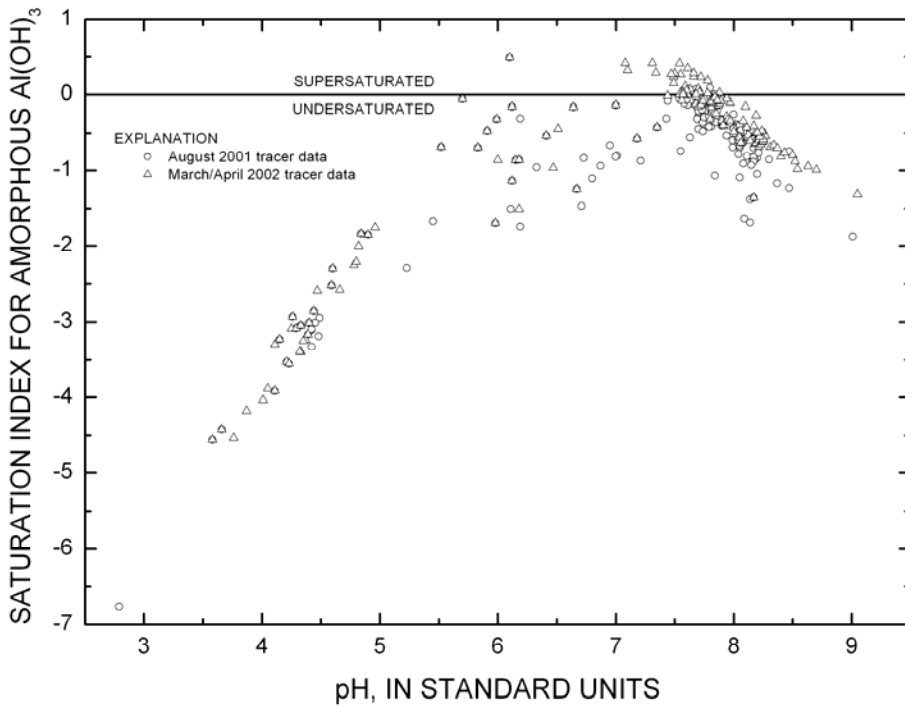
Figure 15. Saturation index of amorphous Al(OH)$_3$ as a function of pH for all Red River inflow and stream samples.
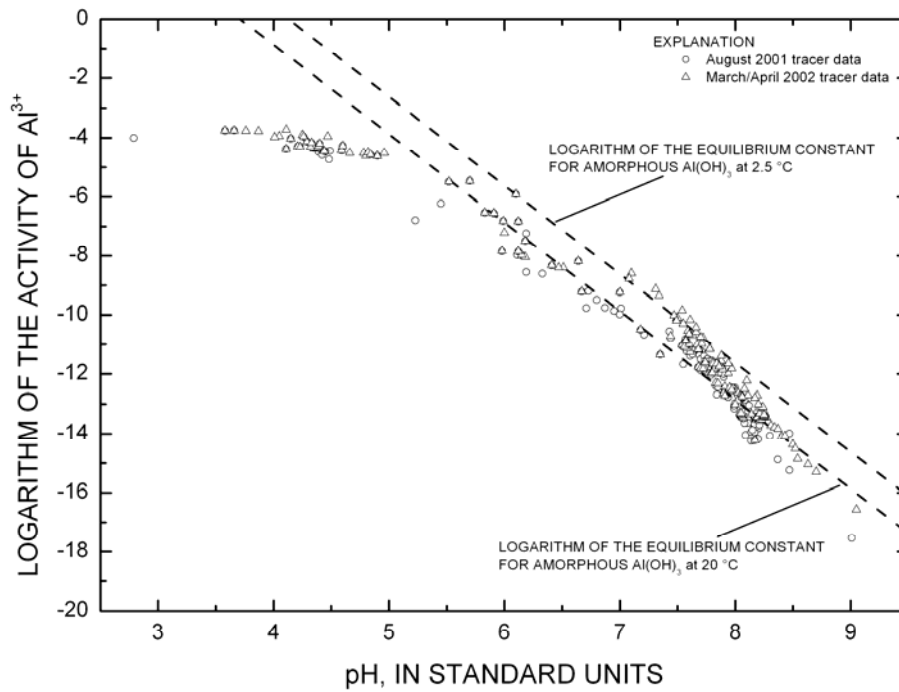
Figure 16. Logarithm of the activity of aqueous Al^{3+} as a function of pH for all Red River inflow and stream samples

with intermediate pH values reflect an approach to solubility equilibrium from pH values greater than about 5.5 up to pH values near 7, whereupon the SI values decrease markedly and consistently from pH values near 7 to the highest pH values near 9. This decreasing trend with increasing pH has not been clearly observed before and merits further attention.

As explained in Nordstrom and Munoz (1994, p. 259 to 264), dissolved aluminum hydrolyzes over the pH range 4 to 8 according to the sequence of hydrolysis constants: $pK_1 = 5$, $pK_1K_2 = p\beta_2 = 10$, $p\beta_3 = 17$, $p\beta_4 = 23$ (based on Nordstrom and May, 1996). The Red River data for pH 7 to 9 are in the range where the dominant hydrolysis product is $Al(OH)_4^-$. Consequently, the relation between the free aluminum-ion activity and pH is based on the β_4 stability constant:

$$\beta_4 = \frac{\left[Al(OH)_4^-\right]\left[H^+\right]^4}{\left[Al^{3+}\right]\left[H_2O\right]^4} = 10^{-23} \qquad (7)$$

or in logarithmic form and assuming $[H_2O] = 1$:

$$-\log \beta_4 = p\beta_4 = \log\left[Al^{3+}\right] - \log\left[Al(OH)_4^-\right] + 4pH = 23 \qquad (8)$$

and (rearranging equation 8):

$$\log\left[Al^{3+}\right] = \log\left[Al(OH)_4^-\right] - 4pH + 23 . \qquad (9)$$

This relation holds at constant temperature and pressure if there are no other constraints on the system. If gibbsite solubility is a constraint, then substitution of the equilibrium solubility-product constant leads to a relation between $\log[Al^{3+}]$ and pH with a slope of 3 (Nordstrom and Munoz, 1994, p. 262). The empirical slopes in figure 18 closely approximate the slope and intercept of equation 9 which means that the data in figure 18 have no solubility control and are reflecting the hydrolysis speciation imposed by the aqueous model. In other words, the speciation computation has applied a pH dependence that may not exist in the data. To test this hypothesis, the dissolved aluminum concentration was plotted as a function of pH for pH values greater than 7 to see if any pH dependence is apparent in the analytical data before speciation. This approach was used for iron by Kimball and others (1995). The result

(fig. 19) shows a nearly constant aluminum concentration for both 2001 and 2002 data sets for the range of pH = 7 to 9. The reverse approach also was used to test this conclusion, that is, a constant aluminum concentration of 0.16 mg/L was applied to the same data set (of pH = 7 to 9) and then speciated as before. The results were linearly regressed and had a slope of -4.3 and an intercept of 22. Hence, under these conditions no apparent solubility control on the aluminum concentrations occurs, nor is there a dominant hydrolysis product of aluminum. One reasonable explanation is that organically bound aluminum may play a substantial role in the chemical behavior of aluminum in these waters. Because dissolved organic carbon (DOC) is typically about 1 to 2 mg/L and the aluminum concentrations at pH>7 are less than 0.3 mg/L, it appears reasonable that DOC is binding to much of the dissolved aluminum. Studies in the Adirondack Mountains related to the effects of aluminum solubilization by acid rain and acidified surface waters have reached similar conclusions by directly analyzing for organically bound aluminum (Driscoll and others, 1984; Driscoll and Postek, 1996; Hendershot and others, 1996).

The complexity of the Red River water chemistry arises from the multiplicity of both acidic and basic waters that enter it from tributaries, seeps, and ground waters. The Red River itself is circumneutral in pH (7 to 8) most of the time. Acidic inflow waters carry high aluminum concentrations so that when these waters enter the Red River they will immediately precipitate a hydrated aluminum phase. The effect of this mixing and precipitation can be better appreciated in figures 20A and 20B that show variations in pH, SI for amorphous $Al(OH)_3$, and dissolved aluminum concentrations with downstream distance. Figure 20A demonstrates a broad pH decrease where acidic Bitter Creek debris flow ground waters mix with the Red River (0 to 1.5 km) and then a rebound followed by two obvious low-pH troughs, at Waldo Spring – La Bobita (7.0 to 7.5 km) and Thunder Bridge (15.0 to 15.5 km). Smaller troughs can be seen near the mill yard (about 10.0 km), near Cabin Springs (about 13.3 km), and near Spring 13 (about 17.6 km). The saturation indices for amorphous $Al(OH)_3$ tend to give a mirror image of these pH
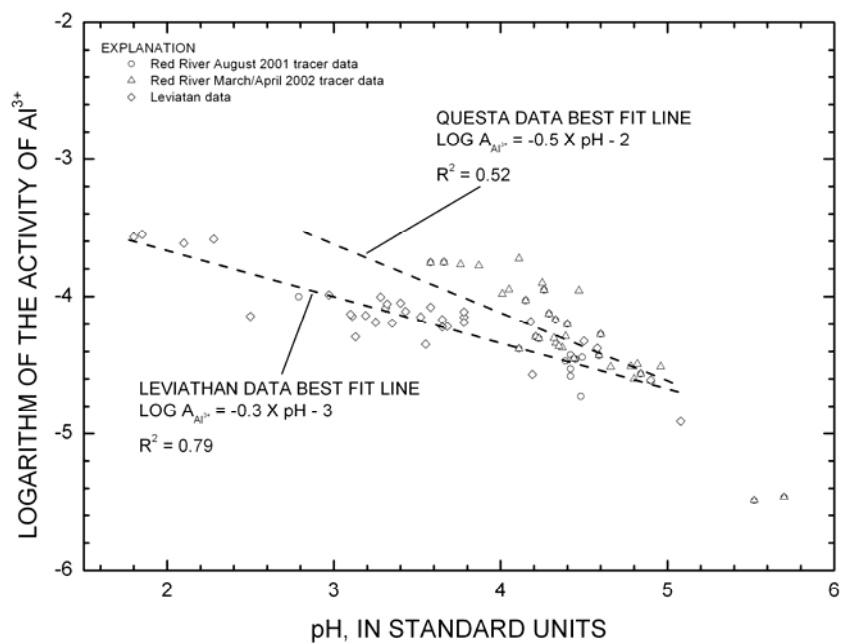
Figure 17. Logarithm of the activity of Al^{3+} as a function of pH between pH 1.5 and pH 6 for Red River and Leviathan data.
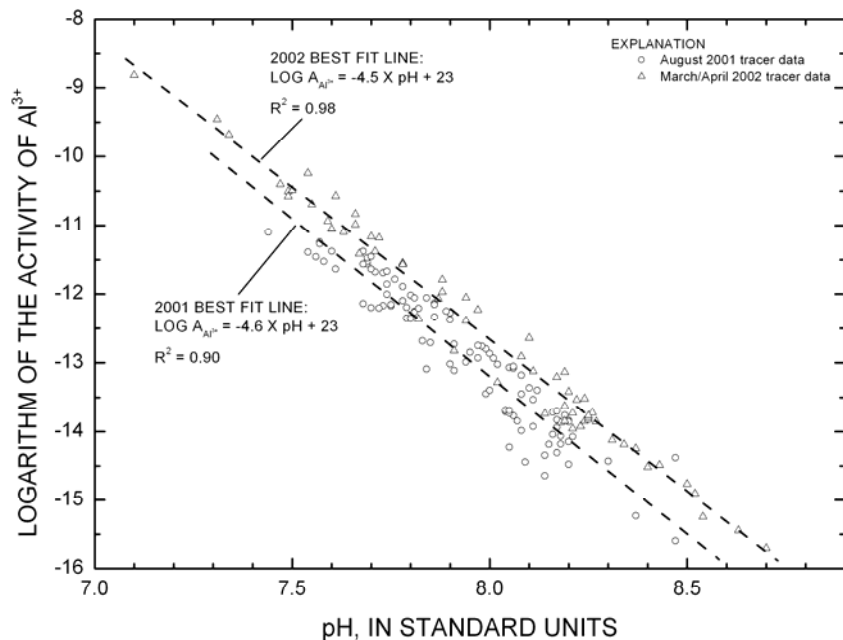
Figure 18. Logarithm of the activity of aqueous Al^{3+} for the main stem of the Red River as a function of pH between pH 7.1 and pH 8.7.
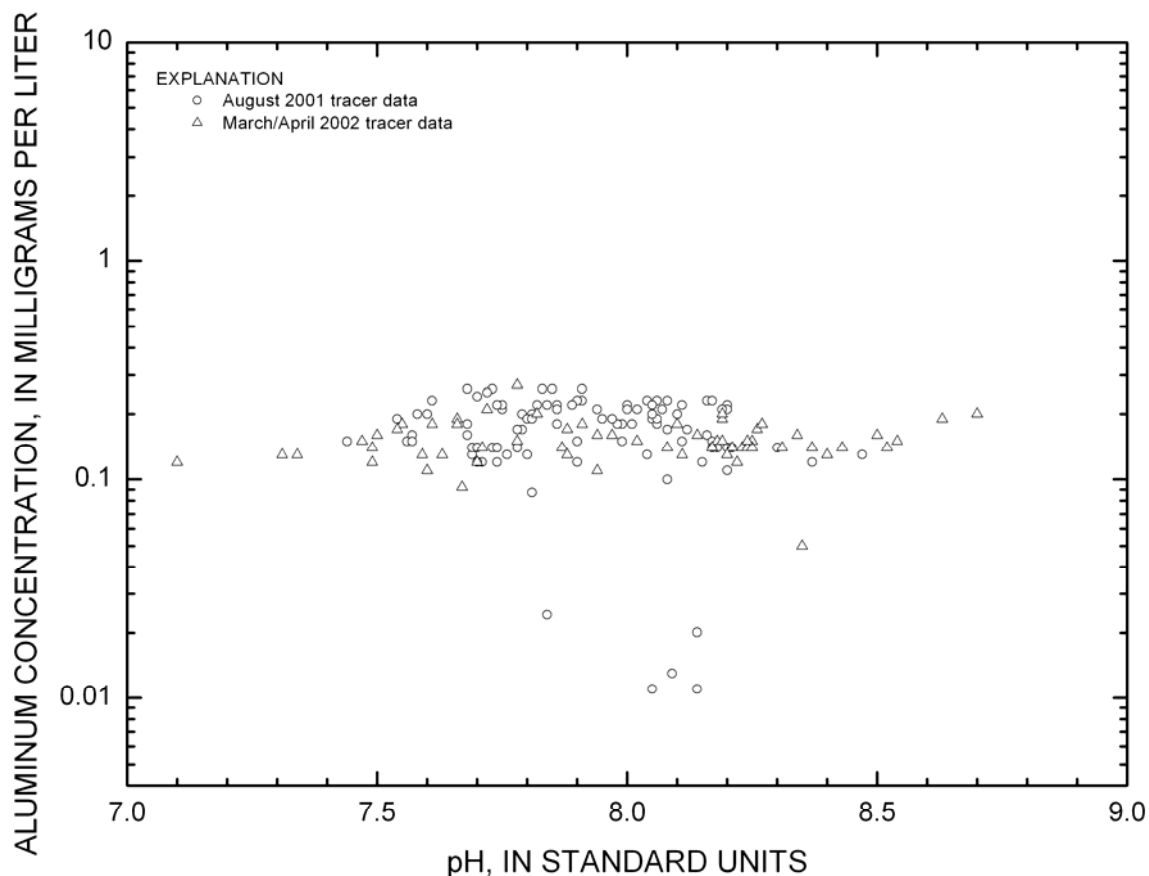
Figure 19. Dissolved aluminum concentration plotted on a logarithmic scale for the main stem of the Red River as a function of pH between pH 7.1 and pH 8.7.

variations, increasing whenever the pH decreases. Figure 20B plots the trend in aluminum concentration with downstream distance. As expected, the aluminum concentration increases where the pH decreases, and this relation would exert a control on the SI values. However, whereas the relation of dissolved aluminum to pH (fig. 20B) is real, the relation of the amorphous $Al(OH)_3$ SI to pH (fig. 20A) has an artificial component. Thus, a primary cause of SI variations (and the reason they mimic pH more closely than do the dissolved aluminum concentrations) is the artificial effect of hydrolysis imposed by the aqueous model on aluminum speciation, and is the result of using hydrogen to the third power compared to aluminum to the first power in the SI calculations.

Fluoride plays a role in the speciation of aluminum in the slightly acidic pH range and may affect the SI values for amorphous $Al(OH)_3$ in the 5<pH<7 range. Average distributions of species were calculated by grouping the WATEQ4F speciation results into three sets based on their measured pH values, acidic (pH<5), mildly acidic to neutral (5<pH<7), and neutral to basic (pH>7). For each water analysis, activities of the Al^{3+}, $AlOH^{2+}$, $Al(OH)_2^+$, $Al(OH)_4^-$, AlF^{2+}, AlF_2^+, and $AlSO_4^+$ species were summed, the percent of the sum of activities was calculated for each species, and average percent values for each species were calculated for each of the three sets. These average percent values are plotted in pie diagrams in figures 21 (pH<5), 22 (5<pH<7), and 23 (pH>7). The speciation results shown in these three figures demonstrate that the distribution of

28
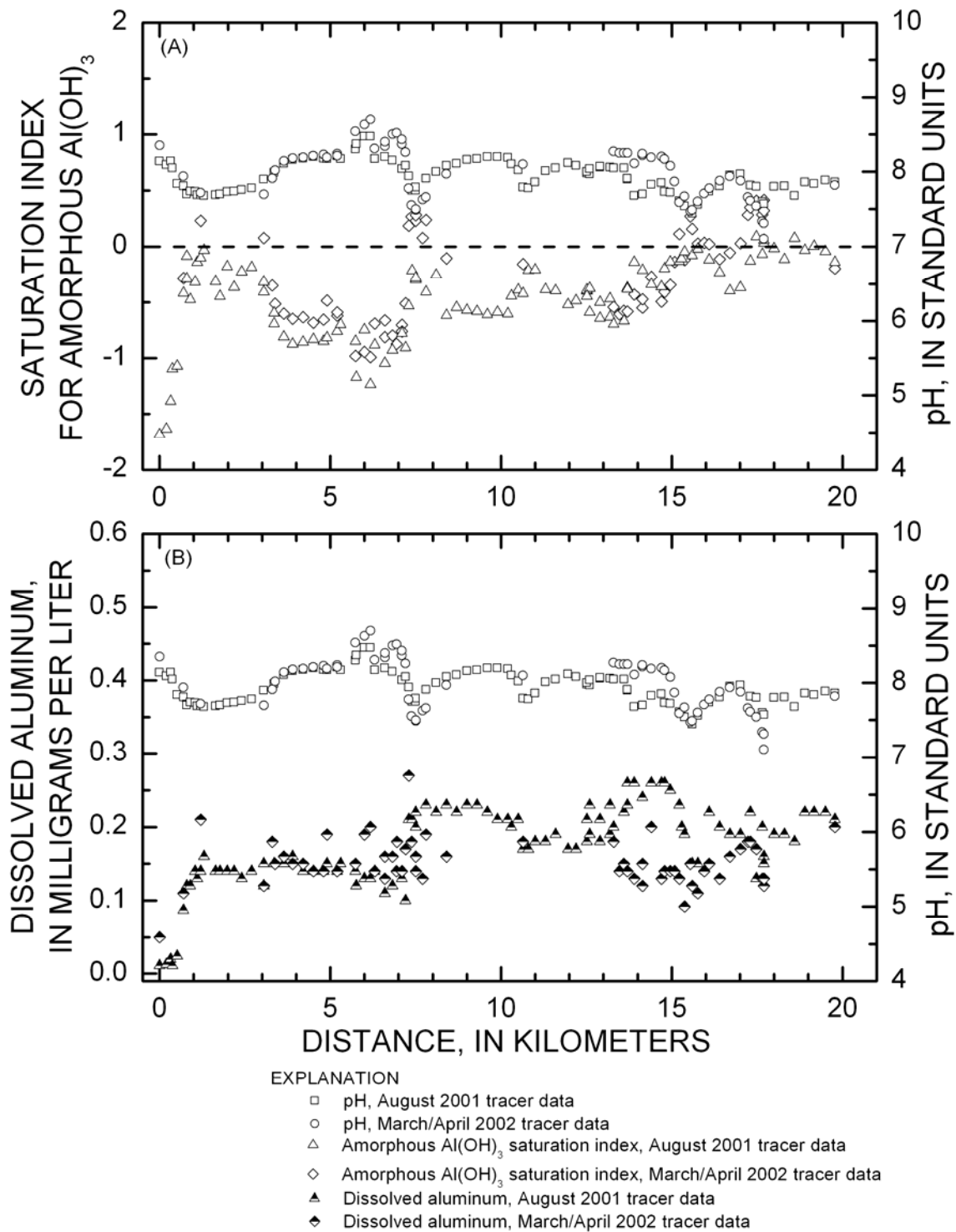
Figure 20. Graphs as a function of downstream distance of (A) amorphous Al(OH)$_3$ saturation index and pH, and (B) dissolved aluminum and pH, in Red River stream water.
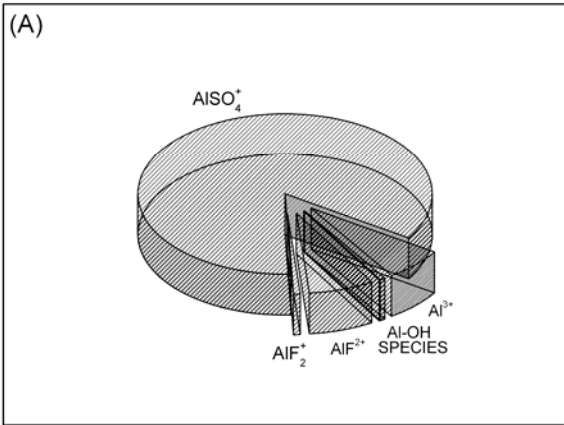
Figure 21. Average aluminum speciation for the seven most predominant aqueous species in 0.45-micrometer-filtered Red River stream water at pH < 5 for the 2001 and 2002 tracers.
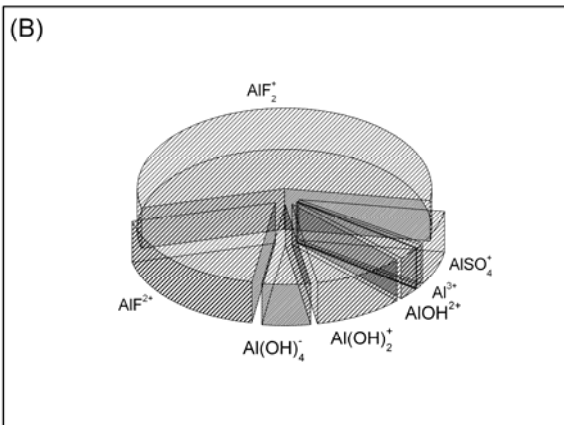
Figure 22. Average aluminum speciation for the seven most predominant aqueous species in 0.45-micrometer-filtered Red River stream water at 5 < pH < 7 for the 2001 and 2002 tracers.
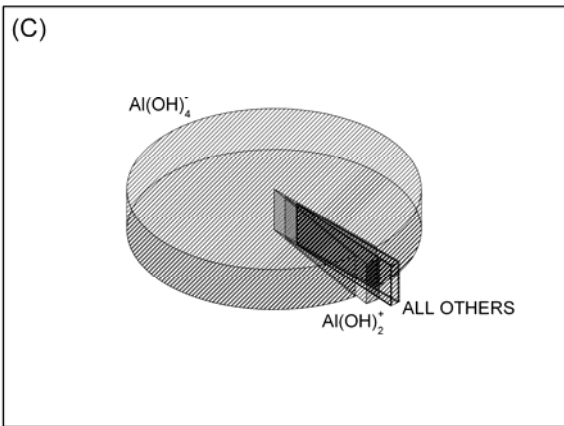
Figure 23. Average aluminum speciation for the seven most predominant aqueous species in 0.45-micrometer-filtered Red River stream water at pH > 7 for the 2001 and 2002 tracers.
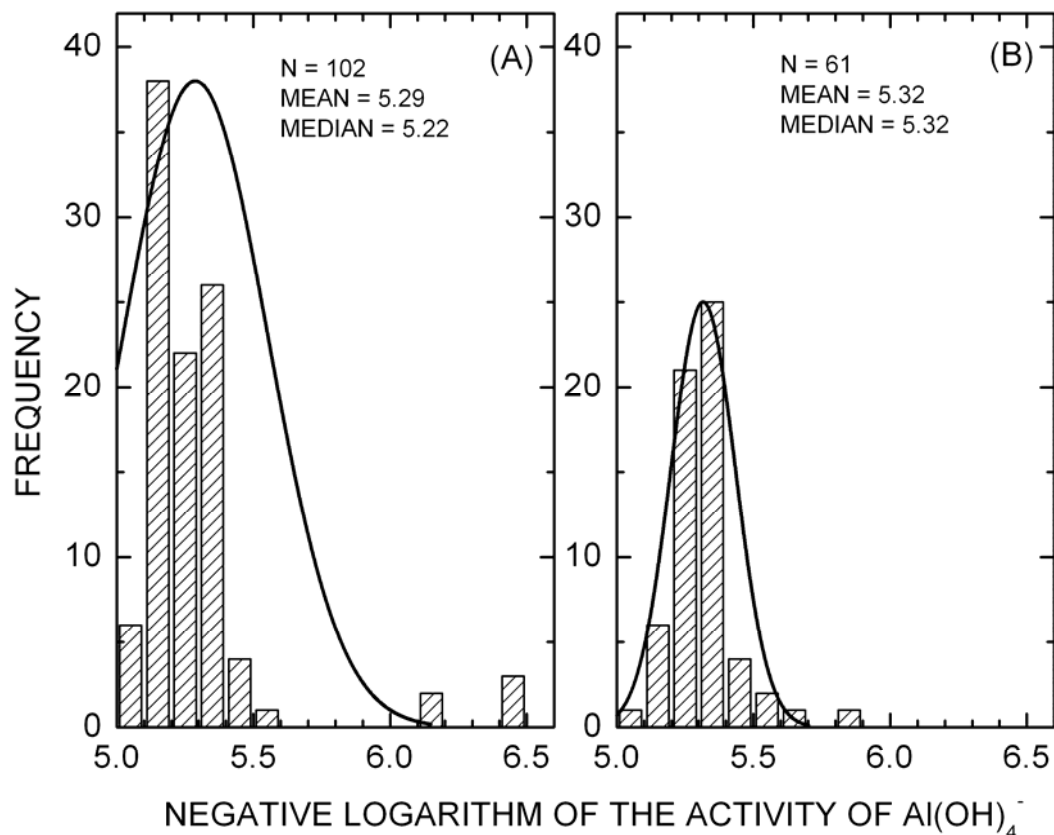
Figure 24. Histograms of the negative logarithm of aqueous Al(OH)$_4^-$ values in Red River waters including normal fit lines for 2001 data (*A*) and 2002 data (*B*).

aqueous species varies dramatically among the pH ranges. The predominant aqueous complexes are AlSO$_4^+$ at pH<5, AlF$_2^+$ at 5<pH<7, and Al(OH)$_4^-$ at pH>7, and the activity of the Al^{3+} ion is continually reduced with each increasing pH range.

Both the AlF$_2^+$ and AlSO$_4^+$ complexes predominate less in their pH ranges than does the Al(OH)$_4^-$ complex in its pH range. Reduced Al^{3+} complexing and greater aluminum concentrations at lower pH result in greater Al^{3+} ion activities, and despite the concurrent reduction of OH$^-$ ion activities in the 5<pH<7 range compared with the pH>7 range, larger Al(OH)$_3$ saturation indices result. A frequency plot of the negative logarithms of the aqueous Al(OH)$_4^-$ (*p*Al(OH)$_4$) activities (fig. 24) shows the Red River main stem samples clustered closely around an average of about 5.3. These values should vary in some linear fashion as a function of pH but they do not,

thus some other aqueous species likely is complexing aluminum in this pH range. The hypothesis of aluminum-organic complexing appears to fit the observed data and explain the higher than expected solubility of aluminum in the Red River.

REACTIVE-TRANSPORT MODELING

Reactive-transport modeling can provide quantitative estimates of the geochemical processes causing downstream attenuation of trace metals in acid mine waters under varying flow conditions. Such modeling can be used to examine the effectiveness of potential remediation scenarios, providing a scientific basis for environmental and regulatory decisions (Runkel and Kimball, 2002; Ball and others,

31

2004). In the Red River Basin, two synoptic studies with tracer injection helped quantify solute sources and sinks, and allowed calibration of models for August 2001 and March/April 2002 flow regimes.

One objective of stream characterization is to describe the watershed in as much detail as possible, to understand both the stream hydraulics and the reactive chemistry. One of the most important aspects of the modeling effort is to provide a test of inflows: can the reactive transport model account simultaneously for instream changes caused by both lateral inflows and reactive processes? Reactive solute-transport modeling for this analysis uses the OTEQ computer code. The model accounts for a variety of physical and chemical processes including advection, dispersion, lateral inflow, transient storage, transport and deposition of water-borne solid phases, acid-base reactions, complexation, precipitation/ dissolution, and sorption/ desorption. Consideration of these processes provides a general modeling framework for the simulation of trace-metal fate and transport. The OTEQ computer code and the models used in it have a considerable history of research and development (Bencala and Walters, 1983; Runkel and Kimball, 2002; Runkel and others, 1996a; 1999; 2003; Ball and others, 1999; 2004)

Applications of OTEQ to date have included the analysis of geochemistry and transport including pH-modification experiments (Runkel and others, 1996b; 1999). These experiments represent dynamic conditions that mimic events such as episodic acidification, unplanned mine discharges (blowouts), and accidental spills (for example, Achterberg and others, 1999). Analyses of these experiments have provided quantitative descriptions of trace-metal behavior as a neutral-pH pulse propagates its way through the hydrologic system (Broshears and others, 1996). The OTEQ program also was applied to the simulation of remediation scenarios for the Summitville Mine, Colorado (Ball and others, 2004). Another application of interest is quantification of the processes that determine the steady-state profile of trace metals and pH (Runkel and Kimball, 2002). This application is especially important when considering the potential effects of remediation on stream-water quality.

In this report, model application to steady-state data helps describe the sources of metals and acidity, and accounts for inflows to the stream and processes that control metal concentrations. Given this quantitative description of existing conditions, additional simulations could be conducted to estimate possible stream-water quality under different flow regimes and remediation plans. Such simulations were not done for this study. Steady-state application of reactive transport modeling using the OTEQ computer code to the Questa Mine area August 2001 and March/April 2002 synoptic studies is described in the following sections.

Conceptual Model and Governing Transport Equations

The hydrologic transport submodel in OTEQ is based on the OTIS solute-transport code, a one-dimensional advection-dispersion equation with additional terms to account for lateral inflow and transient storage (Bencala and Walters, 1983; Runkel, 1998). Transient storage has been noted in many streams in which solutes are temporarily detained in small eddies and stagnant zones of water that move more slowly relative to the faster-moving water near the center of the channel. In addition, parts of the flow move solutes through the coarse gravel of the streambed and porous areas within the stream bank. Lateral inflow represents additional water entering the main channel as overland flow, interflow, and ground-water discharge. Conservation of mass results in a set of partial differential equations (PDEs) describing the physical transport of multiple solutes.

The chemical equilibrium submodel in OTEQ is based on MINTEQA2 (Allison and others, 1991), an extension of the MINEQL computer code developed by Westall and others (1976). Given analytical concentrations of the chemical components, MINTEQA2 computes the distribution of chemical species that exist within a batch reactor at equilibrium. These equilibrium computations include the precipitation and dissolution of solid phases as well as sorption processes. The mass-balance and mass-action equations, describing the different solution-mineral equilibria, form a set of non-linear algebraic equations (AEs).

Coupling transport with chemical equilibrium results in a simultaneous set of AEs and PDEs. The sequential iteration approach (Yeh and Tripathi, 1989) solves the coupled set of equations by dividing each time step into a "reaction" step and a "transport" step. During the reaction step, the equilibrium submodel is applied to each segment in the study reach. Each segment represents a batch reactor wherein chemical equilibrium is assumed. The equilibrium submodel thus determines the solute mass in dissolved, precipitated, and sorbed forms. On the basis of this information, a transport step is applied in which the solute-transport algorithm determines the physical transport of the mobile phases of each solute. Because the transport and reaction steps neglect the coupling of the transport and chemistry, the procedure iterates until a specified level of convergence is achieved.

The governing equations and solution algorithms used within the reactive solute-transport code are based on the following assumptions:

- Complexation, precipitation/dissolution, and sorption reactions are assumed to be in a state of local equilibrium (Korzhinskii, 1959; Fitts, 1962; Hanley, 1967; DiToro, 1976; Rubin, 1983; Bahr and Rubin, 1987).
- Solute mass is uniformly distributed over the stream's cross-sectional area such that one-dimensional transport is applicable. The physical processes that affect solute mass in each stream segment include advection, dispersion, lateral inflow, transient storage, and settling. All dissolved, precipitated, and sorbed species resident in the water column travel at the same advective velocity.
- Solute mass for each chemical component is distributed among five distinct phases. The first three phases represent dissolved, precipitated, and sorbed mass that is present in the water column. These three phases are mobile, in that they are subject to transport. The final two phases represent precipitated and sorbed mass that resides on the streambed or is attached to stationary debris in the stream channel; these phases are immobile and are not transported.

- Dissolved mass in the water column may form precipitates if the solution becomes oversaturated with respect to the defined solid phases. Any precipitated mass initially resides in the water column and is subject to solid-phase transport until it settles to the streambed or redissolution occurs. Precipitated mass may accumulate on the bed, however, as transported precipitates are subject to the force of gravity and settle at a rate defined by a settling velocity.
- Dissolved species may sorb to solid phases in the water column or to sorption sites on the streambed. Conversely, sorbed species may desorb from sites in the water column or on the streambed. Runkel and others (1999) discuss additional assumptions relative to sorption.

The fundamental equations that govern reactive-solute transport are derived based on the above assumptions. Governing equations are formulated in terms of the chemical components defined within the equilibrium submodel. The total component concentration, T, in moles/liter, is the sum of the five individual component phase concentrations, with each phase consisting of one or more chemical species:

$$T = C + P_w + P_b + S_w + S_b \tag{10}$$

where C is the dissolved phase;
P_w is the mobile precipitate;
P_b is the immobile precipitate;
S_w is the mobile sorbed phase; and
S_b is the immobile sorbed phase.

A summary of the processes considered for each phase is illustrated in figure 25, where the system is represented as two compartments. The water column compartment contains the three mobile phases, C, P_w, and S_w; the immobile substrate (the streambed or debris) compartment contains the two immobile phases, P_b and S_b. The three mobile phases are subject to physical transport (advection, dispersion, transient storage, and lateral inflow), as represented by the transport operator, $L(T)$. The dissolved phase, C, takes part
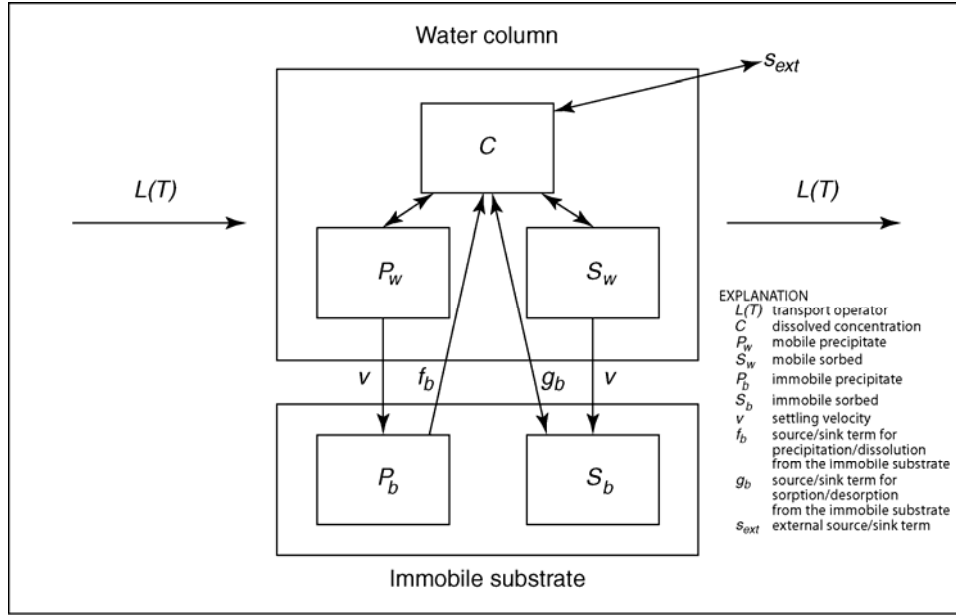
Figure 25. Conceptual model of a surface-water system.

in precipitation/dissolution and sorption/desorption reactions that occur within the water column (interactions with P_w and S_w). The dissolved phase also is affected by dissolution of precipitate from the immobile substrate and sorption/desorption from immobile sorbents (interactions with P_b and S_b). Finally, C may increase or decrease because of external sources and sinks (gas exchange for example), as denoted by s_{ext}. The precipitated and sorbed phases in the water column settle in accordance with settling velocity v [$L\ T^{-1}$].

The mass-balance equation for the total component concentration T is obtained by summing the mass-balance equations for the five individual component phases. This yields:

$$\frac{\partial T}{\partial t} = L(T) - L(P_b + S_b) + s_{ext} \qquad (11)$$

where $L(T)$ is the transport operator, defined in terms of the transient storage model (Bencala and Walters, 1983; Runkel, 1998) and s_{ext} is a source/sink term representing external gains and losses [moles/liter T^{-1}]. The immobile precipitated and sorbed concentrations in equation 11 are governed by:

$$\frac{\partial P_b}{\partial t} = \frac{v}{d}(P - P_b) - f_b \qquad (12)$$

$$\frac{\partial S_b}{\partial t} = \frac{v}{d}(S - S_b) - g_b , \qquad (13)$$

where

f_b is the source/sink term for dissolution from the immobile substrate (M L^{-3} T^{-1}),

g_b is the source/sink term for sorption-desorption from the immobile substrate (M L^{-3} T^{-1}),

v is the settling velocity (L T^{-1}),

d is the settling depth (L),

P is the total precipitate concentration (equal to P_w plus P_b), and

S is the total sorbed concentration (equal to S_w plus S_b).

The set of governing equations thus consists of three PDEs for each component (for T, P_b, and S_b) and the set of AEs representing chemical equilibria. This set of equations is solved by using the sequential iteration approach with a Crank-Nicolson approximation of the PDEs (Runkel and others, 1996a).

34

Input data include mixing parameters (dispersion and transient storage), streamflow estimates, lateral inflow concentrations, upstream boundary conditions, and geochemical parameters. Steady-state analyses under the assumption of chemical equilibrium are generally insensitive to mixing parameters, such that these parameters are not discussed here. The remaining inputs are discussed in the following sections. Most parameters are allowed to vary spatially on a reach-by-reach basis.

Reaches

The six stream sections for reactive-transport modeling (three stream sections per study) were chosen to include processes relevant to the objectives of the study. Lengths of the stream sections for reactive-transport modeling differed from those discussed previously for the tracer-injection/synoptic sampling. The lengths of the respective upper, middle, and lower sections chosen were 6.5, 7.9, and 7.5 km for the August 2001 study, and 2.2, 2.8, and 4.5 km for the March/April 2002 study. Each of the six stream sections from the two synoptic studies was divided into several model reaches for the reactive transport simulations. A model reach is defined as a length of the stream with homogeneous physical properties in which model parameters are spatially constant. Each model reach is further subdivided into several segments (control volumes) to which the governing equations apply.

Model reaches, distances, streamflows, sources of inflow compositions used as input, and iron(II) percentages used as input are presented in tables 2 to 4 for the August 2001 simulations, and in tables 5 to 7, absent the iron(II) percentages, for the March/April 2002 simulations. For the August 2001 transport simulations the upper, middle, and lower stream sections were divided into 25, 19, and 23 model reaches, respectively. For the March/April 2002 transport simulations the upper, middle, and lower stream sections were divided into 7, 14, and 16 model reaches, respectively. Discharges were assigned to inflows based on the results of Red River main stem bromide concentrations obtained from the tracer injection experiment.

Simulated Solutes and Sorbents

OTEQ simulations were done using a 14-component set consisting of total excess hydrogen [H_T^+], dissolved inorganic carbon (DIC) as carbonate, dissolved calcium, chloride, fluoride, iron(II), magnesium, manganese, sodium, and sulfate; and total-recoverable aluminum, copper, zinc, and iron(III). Total-recoverable iron(III) was calculated by differencing the total-recoverable iron(total) and dissolved iron(II) results. This approach is consistent with previous OTEQ simulations for streams receiving mine drainage (Broshears and others, 1996; Runkel and others, 1996b; Ball and others, 2004).

For the March/April 2002 tracer, total dissolved iron concentrations were near method detection limits and iron(II) concentrations were below method detection limits. Thus, for the March/April 2002 simulations total iron was input as iron(III), only 13 components were considered, and iron redox processes were not simulated. For the August 2001 simulations transfer of mass between iron(II) and iron(III) resulting from redox processes was computed by specifying, for each model reach, the fraction of dissolved iron(total) [iron(II) + iron(III)] that is iron(II). The mass of sorbent within each stream reach was based on the amount of iron(III) precipitated within the water column [suspended iron(III) oxyhydroxide] in that reach, as determined by the chemical-equilibrium calculations. For the simulations, all the iron(III) precipitated within the water column remained in the water column, that is, none was settled to the stream bed. Precipitated iron(III) on the streambed was assumed to be saturated with respect to sorbed species and therefore was not a sink in the steady-state analysis presented in this report. Future substantial changes in the Red River water chemistry could require reconsidering these assumptions.

Lateral Inflow Concentrations

Most reaches included one or more observed surface inflows that were used to set component inflow concentrations. Inflow chemical compositions used to set component concentrations are identified in tables 2 to 7.

Table 2. Model reaches for the August 2001 upper stream section, including streamflow, inflows, and iron(II) percentages.

[m, meters; L/s, liters per second; starting distance for this stream section was 0 meters]

Reach	Cumulative distance [m]	Streamflow [L/s] Upstream end of reach	Within reach increase	Inflow chemistry used[1]	Iron(II) percentage
1	200	395.4	0.0	None	72.5
2	324	395.4	13.4	Small inflow among willows at 340 m	72.6
3	375	408.8	8.4		72.7
4	518	417.2	26.0	Average of spring in fill material at 380 m and culvert upstream from Riverside Lodge at 511 m	72.8
5	700	443.2	5.9	Upwelling near concrete block among Al precipitation at 530 m	73.0
6	800	449.1	12.9	Small pool in moss bank at 750 m	73.1
7	900	462.0	0.1	Seep with algae above bridge at 705 m	73.2
8	1,040	462.1	7.4		73.3
9	1,100	469.5	6.4	Culvert with orange precipitate at 1,050 m	73.4
10	1,200	475.9	13.0		73.5
11	1,300	488.9	0.0	None	73.6
12	1,640	488.9	7.6	Small inflow among willows at 1,463 m	73.9
13	1,765	496.5	8.1	Spring with Fe precipitate at 1,658 m	74.1
14	1,975	504.6	0.0	None	74.3
15	2,184	504.6	0.3	Spring with Fe precipitate at 1,658 m	74.5
16	2,404	504.9	60.0	Pioneer Creek, 2,195 m	74.7
17	3,350	564.9	-47.3	None	75.3
18	4,200	517.6	-42.5		76.2
19	4,500	475.1	3.2	Pioneer Creek, 2,195 m	76.8
20	4,800	478.3	0.0	None	77.1
21	4,900	478.3	2.9	Pioneer Creek, 2,195 m	77.2
22	5,200	481.2	6.0	Pioneer Creek, 2,195 m	77.5
23	5,300	487.2	4.5	Pioneer Creek, 2,195 m	77.6
24	5,735	491.7	0.2	Pioneer Creek, 2,195 m	78.0
25	6,500	491.9	0.2	Pioneer Creek, 2,195 m	78.4

[1]Sample site descriptions and concentrations of inflow constituents can be found in McCleskey and others (2003)

Table 3. Model reaches for the August 2001 middle stream section, including streamflow, inflows, and iron(II) percentages.

[m, meters; L/s, liters per second; starting distance for this stream section was 5,756 meters]

Reach	Cumulative distance [m]	Streamflow [L/s] Upstream end of reach	Within reach increase	Inflow chemistry used[1]	Iron(II) percentage
1	6,000	562.4	0.0	None	80.2
2	6,175	562.4	0.0		79.7
3	6,300	562.4	64.2	Seep draining toe of Hansen debris fan at 6,214 m	79.3
4	6,600	626.6	5.1	Draining upstream of altered cliffs on left bank at 6,343 m	79.1
5	6,819	631.7	10.0		78.5
6	7,100	641.7	11.8		78.1
7	7,200	653.5	5.0	Small spring along right bank at 7,270 m	77.5
8	7,295	658.5	7.1		77.3
9	7,395	665.6	2.5	Small ditch draining left bank at 7,300 m	77.1
10	7,500	668.1	7.6	Waldo Spring pool, 7,457 m	76.9
11	7,800	675.7	8.3	Draining from hillslope away from stream at 7,588 m	76.7
12	8,100	684.0	0.0	None	76.1
13	8,700	684.0	6.9	Seep near downstream end of mill yard at 10,360 m	75.5
14	10,300	690.9	0.2		74.6
15	10,500	691.1	5.9		72.3
16	10,800	697.0	18.5	Seepage with pond full of algae at 10,519 m	70.8
17	12,200	715.5	0.0	None	70.4
18	13,194	715.5	10.0	Portal Springs, 12,308 m	68.6
19	13,694	725.5	5.0		66.2

[1]Sample site descriptions and concentrations of inflow constituents can be found in McCleskey and others (2003)

Table 4. Model reaches for the August 2001 lower stream section, including streamflow, inflows, and iron(II) percentages.

[m, meters; L/s, liters per second; starting distance for this stream section was 12,515 meters]

Reach	Cumulative distance [m]	Streamflow [L/s] Upstream end of reach	Streamflow [L/s] Within reach increase	Inflow chemistry used[1]	Iron(II) percentage
1	12,900	798.3	0.0	None	69.7
2	13,194	798.3	6.3	Columbine Creek, 13,210 m	67.5
3	13,300	804.6	168.9		67.1
4	13,600	973.5	6.3		65.8
5	13,700	979.8	0.0	None	65.4
6	13,900	979.8	22.7	Pond with filamentous algae draining to stream at 19,040 m	64.6
7	14,142	1,002.5	0.03	Shaft Spring, 14,570 m	63.6
8	14,700	1,002.5	6.7		61.9
9	14,790	1,009.2	14.3	Spring draining willows along left bank at 14,800 m	60.9
10	14,958	1,023.5	56.0	Discharge from beaver pond at 15,331 m	60.2
11	15,285	1,079.5	56.3	Spring above Thunder Bridge at 15,044 m	59.0
12	15,373	1,135.8	6.8	Discharge from beaver pond at 15,331 m	58.5
13	15,600	1,142.6	44.5	Ponded water in alluvium on left bank at 15,500 m	57.6
14	15,765	1,187.1	12.1	Pond with old metal relic at 15,687 m	56.9
15	16,100	1,199.2	0.0	None	55.5
16	17,480	1,199.2	17.3	Discharge from French drain at 17,574 m	51.9
17	18,000	1,216.5	16.5	Ponded water in alluvium on left bank at 15,500 m	48.5
18	18,300	1,233.0	1.8	Seeps along right bank at 18,160 m	46.4
19	18,600	1,234.8	0.0	None	45.2
20	19,170	1,234.8	6.9	Pond with filamentous algae draining to stream at 19,040 m	43.4
21	19,500	1,241.7	-60.3	None	41.5
22	19,780	1,181.4	0.0		40.3
23	20,000	1,181.4	0.0		39.4

[1]Sample site descriptions and concentrations of inflow constituents can be found in McCleskey and others (2003)

Table 5. Model reaches for the March/April 2002 upper stream section, including streamflow and inflows.

[m, meters; L/s, liters per second; starting distance for this stream section was 3,225 meters]

Reach	Cumulative distance [m]	Streamflow [L/s] Upstream end of reach	Within reach increase	Inflow chemistry used[1]
1	3,900	307.1	0.0	None
2	4,200	307.1	0.0	
3	4,500	315.9	8.8	Red River at 4,200 m
4	4,800	321.2	5.3	Red River at 4,500 m
5	5,200	325.1	3.9	Red River at 4,800 m
6	5,300	330.5	5.4	Red River at 5,200 m
7	5,400	335.9	5.4	Red River at 5,300 m

[1]Sample site descriptions and concentrations of inflow constituents can be found in McCleskey and others (2003)

Table 6. Model reaches for the March/April 2002 middle stream section, including streamflow and inflows.

[m, meters; L/s, liters per second; starting distance for this stream section was 5,756 meters]

Reach	Cumulative distance [m]	Streamflow [L/s] Upstream end of reach	Within reach increase	Inflow chemistry used[1]
1	6,021	233.5	0.0	None
2	6,196	233.5	0.0	
3	6,321	233.5	35.1	Seep draining right bank upstream of Hansen fan at 6,214 m
4	6,621	268.6	7.4	Drainage upstream from altered cliffs on left bank at 6,343 m
5	6,840	276.0	0.0	None
6	6,961	276.0	1.9	Drainage upstream from altered cliffs on left bank at 6,343 m
7	7,121	277.9	4.9	
8	7,221	282.8	5.1	Small right bank seep with Fe stain at 7,150 m
9	7,316	287.9	5.2	Drainage near well on right bank at 7,240 m
10	7,398	293.1	6.6	Seep from right bank with algae at 7,297 m
11	7,521	299.7	8.1	
12	7,821	307.8	2.3	Right bank input draining from hillslope away from stream at 7,588 m
13	8,421	310.1	3.7	
14	8,521	313.8	0.6	

[1]Sample site descriptions and concentrations of inflow constituents can be found in McCleskey and others (2003)

Table 7. Model reaches for the March/April 2002 lower stream section, including streamflow and inflows.

[m, meters; L/s, liters per second; starting distance for this stream section was 13,300 meters]

		Streamflow [L/s]		
Reach	Cumulative distance [m]	Upstream end of reach	Within reach increase	Inflow chemistry used[1]
1	14,142	295.9	0.0	None
2	15,084	295.9	0.0	
3	15,221	295.9	17.7	Left bank seep at base of stream bank at 15,141 m
4	15,373	313.6	39.8	Right bank seep near start of fan from Goathill Gulch at 15,264 m
5	15,547	353.4	23.1	
6	15,600	376.5	2.2	Pond on left bank near river, birch at bank at 15,567 m
7	15,765	378.7	2.5	
8	15,950	381.2	2.0	Right bank seep near start of fan from Goathill Gulch at 15,264 m
9	16,700	383.2	2.4	
10	17,012	385.6	10.2	
11	17,230	395.8	2.8	
12	17,300	398.6	4.1	
13	17,480	402.7	4.6	Right bank seep with Al precipitate at 17,270 m
14	17,655	407.3	13.8	Spring at old tree stump at 17,574 m
15	17,700	421.1	0.0	None
16	17,800	421.1	0.0	

[1]Sample site descriptions and concentrations of inflow constituents can be found in McCleskey and others (2003)

When more than one inflow was available for a given reach, the largest observed inflow was generally used. In one instance (table 2, reach 4), the average of two compositions was used as input to the computer code. For chemical compositions of all surface inflows, DIC and H_T^+ were calculated by running standalone MINTEQA2 simulations with pH fixed at measured values and dissolved carbonate species either calculated from alkalinity titration results where available, or assumed to be at equilibrium with atmospheric CO_2 for instances where samples contained no measurable alkalinity. Measured concentrations of dissolved calcium, chloride, fluoride, iron(II), magnesium, manganese, sodium, and sulfate, and total-recoverable aluminum, copper, iron(III), and zinc were used to set component concentrations in all inflows.

Of the 67 stream reaches considered for the August 2001 simulations, 17 were reaches where there was no change in the discharge, as calculated from the Br tracer data; thus, no water-chemistry data were needed as input. Of the remaining 50 reaches, 23 were reaches for which increases in discharge were detected, either with the bromide tracer results or using a current meter, but no surface inflows were observed or sampled. For these 23 reaches, inflow concentrations usually were estimated by using the composition of a nearby surface inflow source. In some cases none of the nearby inflow compositions were appropriate to achieve a reasonable simulated fit to the concentrations measured in the Red River.

Many of the available water sources were seeps and springs near the Red River main stem, some of which could not be conclusively

established to flow directly into the Red River. To a first approximation such seeps and springs may be inferred to represent nearby ground-water compositions that may affect the stream-water quality. What cannot be determined are flow paths for ground water that evidently discharged into the Red River along stream reaches that had no visible inflow source but were known from the bromide tracer results to increase in discharge. When poor simulated fits occurred, alternative inflow compositions were chosen from among a wider range of candidate inflow sources. Mass-loading and confluence-mass-balance calculations were used to compare inflow compositions with the chemistry of the Red River at these locations as an aid in choosing appropriate inflow compositions.

For the March/April 2002 simulations, of the 37 stream reaches considered, 8 were reaches where there was no change in the discharge, as calculated from the bromide tracer data; thus, no input water chemistry data were needed. No surface inflows were observed or sampled for 12 of the remaining 29 reaches. Thus, inflow concentrations were estimated for these 12 reaches by using the composition of an appropriate surface inflow source as determined using mass-balance calculations in a manner similar to that described above. No surface inflow features were observed for any of the 7 reaches of the upper section for the March/April 2002 simulation. Thus, for the lower 5 model reaches where increases in flow were detected, chemical data from the Red River main stem were used as lateral inflow input. Because this approach yielded acceptable simulation results no alternative inflow sources were needed. For both the August 2001 and March/April 2002 simulations, in instances where the initial chosen inflow composition failed to yield an adequate simulation of observed concentrations in the Red River, alternative inflows were substituted until the best simulation of observed concentrations was achieved for all chemical components.

Upstream Boundary Conditions

Upstream boundary conditions were set to the respective measured dissolved calcium, fluoride, iron(II), magnesium, manganese, sodium, and sulfate, and total-recoverable aluminum, copper, iron(III), and zinc concentrations in the Red River above the injection point. Values for H_T^+ and DIC were obtained as described in the previous section. Upstream-boundary-condition concentrations used for the final calibration runs for August 2001 and March/April 2002 simulations are listed in table 8.

At the upstream boundary the mass of sorbent within the water column was based on the amount of precipitated iron(III), as determined by total-recoverable iron determinations. Red River water at the upstream boundary and several inflows contained suspended material thought to be mostly hydrous ferric oxide (HFO). In order to include suspended material from these sources in the OTEQ simulations, it was necessary to create an upstream or inflow boundary condition that had both the selected simulation pH and the appropriate amount of suspended HFO. This boundary condition was calculated by a separate MINTEQA2 simulation in which the equilibrium solution was modified by changing the metal concentrations to their total-recoverable values. The separate MINTEQA2 simulation was a manual-iteration scheme in which MINTEQA2 was run repeatedly while varying the input H_T^+ until the correct pH and amount of precipitation of iron and aluminum phases were simulated. When the correct input H_T^+ was achieved, as reflected in the targets of pH and solid phase precipitation, the H_T^+ and the total-recoverable iron and aluminum concentrations were used in the OTEQ upstream or inflow boundary condition. This approach is appropriate for any inflow carrying a substantial amount of sorbent in the water column.

Streamflow Parameters

Streamflow estimates (tables 2 to 7) were based on Br concentrations measured in samples collected at numerous points along the Red River. These streamflow estimates were compared with instantaneous discharges measured at several points along the Red River during the tracer-injection synoptic study. For the August 2001 tracer study, one stream reach was identified as a losing reach, a condition that cannot be accounted for using the tracer dilution method of determining stream discharge. Thus, for the

Table 8. Upstream boundary condition concentrations above injection points.

[concentration in moles per liter]

Component	August 2001 Tracer			March/April 2002 Tracer		
	Upper	Middle	Lower	Upper	Middle	Lower
Dissolved						
SO_4	1.538E-04	5.150E-04	7.736E-04	6.736E-04	7.114E-04	8.020E-04
Fe(II)	0.000E+00	1.007E-07	0.000E+00	---[1]	---[1]	---[1]
Ca	7.735E-04	8.483E-04	9.980E-04	8.982E-04	8.982E-04	9.480E-04
Mg	1.851E-04	2.838E-04	3.208E-04	3.373E-04	3.537E-04	3.460E-04
Na	1.131E-04	1.914E-04	2.262E-04	2.349E-04	2.784E-04	---[1]
F	3.475E-06	5.150E-04	1.834E-05	1.613E-05	1.508E-05	1.421E-05
Cl	2.941E-05	6.229E-05	7.806E-05	8.970E-05	1.066E-04	---[1]
Mn	3.640E-08	1.511E-06	2.002E-06	2.912E-06	2.366E-06	2.190E-06
H^+_T	8.5970E-04	1.1865E-03	4.2806E-04	1.3574E-03	1.1149E-03	1.0071E-03
DIC	8.624E-04	1.277E-03	5.917E-04	1.442E-03	1.216E-03	1.095E-03
Total Recoverable						
Al	1.853E-06	1.334E-05	3.261E-05	1.779E-05	1.668E-05	2.520E-05
Fe(III)	8.953E-07	1.011E-05	2.328E-05	5.909E-06	6.804E-06	2.510E-06
Cu	6.310E-09	1.350E-07	1.198E-07	2.097E-07	2.426E-07	1.390E-07
Zn	0.000E+00	3.212E-07	4.436E-07	6.272E-07	5.201E-07	4.590E-07

[1]This constituent not modeled for this instance.

August 2001 tracer study discharges in the stream reaches downstream from Pioneer Creek were adjusted to be consistent with current-meter discharge measurements. Methods and approaches for adjusting discharges for losing stream reaches are discussed by Runkel and others (2003).

Geochemical Parameters

Temperature and ionic strength are spatially invariant within OTEQ. Therefore, the average temperature measured during the course of the synoptic samplings and the average ionic strength calculated by MINTEQA2 (table 9) were used to set these two parameters for each of the six simulations.

For the August 2001 simulations equilibrium with atmospheric CO_2 was found to reproduce measured pH values better than dissolved carbonate concentrations and thus was specified. For the March/April 2002 simulations adequate fits to measured pH values were obtained without specifying equilibrium with atmospheric CO_2.

Table 9. Temperature and ionic strength for the OTEQ simulations.

[°C, degrees Celsius; M, moles per liter]

| Simulation	Reach	Temperature [°C]	Ionic Strength [M]
August 2001	Upper	9.0	0.003
August 2001	Middle	12	0.004
August 2001	Lower	12	0.004
April 2002	Upper	10.8	0.0044
March 2002	Middle	7.8	0.0044
March 2002	Lower	9.0	0.00456

Thermodynamic Data

The thermodynamic data base for aqueous complexes and ion activity product calculations was that of MINTEQA2 (Allison and others, 1991) modified using the data from Nordstrom and others (1990), Ball and Nordstrom (1991), and Nordstrom and May (1996). The complete set of thermodynamic data relevant to the dissolved components used for the OTEQ simulations is presented in table 10.

Investigations of white aluminous precipitates in acid mine waters indicate that this material can be approximated most closely by either amorphous to crystalline aluminum hydroxide [$Al(OH)_3$] or amorphous basaluminite [$Al_4(OH)_{10}SO_4$] (Singh, 1969; Singh and Brydon, 1970; Adams and Rawajfih, 1977; Nordstrom, 1982; Nordstrom and others, 1984). The following two reactions were used to define the precipitating phases for the OTEQ simulations:

$$Fe^{3+} + 3H_2O = Fe(OH)_3 + 3H^+, \qquad (14)$$

and

$$Al^{3+} + 3H_2O = Al(OH)_3 + 3H^+. \qquad (15)$$
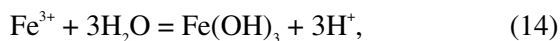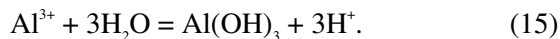
Ferrihydrite and poorly crystalline to amorphous aluminum hydroxide were used as the respective iron and aluminum precipitating phases for both the August 2001 and March/April 2002 simulations. The MINTEQA2 default log $K°$ value of -4.891 for the solubility equilibrium constant for ferrihydrite was used in the simulations. Initially, the log $K°$ value of -9.35 for microcrystalline gibbsite solubility (Nordstrom and others, 1990) was used in the simulations. This log $K°$ value, which yielded consistently positive saturation indices from WATEQ4F, also yielded OTEQ dissolved aluminum concentrations significantly lower than those measured in the Red River. Based on the geochemical speciation modeling results discussed earlier, a log $K°$ value of -9.8 was chosen empirically for the precipitating aluminum hydroxide phase. This value is intermediate between the log $K°$ values for microcrystalline gibbsite (-9.35) and amorphous $Al(OH)_3$ (-10.8).

Sorbent concentrations were based on the simulated concentration of precipitated HFO in each stream segment. The sorption data base was that of Dzombak and Morel (1990). Initial simulations using the best estimates of Dzombak and Morel resulted in underprediction of copper sorption. The high affinity site density was therefore increased to the upper value reported by Dzombak and Morel to reflect the high sorptive capacity of freshly precipitated iron oxides (Runkel and others, 1999; Runkel and Kimball, 2002; Ball and others, 2004).

Reduction-Oxidation Parameters for Iron

Iron(II) was not included in the March/April 2002 simulations because in most cases dissolved iron concentrations in the Red River were below detection. For the August 2001 simulations, iron(II) was simulated to oxidize concurrently with iron(III) hydrolysis and precipitation to achieve a ratio of dissolved iron(II) to dissolved iron(total) consistent with measured dissolved concentrations of iron(II) and iron(total) at several locations in the main stem of Red River. The dissolved iron(II)/iron(total) ratio was fixed to approximate the measured dissolved concentrations of iron(II) and iron(total) for the main stem at the end of each model reach. Ratio values (tables 2 to 4) for input to OTEQ were calculated from the slope and intercept of a least-squares linear regression of the measured dissolved iron(II)/iron(total) ratios as a function of distance. The relations between dissolved iron(II)/iron(total) ratios calculated from the measured dissolved iron(II) and dissolved iron(total) values and those derived from the least-squares linear regression are shown in figures 26 to 28. Scatter in the dissolved iron redox species determinations, and thus in the dissolved iron(II)/iron(total) ratios, has two likely sources: (1) low dissolved iron concentrations in the Red River; and (2) sample storage in containers that may have been contaminated with small but measurable amounts of iron (McCleskey and others, 2003; 2004).

Table 10. Thermodynamic data used by MINTEQA2 for modeling aqueous speciation.

[References are: 1, Allison and others (1991); 2, Nordstrom and May (1996); 3, Nordstrom and others (1990); ΔH, enthalpy of reaction, in kilocalories per mole; K equilibrium constant for the reaction]

Aqueous Species	Reaction	ΔH	Log K	Analytical Expression	Refer-ence
OH^-	$H_2O \leftrightarrows H^+ + OH^-$	13.345	-13.998		1
$MgOH^+$	$Mg^{2+} + H_2O \leftrightarrows MgOH^+ + H^+$	15.952	-11.44	$Log\ K_{MgOH+} = -3.53 + 0.00513T - 2917.1/T$	1
MgF^+	$Mg^{2+} + F^- \leftrightarrows MgF^+$	4.674	1.82		1
$MgCO_3^\circ$	$Mg^{2+} + CO_3^{2-} \leftrightarrows MgCO_3^\circ$	2.022	2.98	$Log\ K_{MgCO3^\circ} = 0.991 + 0.00667T$	1
$MgHCO_3^+$	$Mg^{2+} + H^+ + CO_3^{2-} \leftrightarrows MgHCO_3^+$	-2.43	11.4	$Log\ K_{MgHCO3+} = -4.179 + 0.012734T + 2902.39/T + 0.0000229812T^2$	1
$MgSO_4^\circ$	$Mg^{2+} + SO_4^{2-} \leftrightarrows MgSO_4^\circ$	1.399	2.25		1
$CaOH^+$	$Ca^{2+} + H_2O \leftrightarrows CaOH^+ + H^+$	14.535	-12.598		1
$CaHCO_3^+$	$Ca^{2+} + H^+ + CO_3^{2-} \leftrightarrows CaHCO_3^+$	1.79	11.33	$Log\ K_{CaHCO3+} = -9.448 + 0.03709T + 2902.39/T$	1
$CaCO_3^\circ$	$Ca^{2+} + CO_3^{2-} \leftrightarrows CaCO_3^\circ$	4.03	3.15	$Log\ K_{CaCO3^\circ} = -27.393 + 0.05617T + 4114/T$	1
$CaSO_4^\circ$	$Ca^{2+} + SO_4^{2-} \leftrightarrows CaSO_4^\circ$	1.65	2.3		1
CaF^+	$Ca^{2+} + F^- \leftrightarrows CaF^+$	3.798	0.94		1
$NaCO_3^-$	$Na^+ + CO_3^{2-} \leftrightarrows NaCO_3^-$	8.911	1.268		1
$NaHCO_3^\circ$	$Na^+ + H^+ + CO_3^{2-} \leftrightarrows NaHCO_3^\circ$	0	10.08		1
$NaSO_4^-$	$Na^+ + SO_4^{2-} \leftrightarrows NaSO_4^-$	1.12	0.7		1
NaF°	$Na^+ + F^- \leftrightarrows NaF^\circ$	0	0.24		1
$AlOH^{2+}$	$Al^{3+} + H_2O \leftrightarrows AlOH^{2+} + H^+$	11.49	-5		2
$Al(OH)_2^+$	$Al^{3+} + 2H_2O \leftrightarrows Al(OH)_2^+ + 2H^+$	26.9	-10.1		2
$Al(OH)_4^-$	$Al^{3+} + 4H_2O \leftrightarrows Al(OH)_4^- + 4H^+$	43.38	-22.99		2
AlF^{2+}	$Al^{3+} + F^- \leftrightarrows AlF^{2+}$	1.06	7		2
AlF_2^+	$Al^{3+} + 2F^- \leftrightarrows AlF_2^+$	1.98	12.7		2
AlF_3°	$Al^{3+} + 3F^- \leftrightarrows AlF_3^\circ$	2.16	16.8		2
AlF_4^-	$Al^{3+} + 4F^- \leftrightarrows AlF_4^-$	2.2	19.4		2
$AlSO_4^+$	$Al^{3+} + SO_4^{2-} \leftrightarrows AlSO_4^+$	2.29	3.5		2
$Al(SO_4)_2^-$	$Al^{3+} + 2SO_4^{2-} \leftrightarrows Al(SO_4)_2^-$	3.11	5		2
$Al(OH)_3^\circ$	$Al^{3+} + 3H_2O \leftrightarrows Al(OH)_3^\circ + 3H^+$	39.89	-16.9		2
$FeOH^+$	$Fe^{2+} + H_2O \leftrightarrows FeOH^+ + H^+$	13.199	-9.5		3
$Fe(OH)_3^-$	$Fe^{2+} + 3H_2O \leftrightarrows Fe(OH)_3^- + 3H^+$	30.3	-31		3
$FeSO_4^\circ$	$Fe^{2+} + SO_4^{2-} \leftrightarrows FeSO_4^\circ$	3.23	2.25		3
$Fe(OH)_2^\circ$	$Fe^{2+} + 2H_2O \leftrightarrows Fe(OH)_2^\circ + 2H^+$	28.565	-20.57		3
$FeOH^{2+}$	$Fe^{3+} + H_2O \leftrightarrows FeOH^{2+} + H^+$	10.399	-2.19		3

Table 10. Thermodynamic data used by MINTEQA2 for modeling aqueous speciation--Continued.

Aqueous Species	Reaction	ΔH	Log K	Analytical Expression	Reference
$FeSO_4^+$	$Fe^{3+} + SO_4^{2-} \leftrightarrows FeSO_4^+$	3.91	4.04		3
$FeCl^{2+}$	$Fe^{3+} + Cl^- \leftrightarrows FeCl^{2+}$	5.6	1.48		3
$FeCl_2^+$	$Fe^{3+} + 2Cl^- \leftrightarrows FeCl_2^+$	0	2.13		3
$FeCl_3^\circ$	$Fe^{3+} + 3Cl^- \leftrightarrows FeCl_3^\circ$	0	1.13		3
$Fe(OH)_2^+$	$Fe^{3+} + 2H_2O \leftrightarrows Fe(OH)_2^+ + 2H^+$	17.1	-5.67		3
$Fe(OH)_3^\circ$	$Fe^{3+} + 3H_2O \leftrightarrows Fe(OH)_3^\circ + 3H^+$	24.8	-12.56		3
$Fe(OH)_4^-$	$Fe^{3+} + 4H_2O \leftrightarrows Fe(OH)_4^- + 4H^+$	31.9	-21.6		3
FeF^{2+}	$Fe^{3+} + F^- \leftrightarrows FeF^{2+}$	2.699	6.199		3
FeF_2^+	$Fe^{3+} + 2F^- \leftrightarrows FeF_2^+$	4.8	10.8		3
FeF_3°	$Fe^{3+} + 3F^- \leftrightarrows FeF_3^\circ$	5.399	14		3
$Fe(SO_4)_2^-$	$Fe^{3+} + 2SO_4^{2-} \leftrightarrows Fe(SO_4)_2^-$	4.6	5.38		3
$Fe_2(OH)_2^{4+}$	$2Fe^{3+} + 2H_2O \leftrightarrows Fe_2(OH)_2^{4+} + 2H^+$	13.5	-2.95		3
$Fe_3(OH)_4^{5+}$	$3Fe^{3+} + 4H_2O \leftrightarrows Fe_3(OH)_4^{5+} + 4H^+$	14.3	-6.3		3
$MnCl^+$	$Mn^{2+} + Cl^- \leftrightarrows MnCl^+$	0	0.607		1
$MnCl_2^\circ$	$Mn^{2+} + 2Cl^- \leftrightarrows MnCl_2^\circ$	0	0.025		1
$MnCl_3^-$	$Mn^{2+} + 3Cl^- \leftrightarrows MnCl_3^-$	0	-0.31		1
$MnOH^+$	$Mn^{2+} + H_2O \leftrightarrows MnOH^+ + H^+$	14.399	-10.59		1
$Mn(OH)_3^-$	$Mn^{2+} + 3H_2O \leftrightarrows Mn(OH)_3^- + 3H^+$	0	-34.8		1
MnO_4^-	$Mn^{2+} + 4H_2O \leftrightarrows MnO_4^- + 8H^+ + 5e^-$	176.62	-127.824		1
MnO_4^{2-}	$Mn^{2+} + 4H_2O \leftrightarrows MnO_4^{2-} + 8H^+ + 4e^-$	150.02	-118.44		1
MnF^+	$Mn^{2+} + F^- \leftrightarrows MnF^+$	0	0.85		1
$MnSO_4^\circ$	$Mn^{2+} + SO_4^{2-} \leftrightarrows MnSO_4^\circ$	2.17	2.26		1
$MnHCO_3^+$	$Mn^{2+} + H^+ + CO_3^{2-} \leftrightarrows MnHCO_3^+$	0	11.6		1
$CuCl_2^-$	$Cu^+ + 2Cl^- \leftrightarrows CuCl_2^-$	-0.42	5.5		1
$CuCl_3^{2-}$	$Cu^+ + 3Cl^- \leftrightarrows CuCl_3^{2-}$	0.26	5.7		1
$CuCO_3^\circ$	$Cu^{2+} + CO_3^{2-} \leftrightarrows CuCO_3^\circ$	0	6.73		1
$Cu(CO_3)_2^{2-}$	$Cu^{2+} + 2CO_3^{2-} \leftrightarrows Cu(CO_3)_2^{2-}$	0	9.83		1
$CuCl^+$	$Cu^{2+} + Cl^- \leftrightarrows CuCl^+$	8.65	0.43		1
$CuCl_2^\circ$	$Cu^{2+} + 2Cl^- \leftrightarrows CuCl_2^\circ$	10.56	0.16		1
$CuCl_3^-$	$Cu^{2+} + 3Cl^- \leftrightarrows CuCl_3^-$	13.69	-2.29		1

Table 10. Thermodynamic data used by MINTEQA2 for modeling aqueous speciation--Continued.

Aqueous Species	Reaction	ΔH	Log K	Analytical Expression	Reference
$CuCl_4^{2-}$	$Cu^{2+} + 4Cl^- \leftrightarrows CuCl_4^{2-}$	17.78	-4.59		1
CuF^+	$Cu^{2+} + F^- \leftrightarrows CuF^+$	1.62	1.26		1
$CuOH^+$	$Cu^{2+} + H_2O \leftrightarrows CuOH^+ + H^+$	0	-8		1
$Cu(OH)_2^\circ$	$Cu^{2+} + 2H_2O \leftrightarrows Cu(OH)_2^\circ + 2H^+$	0	-13.68		1
$Cu(OH)_3^-$	$Cu^{2+} + 3H_2O \leftrightarrows Cu(OH)_3^- + 3H^+$	0	-26.899		1
$Cu(OH)_4^{2-}$	$Cu^{2+} + 4H_2O \leftrightarrows Cu(OH)_4^{2-} + 4H^+$	0	-39.6		1
$Cu_2(OH)_2^{2+}$	$2Cu^{2+} + 2H_2O \leftrightarrows Cu_2(OH)_2^{2+} + 2H^+$	17.539	-10.359	*Log K$_{Cu2(OH)2 +2}$ = 2.497 - 3833/T*	1
$CuSO_4^\circ$	$Cu^{2+} + SO_4^{2-} \leftrightarrows CuSO_4^\circ$	1.22	2.31		1
$CuHCO_3^+$	$Cu^{2+} + H^+ + CO_3^{2-} \leftrightarrows CuHCO_3^+$	0	13		1
$ZnCl^+$	$Zn^{2+} + Cl^- \leftrightarrows ZnCl^+$	7.79	0.43		1
$ZnCl_2^\circ$	$Zn^{2+} + 2Cl^- \leftrightarrows ZnCl_2^\circ$	8.5	0.45		1
$ZnCl_3^-$	$Zn^{2+} + 3Cl^- \leftrightarrows ZnCl_3^-$	9.56	0.5		1
$ZnCl_4^{2-}$	$Zn^{2+} + 4Cl^- \leftrightarrows ZnCl_4^{2-}$	10.96	0.199		1
ZnF^+	$Zn^{2+} + F^- \leftrightarrows ZnF^+$	2.22	1.15		1
$ZnOH^+$	$Zn^{2+} + H_2O \leftrightarrows ZnOH^+ + H^+$	13.399	-8.96		1
$Zn(OH)_2^\circ$	$Zn^{2+} + 2H_2O \leftrightarrows Zn(OH)_2^\circ + 2H^+$	0	-16.899		1
$Zn(OH)_3^-$	$Zn^{2+} + 3H_2O \leftrightarrows Zn(OH)_3^- + 3H^+$	0	-28.399		1
$Zn(OH)_4^{2-}$	$Zn^{2+} + 4H_2O \leftrightarrows Zn(OH)_4^{2-} + 4H^+$	0	-41.199		1
$ZnOHCl^\circ$	$Zn^{2+} + H_2O + Cl^- \leftrightarrows ZnOHCl^\circ + H^+$	0	-7.48		1
$ZnSO_4^\circ$	$Zn^{2+} + SO_4^{2-} \leftrightarrows ZnSO_4^\circ$	1.36	2.37		1
$Zn(SO_4)_2^{2-}$	$Zn^{2+} + 2SO_4^{2-} \leftrightarrows Zn(SO_4)_2^{2-}$	0	3.28		1
$ZnHCO_3^+$	$Zn^{2+} + H^+ + CO_3^{2-} \leftrightarrows ZnHCO_3^+$	0	12.4		1
$ZnCO_3^\circ$	$Zn^{2+} + CO_3^{2-} \leftrightarrows ZnCO_3^\circ$	0	5.3		1
$Zn(CO_3)_2^{2-}$	$Zn^{2+} + 2CO_3^{2-} \leftrightarrows Zn(CO_3)_2^{2-}$	0	9.63		1
HCO_3^-	$H^+ + CO_3^{2-} \leftrightarrows HCO_3^-$	-3.561	10.329	*Log K$_{HCO3-}$ = -6.498 + 0.02379T + 2902.39/T*	1
$H_2CO_3^\circ$	$2H^+ + CO_3^{2-} \leftrightarrows H_2CO_3^\circ$	-5.738	16.681		1
HSO_4^-	$H^+ + SO_4^{2-} \leftrightarrows HSO_4^-$	4.91	1.987	*Log K$_{HSO4-}$ = -5.3505 + 0.0183412T + 557.2461/T*	1
HF°	$H^+ + F^- \leftrightarrows HF^\circ$	3.18	3.18		1
HF_2^-	$H^+ + 2F^- \leftrightarrows HF_2^-$	4.55	3.749		1
$H_2F_2^\circ$	$2H^+ + 2F^- \leftrightarrows H_2F_2^\circ$	0	6.768		1

Figure 26. Measured dissolved iron(II)-to-iron(total) ratios compared with ratios used in the OTEQ simulations for the upper section of the low-flow (August 2001) simulations.

Figure 27. Measured dissolved iron(II)-to-iron(total) ratios compared with ratios used in the OTEQ simulations for the middle section of the low-flow (August 2001) simulations.
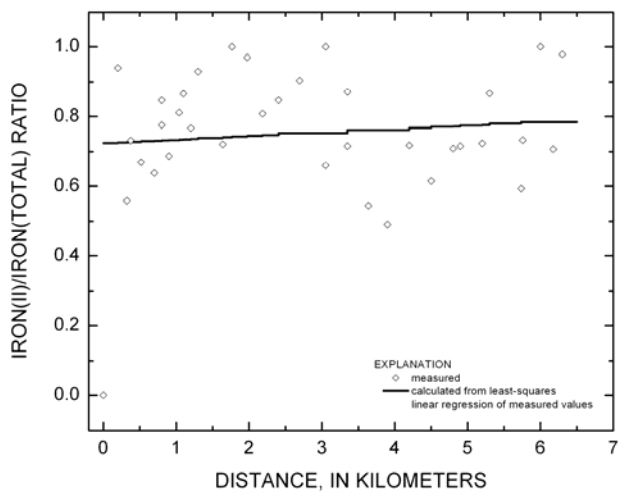
Figure 28. Measured dissolved iron(II)-to-iron(total) ratios compared with ratios used in the OTEQ simulations for the lower section of the low-flow (August 2001) simulations.
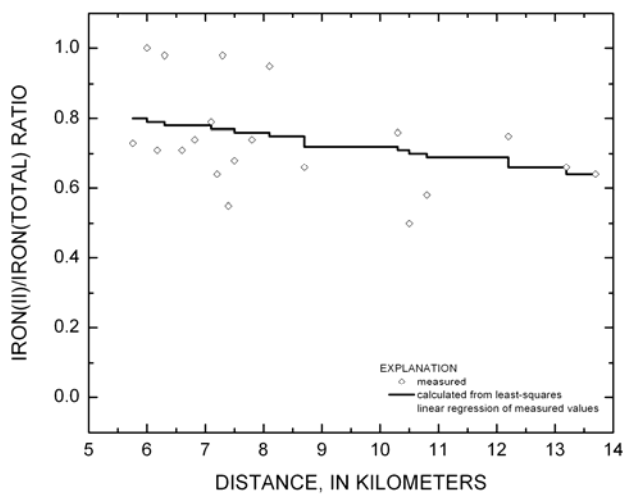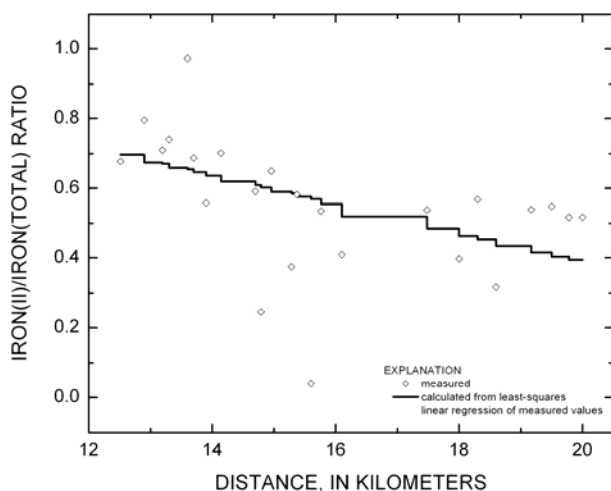
Simulation Results

Simulation results for pH (graph A), aluminum (graph B), iron (graph C), copper (graph D), and zinc (graph E) as a function of distance are shown in figures 29 to 31 for the three stream sections of the August 2001 tracer-injection/synoptic study, and in figures 35 to 37 for the three stream sections of the March/April 2002 tracer-injection/synoptic study. Figures 32 to 34 and 38 to 40 illustrate the conservative simulation of fluoride (graph A), manganese (graph B), magnesium (graph C), calcium (graph D), and sulfate (graph E) for the three stream sections of the two studies. Data are not shown for sodium, chloride, and carbonate. Figures 32 to 34 and 38 to 40 illustrate the typical accuracy with which measured data for the conservative components were reproduced by the simulations.

OTEQ simulations reproduced the general behavior of all components in the three stream sections of the study area, for both the August 2001 and the March/April 2002 tracer injection-synoptic studies. The fit to measured data supports the adequacy of the steady-state assumption. Simulation results indicate that aluminum, copper, hydrogen, iron (II and III), and zinc were reactive along the modeled sections, and that other solutes, including calcium, chloride, fluoride, magnesium, manganese, sodium, and sulfate were non-reactive. Iron, aluminum, copper, and zinc simulation results demonstrate that the reactive behavior of these solutes can be simulated with good precision (figs. 29 to 31 and 35 to 37), considering the occurrence of these components at concentrations close to method detection limits for many constituents. For example, for all six simulations, total-recoverable copper concentrations never exceeded 0.5 micromoles per liter and total-recoverable zinc concentrations never exceeded 3 micromoles per liter, yet the reactive transport model was able to simulate their concentrations within 0.1 to 0.3 micromoles per liter in the main stem of the Red River based solely on measured concentrations at the upstream boundary and in the inflowing tributaries, and chemical interactions in the Red River. The iron, copper, and zinc results (figs. 29 to 31 and 35 to 37) demonstrate that sorption to the amount of iron hydroxide precipitate actively forming in the water column quantitatively represents the measured copper and zinc concentrations. The foregoing represents a significant simulation result, because the mass of sorbent in the water column frequently is considered an adjustable reactive-transport modeling parameter.

48

Figure 29. Low-flow (August 2001) OTEQ simulations of (A) pH and (B) aluminum, (C) iron, (D) copper, and (E) zinc concentrations for the upper section.

Figure 30. Low-flow (August 2001) OTEQ simulations of (A) pH and (B) aluminum, (C) iron, (D) copper, and (E) zinc concentrations for the middle section.
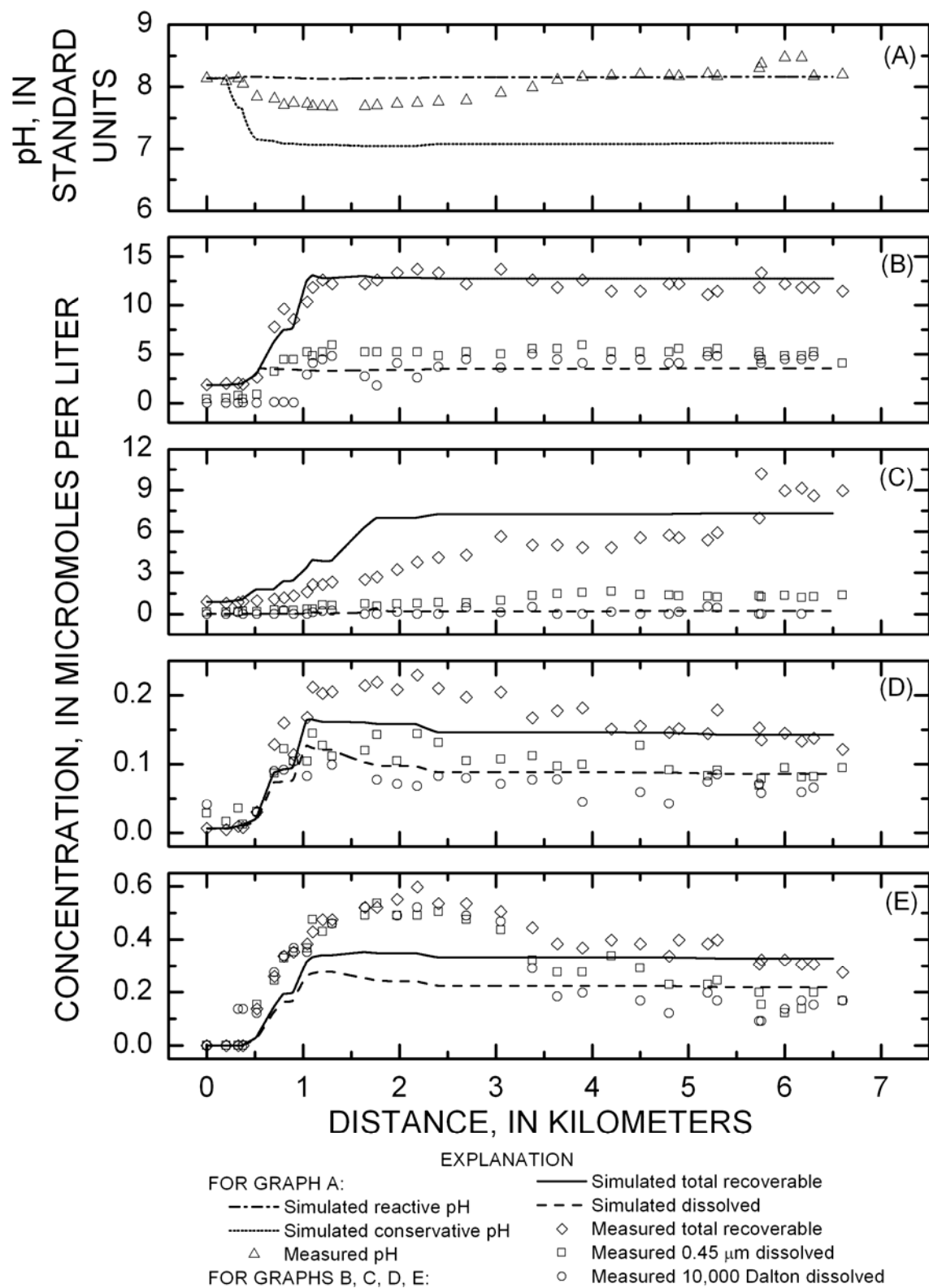
Figure 31. Low-flow (August 2001) OTEQ simulations of (A) pH and (B) aluminum, (C) iron, (D) copper, and (E) zinc concentrations for the lower section.

Figure 32. Low-flow (August 2001) conservative simulations of dissolved (A) fluoride, (B) manganese, (C) magnesium, (D) calcium, and (E) sulfate, for the upper section.

Figure 33. Low-flow (August 2001) conservative simulations of dissolved (A) fluoride, (B) manganese, (C) magnesium, (D) calcium, and (E) sulfate, for the middle section.

Figure 34. Low-flow (August 2001) conservative simulations of dissolved (A) fluoride, (B) manganese, (C) magnesium, (D) calcium, and (E) sulfate, for the lower section.
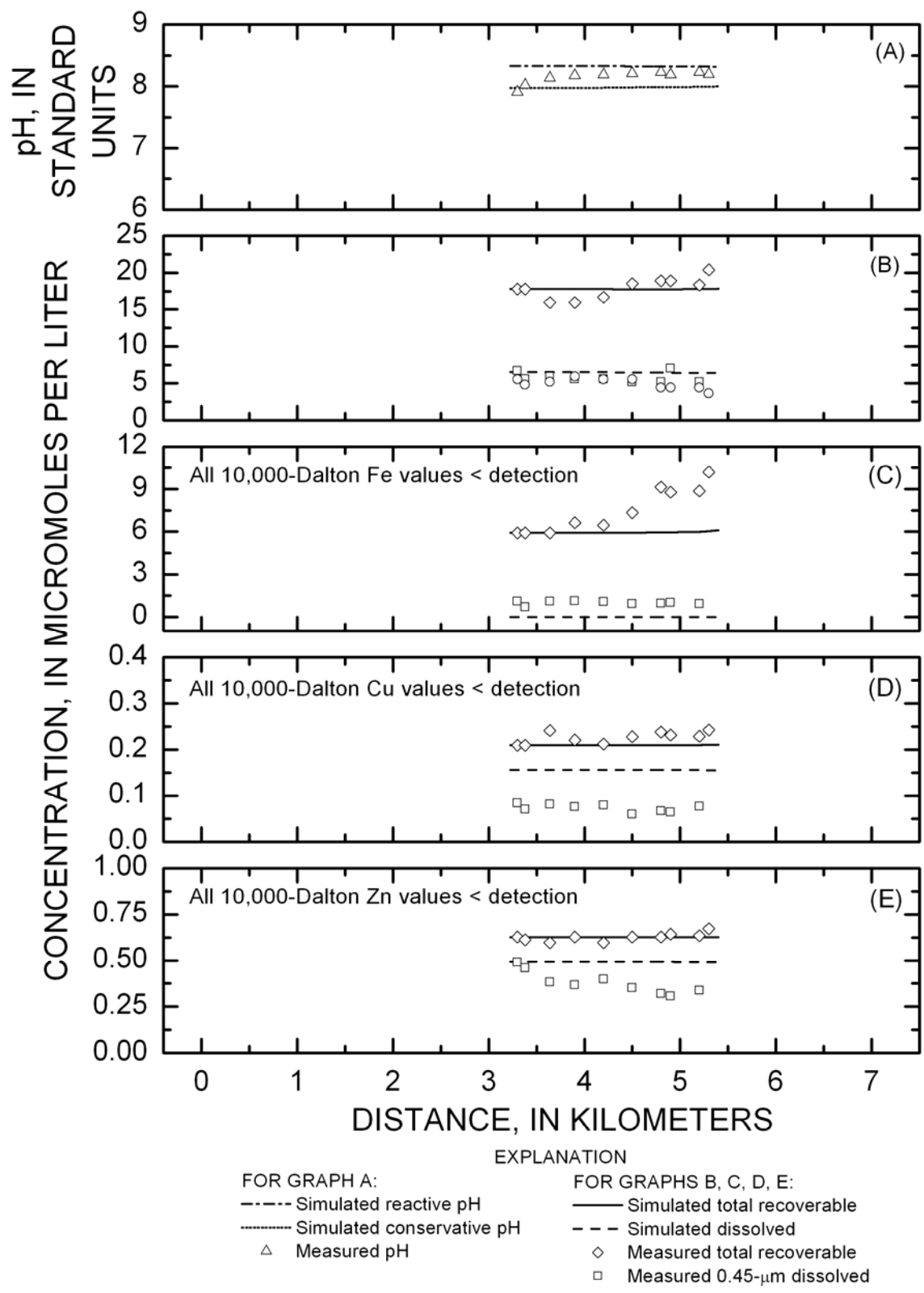
Figure 35. March/April 2002 OTEQ simulations of (A) pH and (B) aluminum, (C) iron, (D) copper, and (E) zinc concentrations for the upper section.
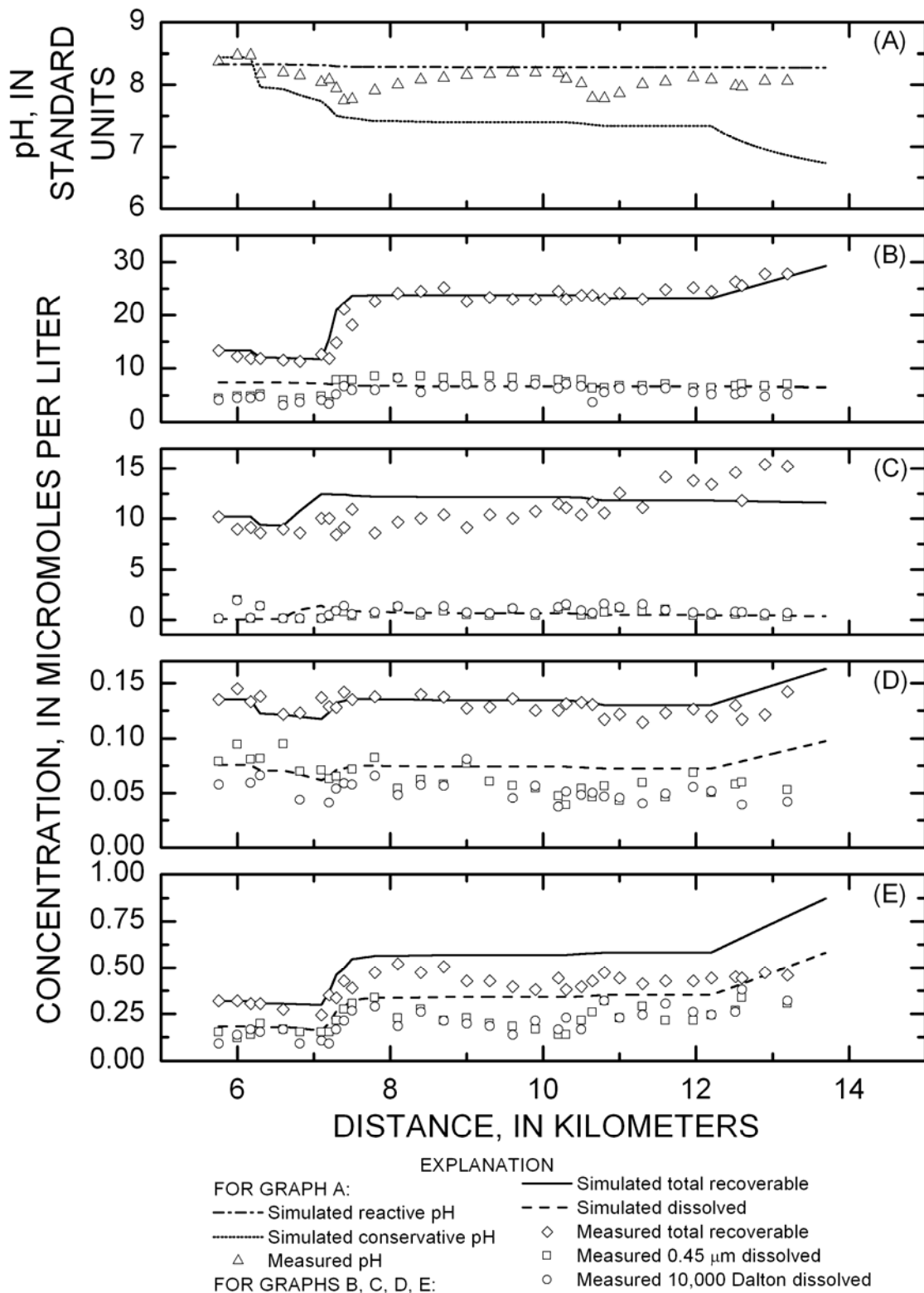
55
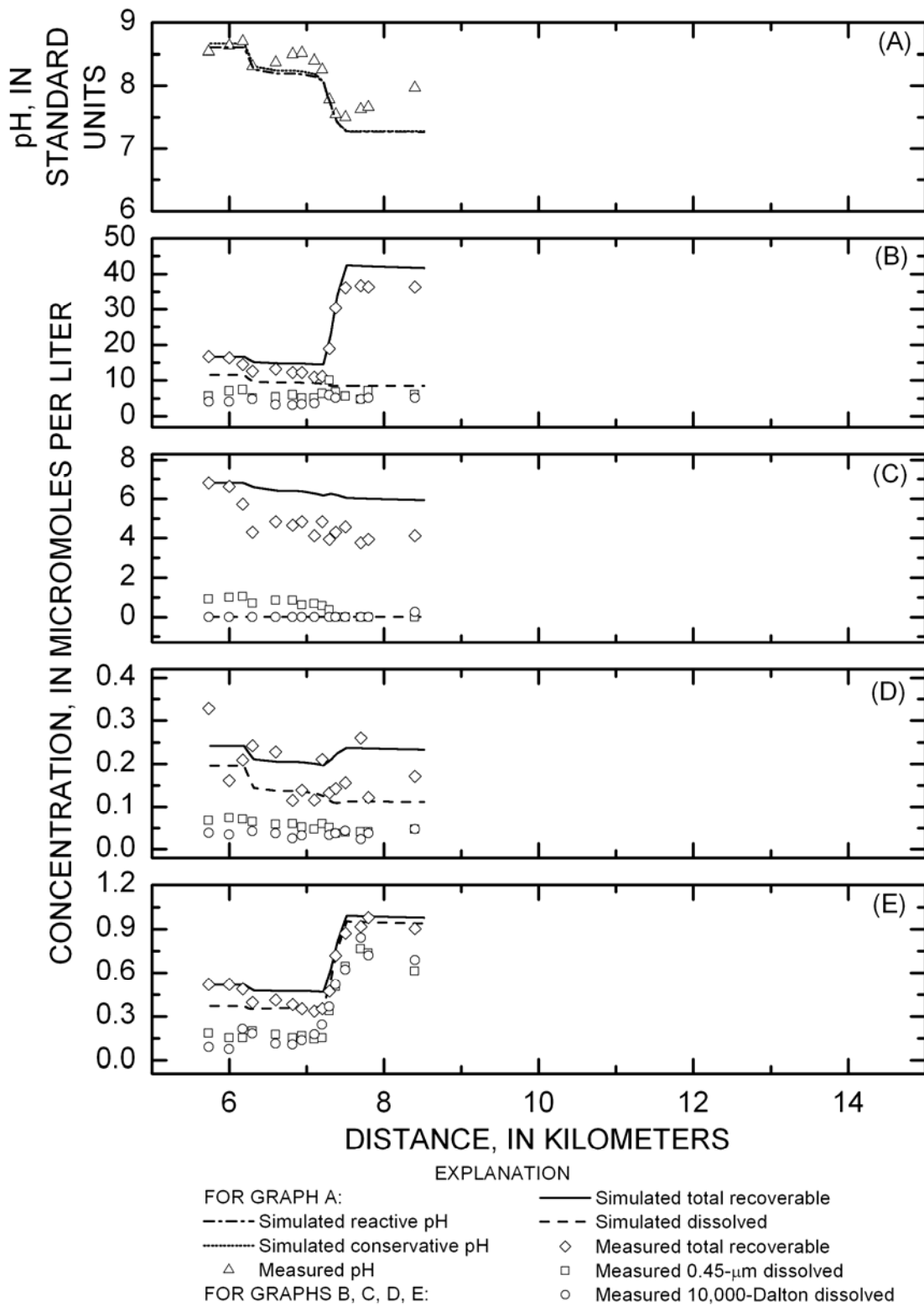
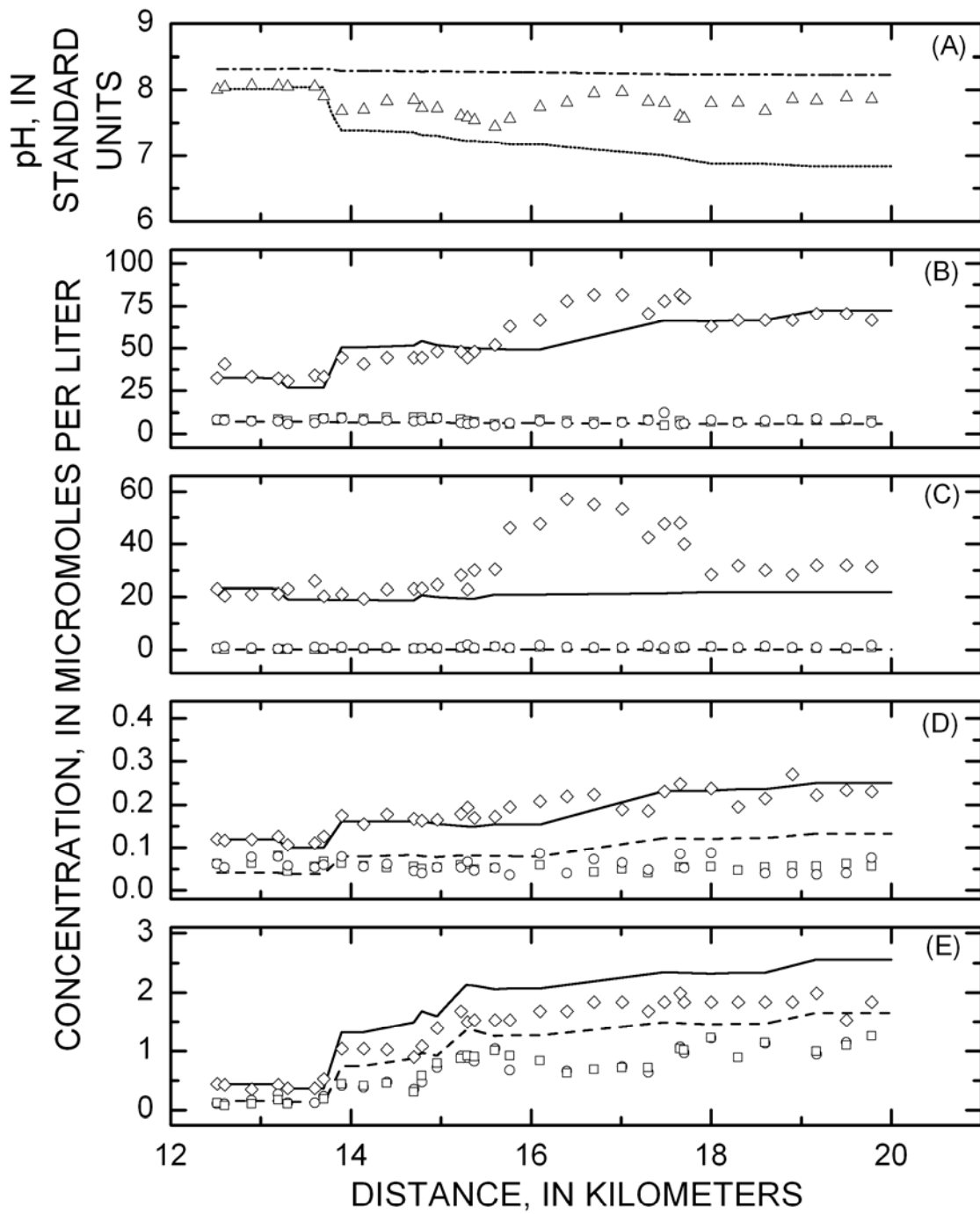**Figure 36**. March/April 2002 OTEQ simulations of (A) pH and (B) aluminum, (C) iron, (D) copper, and (E) zinc concentrations for the middle section.
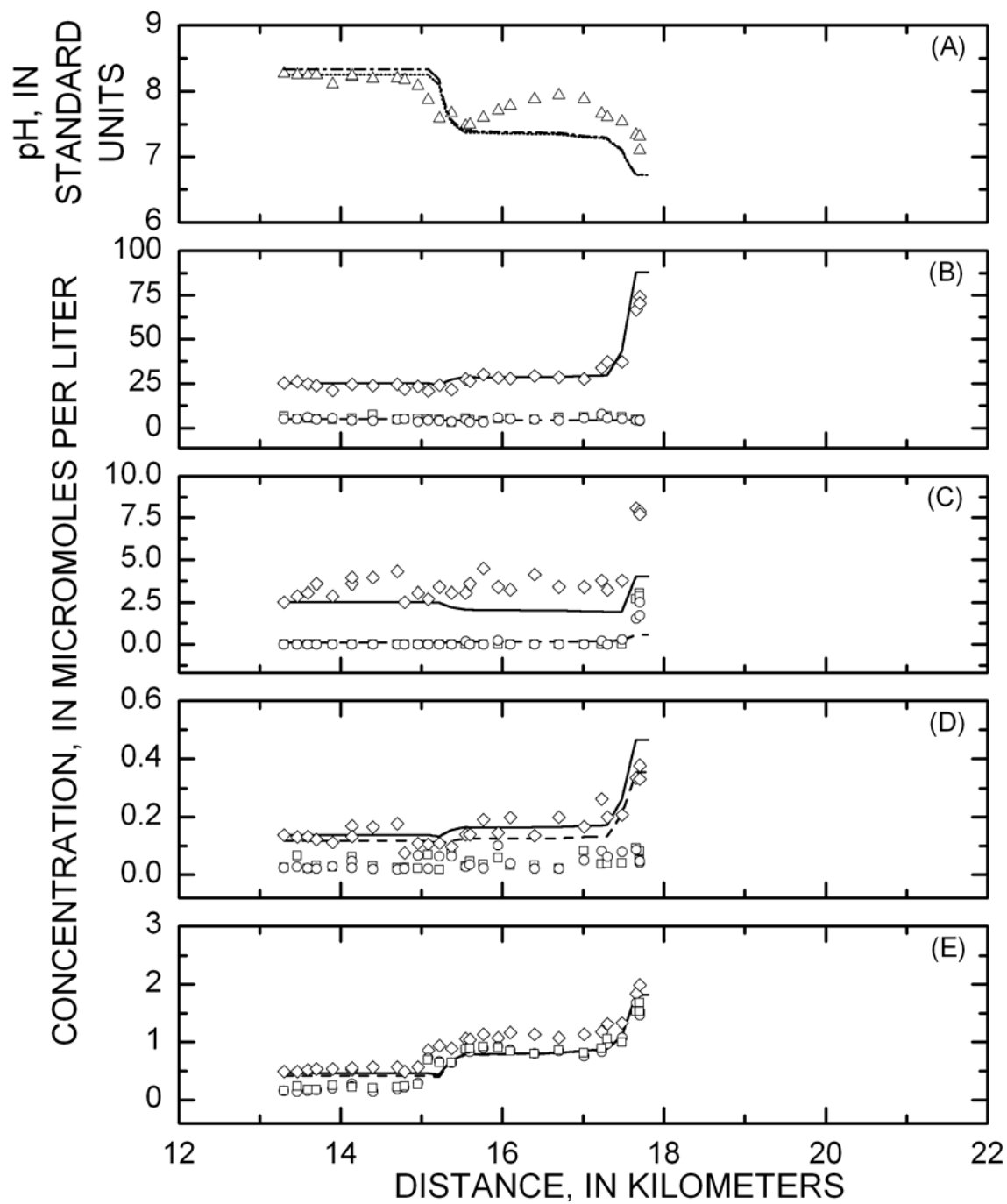
Figure 37. March/April 2002 OTEQ simulations of (A) pH and (B) aluminum, (C) iron, (D) copper, and (E) zinc concentrations for the lower section.
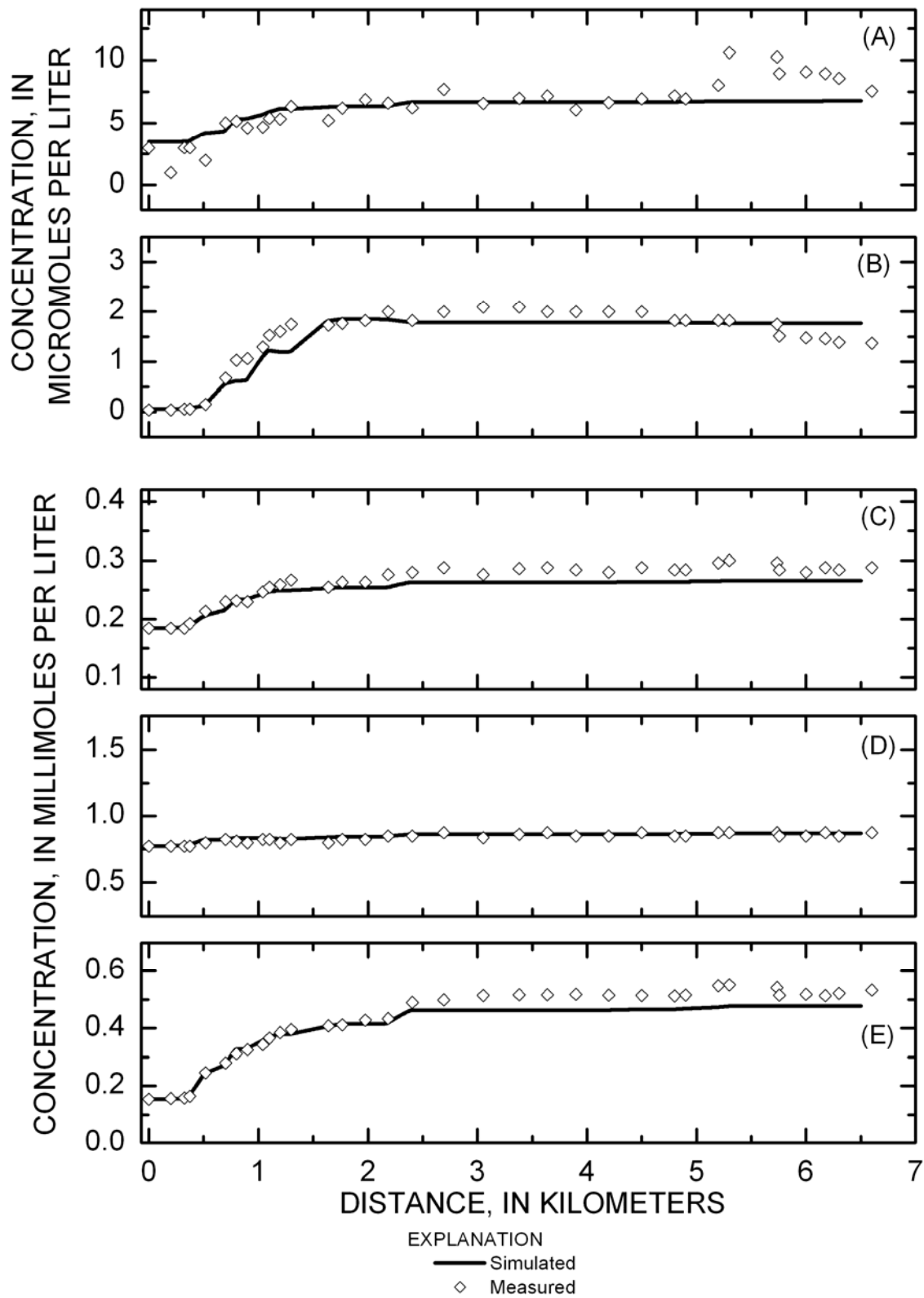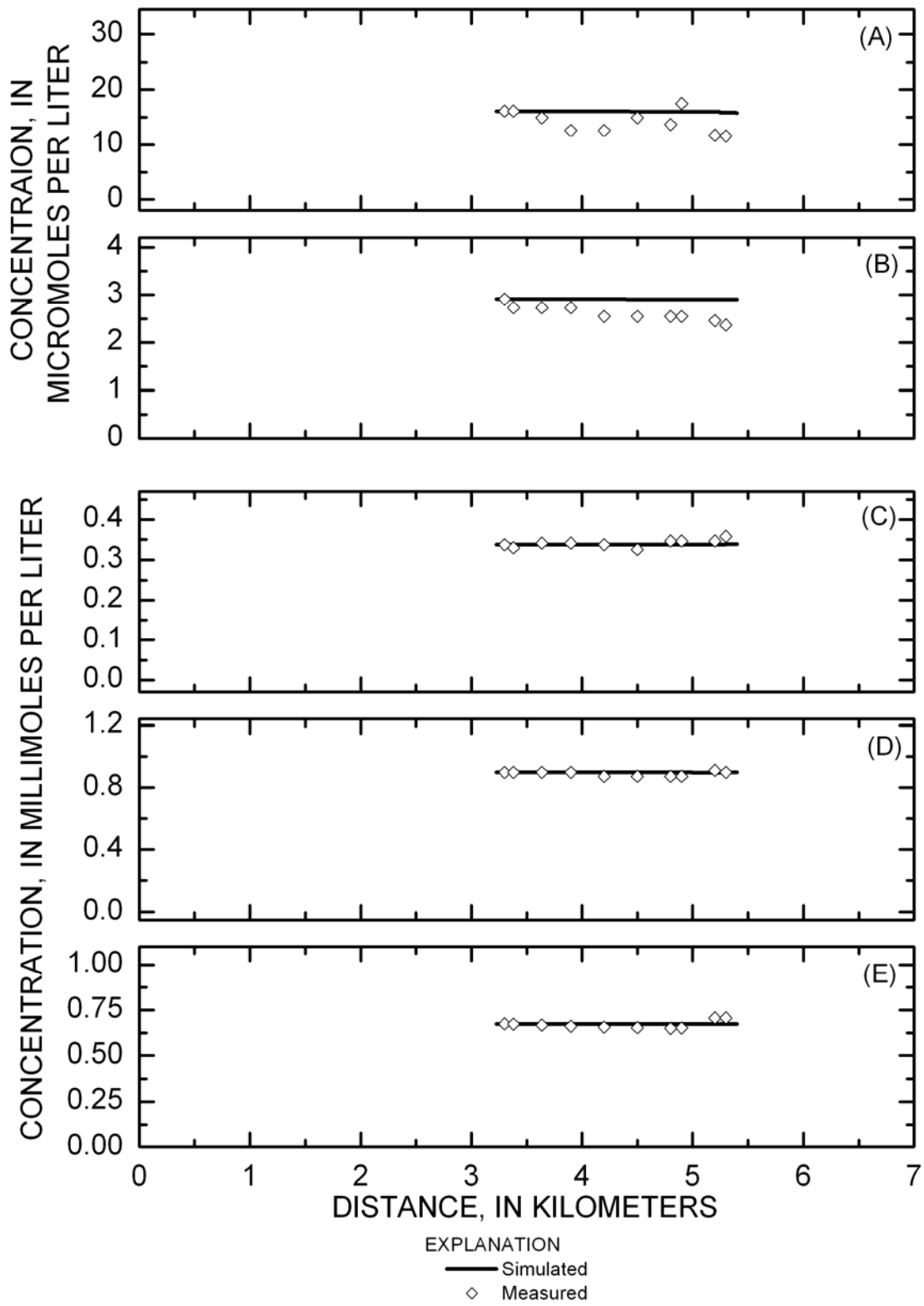
Figure 38. March/April 2002 conservative simulations of dissolved (A) fluoride, (B) manganese, (C) magnesium, (D) calcium, and (E) sulfate, for the upper section.
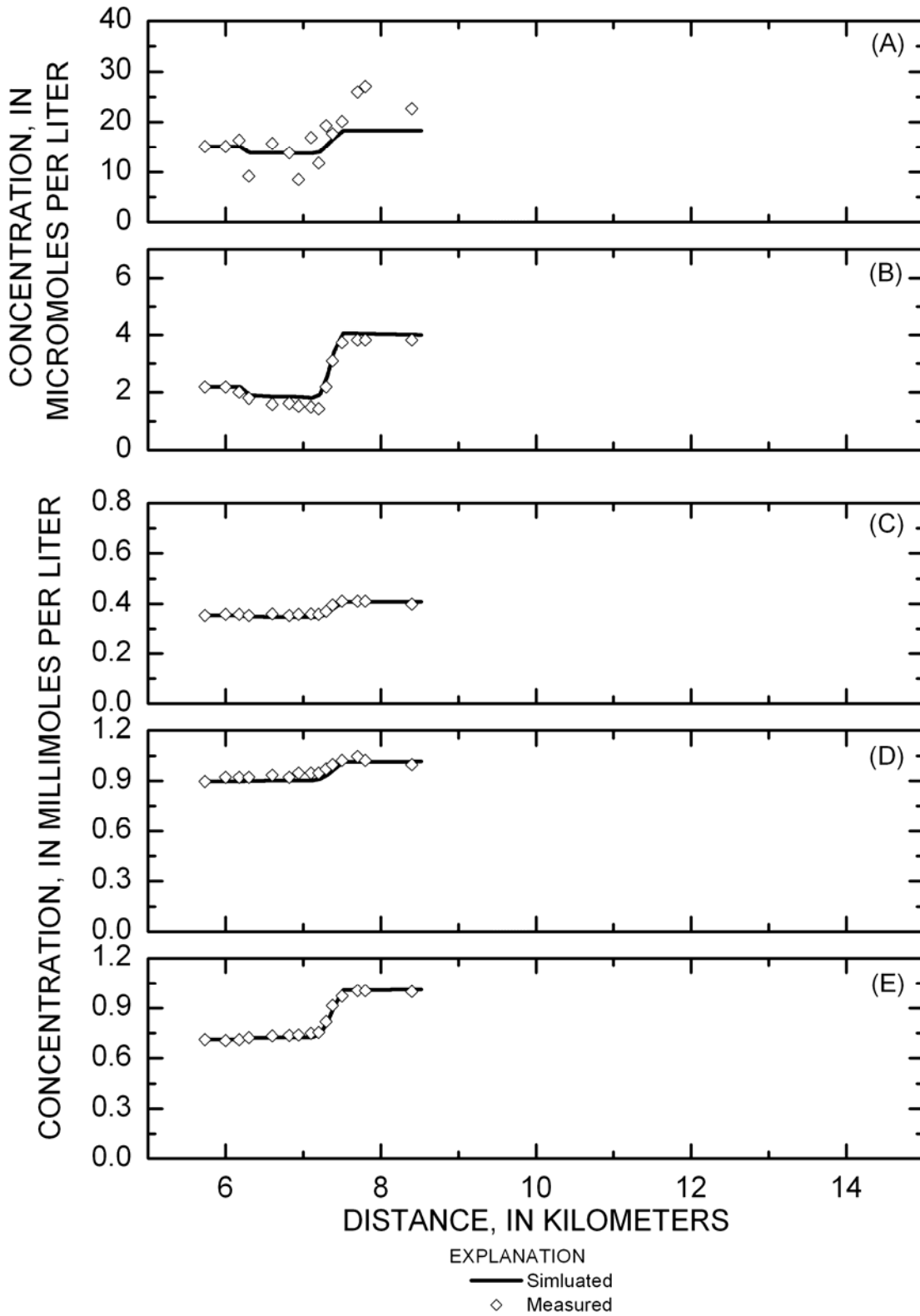
Figure 39. March/April 2002 conservative simulations of dissolved (A) fluoride, (B) manganese, (C) magnesium, (D) calcium, and (E) sulfate, for the middle section.
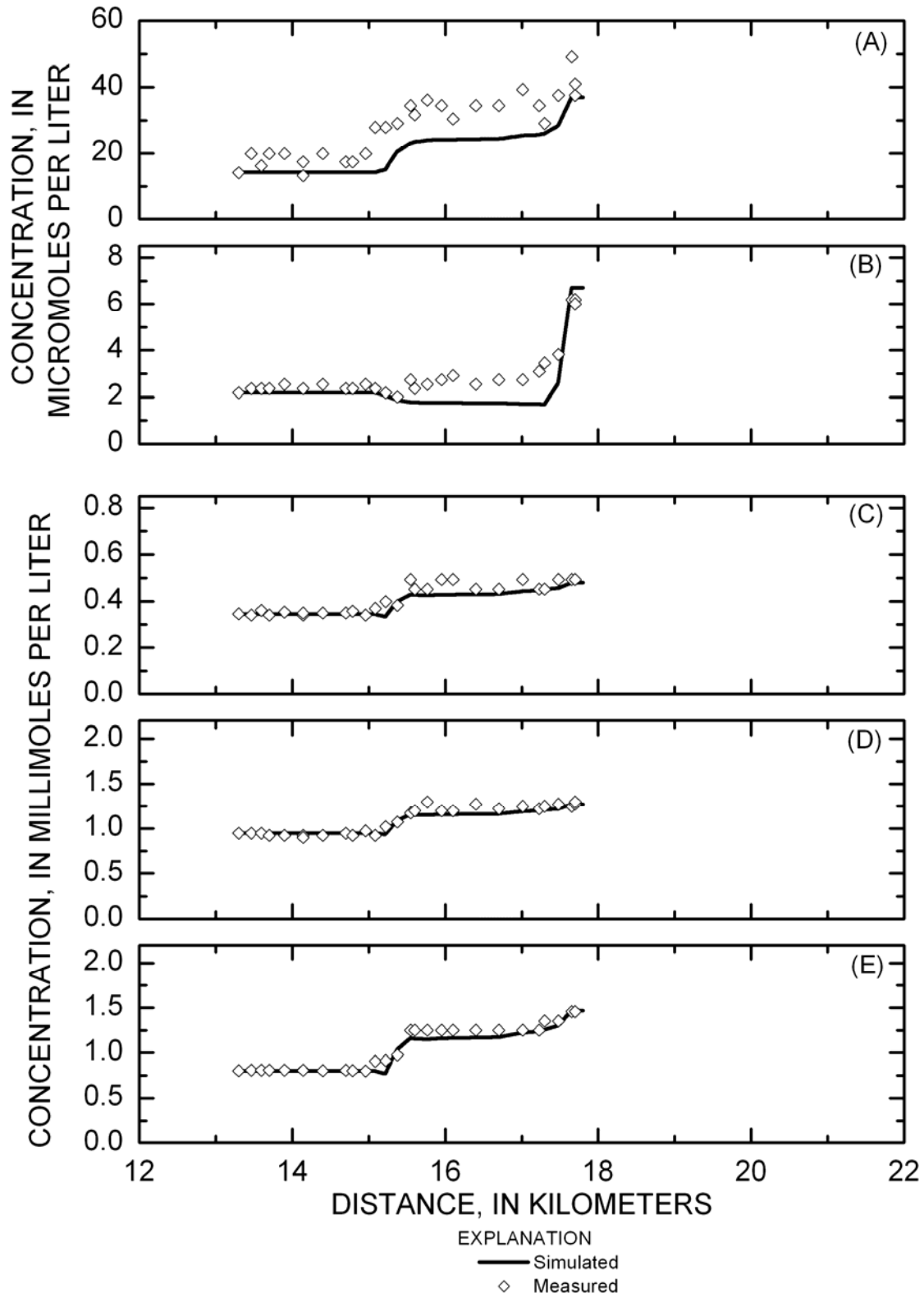
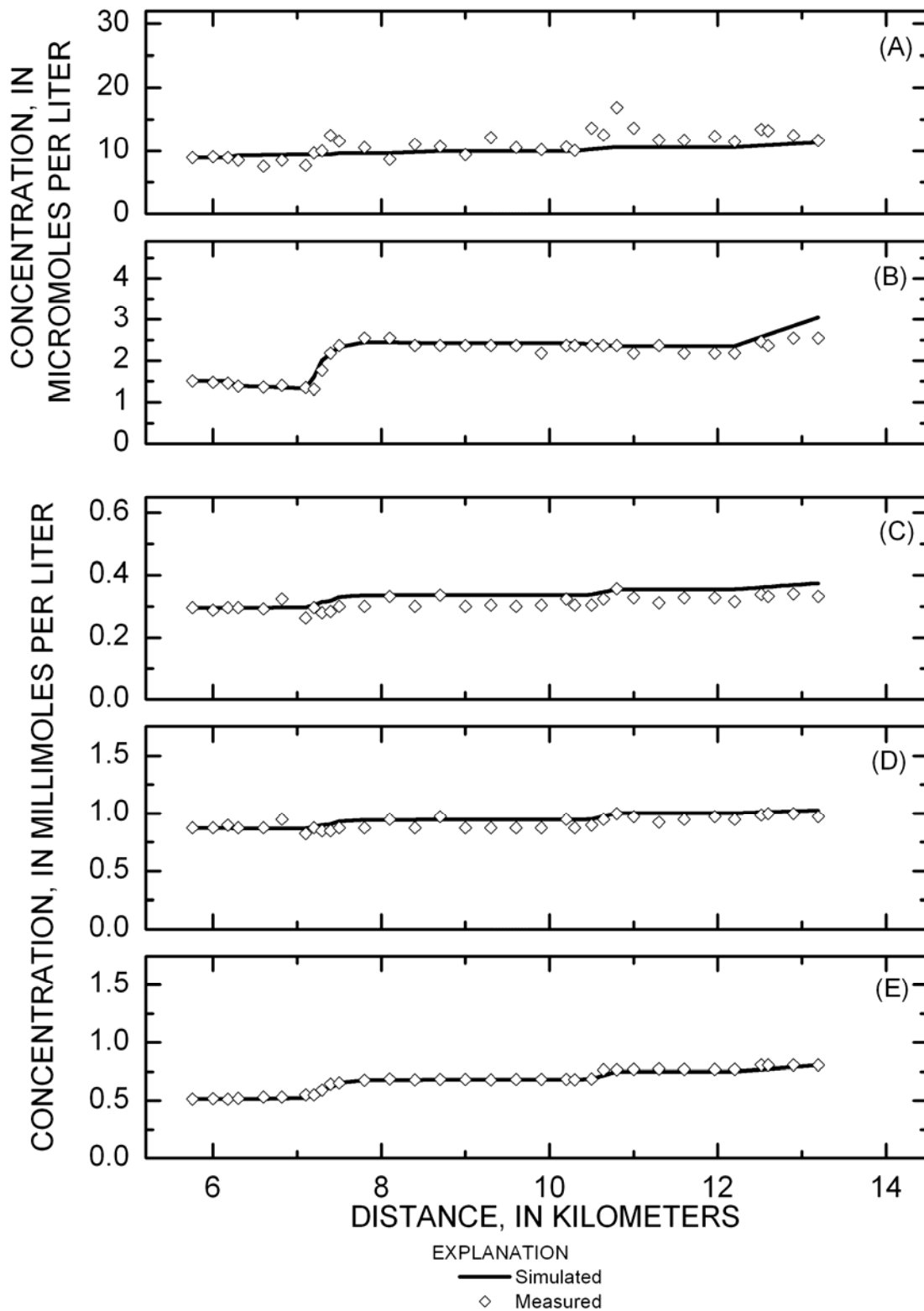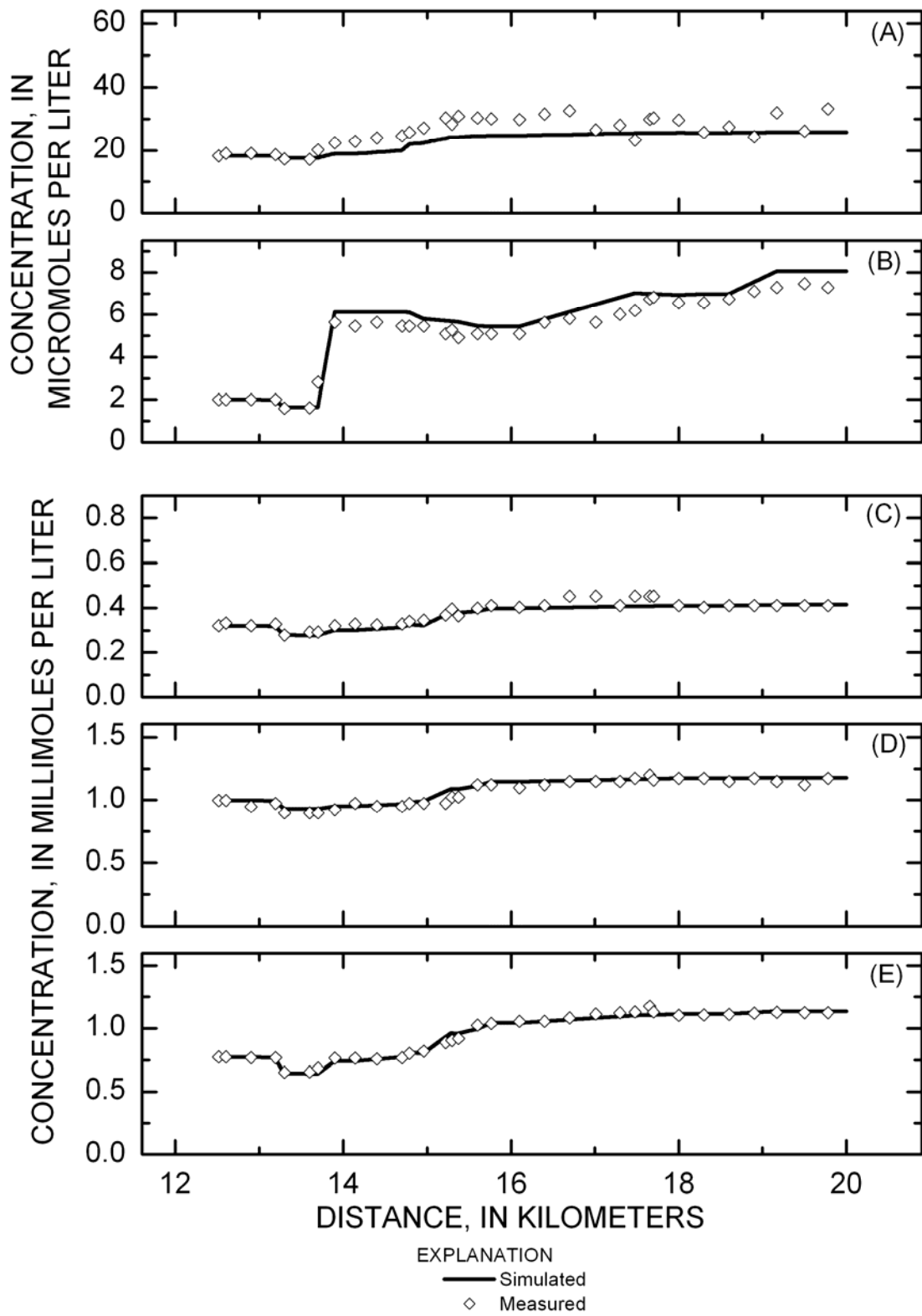**Figure 40**. March/April 2002 conservative simulations of dissolved (A) fluoride, (B) manganese, (C) magnesium, (D) calcium, and (E) sulfate, for the lower section.

Hydrogen

Results of the simulations of pH, together with measured pH values, are shown on figures 29A, 30A, 31A, 35A, 36A, and 37A. Acidification and neutralization cycles were observed in measured pH values throughout the entire study reach (see also fig. 20). These cycles are the result of slow degassing of carbon dioxide that is the product of neutralization of acidity by alkalinity. The six most obvious locations of low pH occur from 0.8 to 2.0 km and at 7.5, 10.8, 13.9, 15.6, and 17.7 km. These six locations coincide with those where mass-loading calculations identified inflows containing considerable loads of acidity, sulfate, and metals. Thus, the identified inflow loads also may be implicated as sources of acidification of the Red River.

The repeated cycles of acidification and neutralization observed in the measured pH data for the Red River could not be reproduced by the reactive pH simulations, with or without equilibrium with atmospheric carbon dioxide (figs. 29A, 30A, 31A, 35A, 36A, and 37A). As a consequence, the accuracy with which phase transfer reactions such as precipitation, sorption, and degassing can be simulated is limited by the equilibrium assumption implicit in the reactive-transport model. Dynamic open-system processes such as transfer of gases (including carbon dioxide) between an aqueous phase and the atmosphere are strongly influenced by kinetic factors. As such, they are difficult to simulate using an equilibrium thermodynamic model such as that implemented in the MINTEQA2 computer code, because for reactions that are sufficiently slow the instantaneous equilibrium assumption implicit in the model is not valid.

Adjusting reactive-transport-modeling parameters allowed simulation of the upper and lower boundary conditions of pH, one with no equilibration, and the other with instantaneous equilibration, with atmospheric carbon dioxide. Consequently, the reactive-transport simulations allowed only approximate reproduction of the measured pH values for the Red River. Simulated pH differed from measured pH as much as -0.6 pH unit for the middle section of the March/April 2002 simulations (fig. 36A) and +0.9 pH unit for the lower section of the August 2001 simulations

(fig. 31A). The effect of these discrepancies is difficult to quantify. Simulation of pH values less than those measured would tend to concurrently reduce formation of HFO and sorption of copper and zinc, whereas simulation of greater pH values would have the opposite effect.

Aluminum

Results of the simulated and measured aluminum concentrations are shown on figures 29B, 30B, 31B, 35B, 36B, and 37B. Dissolved aluminum concentrations in the Red River main stem ranged from about 0.01 to 0.3 mg/L with the lower end of this range about 10 times the method detection limit of 0.001 mg/L. Mixing zones with actively forming white precipitates were observed in the Red River at the time of sampling, and total-recoverable aluminum concentrations were substantially greater than dissolved aluminum concentrations in most of the Red River between the town of Red River and the Ranger Station. Numerous seeps, springs, and surface and ground waters, many of which are acidic and contain high concentrations of aluminum, enter the Red River along the study reach. Neutralization along the mixing zones of the acidic inflows and Red River water is followed by precipitation of amorphous to poorly crystalline aluminum oxyhydroxides. This precipitation causes dissolved aluminum concentrations in the Red River to decrease until they reach approximately 0.16 mg/L, whereupon they appear to be stabilized by complexing with dissolved organic carbon. The hypothesis of aluminum-organic complexing could not be investigated further because organic materials potentially responsible for complexing aluminum were not identified or quantified, and no reliable thermodynamic data were available for calculating distributions of species that included aluminum-organic complexes. The range of pH over which simulated pH values did not match measured pH values is not in the range where aluminum aqueous speciation, precipitation, or dissolution are sensitive to pH.

Iron

The simulated and measured iron concentrations are shown on figures 29C, 30C, 31C, 35C, 36C, and 37C. Dissolved iron

concentrations in the Red River main stem were low and analytical values were likely overestimated in some cases (McCleskey and others, 2004). Total-recoverable iron concentrations were substantially higher than dissolved iron concentrations and formed the basis for simulating the formation of suspended HFO for sorption of copper and zinc. Sources of potential errors in determining total-recoverable metal concentrations included filtration timing and difficulties obtaining representative samples from shallow or low-discharge inflow sources (McCleskey and others, 2003; 2004). Nevertheless, iron concentrations in the suspended solid phase were acceptably consistent and allowed acceptable sorption modeling results to be obtained for copper and zinc. Although it is not expected to affect formation of HFO, the pH range over which simulated pH matches measured data poorly is a range where copper and zinc sorption to HFO are sensitive to the solution pH. However, most pH simulation errors tend to be toward higher pH which would result in simulation of increased sorption and thus simulated dissolved copper and zinc concentrations that were lower than measured values. This consequence is not seen in the results.

In the lower sections of the study area, the reactive-transport model underestimated total-recoverable iron concentrations and over-estimated total-recoverable copper and zinc concentrations (figs. 31C, 31D, 31E). A possible explanation for these results is inflow concentrations for total-recoverable iron that are too low. Many of the inflow sources that were used as input to the simulations were seeps and springs that had little visible surface flow. Thus, obtaining a representative sample of suspended material for determination of total-recoverable concentrations appears problematic at best and impossible at worst. While a more representative total-recoverable iron sample also may have contained higher concentrations of total-recoverable copper and zinc, this would not necessarily be so. The sorption characteristics of the HFO also may change as fresh precipitate ages; however, there was no way to measure the sorption characteristics of such small quantities of precipitate even had they been collected. Furthermore, the OTEQ computer code cannot accommodate sorption characteristics that vary as

a function of distance. Thus, unfortunately, these hypotheses could not be tested.

Copper

Measured total-recoverable copper concentrations in the Red River never exceeded 0.5 micromoles per liter. Measured dissolved copper concentrations were considerably lower, occasionally less than 0.01 micromoles per liter. Many copper concentrations were below the method detection limit of even the most sensitive analytical methods (inductively-coupled plasma-mass spectrometry and graphite-furnace atomic-absorption spectrometry) used in this study.

Sorption accounts for divergence of the lines for simulated dissolved copper from those for simulated total-recoverable copper (figs. 29D, 30D, 31D, 35D, 36D, and 37D). Simulation of copper sorption to HFO actively forming in the water column accurately reproduced the measured copper concentrations in the Red River, notwithstanding the consistently low copper concentrations.

Zinc

Zinc sorption is indicated by differences between the simulated total-recoverable and dissolved zinc concentrations (figs. 29E, 30E, 31E, 35E, 36E, and 37E). The highest total-recoverable and dissolved zinc concentrations in the Red River main stem were about 0.5 and 0.4 micromoles per liter, respectively. Despite the use of careful sample processing procedures, contamination of many samples with zinc from the filtration apparatus could not be avoided. Consequently, many elevated dissolved zinc concentrations deemed outliers were not included in the plots presented here. Although their inclusion would have given the appearance of improved correspondence between measured and simulated concentrations, the scatter in the data would have obscured the relation as a function of downstream distance. Although not known with certainty, the elevated zinc concentrations were most likely the ones in error. The OTEQ simulations would appear substantially more accurate if the elevated zinc concentrations were the correct values.

Another source of inconsistency between measured and simulated dissolved zinc concentrations may be the sorption parameters used in the OTEQ computer code. The potential for sorption was maximized by setting the high-affinity site density of the HFO sorbent to the top of its allowable range, and by setting the precipitate settling velocity to zero, effectively maintaining all the HFO precipitate in the water column. If zinc sorption still is not sufficient, the specific sorption parameters for zinc may be in error or may be inappropriate for the system being modeled. In addition, manganese is known to be precipitating from the Red River in the lower sections of the study area. Sorption of zinc by manganese oxyhydroxides has been shown to occur (Fuller and Harvey, 2000) and may affect zinc concentrations to a greater extent than sorption to HFO. This reaction was not simulated for this study because the necessary sorption parameters were not available. Sorption by manganese oxyhydroxides also may be an issue for copper but may not be evident at the reduced concentrations at which copper occurs in the Red River.

SUMMARY

Mass-loading calculations for the Red River between the town of Red River and the USGS streamflow-gaging station at the National Forest Ranger Station near Questa, New Mexico allowed identification of six specific locations where elevated concentrations of potential contaminants enter the Red River. These locations, characterized by features on the north side of the Red River that are known to be sources of low-pH water containing elevated metal and sulfate concentrations, are: the initial 2.4 km of the study reach, including Bitter Creek, the stream section from 6.2 to 7.8 km, encompassing La Bobita well and the Hansen debris fan, Sulphur Gulch, at about 10.5 km, the area near Portal Springs, from 12.2 to 12.6 km, and the largest contributors of mass loading, the 13.7 to 13.9 and 14.7 to 17.5 km stream sections from Cabin Springs to Thunder Bridge, and Goathill Gulch to Capulin Canyon, respectively.

Mass ratios of several elements for surface-water inputs to the Red River were compared with those for nearby ground waters.

These comparisons led to the conclusion that inflows to the Red River in the La Bobita/Waldo Spring area originated from these ground waters and not from ground water upstream from this area. Calculation of mass ratios of several elements to sulfate and development of conservative mixing lines resulted in identification of alluvial ground waters in the vicinity of Straight Creek and the La Bobita/Waldo Spring area that appeared to lie on a flow path to the Red River. These ground waters included water from the Hansen, La Bobita, SC-8A, and MMW-17A wells.

Aqueous geochemical speciation modeling led to identification of an empirical equilibrium constant for the formation of aluminum hydroxide precipitate that was consistent with the aluminum concentrations measured in the Red River. This modeling also allowed a hypothesis to be advanced of possible complexing of aluminum by natural organic material that allows aluminum dissolved in the Red River to be maintained at concentrations greater than those predicted by saturation with a microcrystalline gibbsite phase.

Reactive-transport processes in the Red River were simulated using the OTEQ reactive-transport model. The simulations were calibrated using data from synoptic studies conducted in August 2001 and in March/April 2002. August 2001 simulations included iron(II) oxidation, constrained using measured dissolved concentrations of iron(II) and iron(total). Both simulations included precipitation of hydrous ferric oxide as $Fe(OH)_3$ and amorphous $Al(OH)_3$, and sorption of copper and zinc to freshly precipitated hydrous ferric oxide actively forming in the water column. Simulations revealed that hydrogen, iron, aluminum, copper, and zinc were non-conservative and that precipitation can account for iron and aluminum concentrations. Measured copper and zinc concentrations in the water column could be accounted for by simulating their sorption to the hydrous ferric oxide in the water column. Speciation and saturation index calculations indicated that $Al(OH)_3$ solubility limits the concentration of aluminum between pH 5.0 and 7.5. However, at pH values greater than 7 and aluminum concentrations less than 0.3 mg/L, inorganic speciation and aluminum-organic complexing may combine to allow somewhat elevated

concentrations of aluminum to remain in solution. Mineral solubility controls may not dominate the aluminum solution chemistry in this pH range.

Literature Cited

Achterberg, E.P., Braungardt, C., Morley, N.H., Elbaz-Paulichert, F., and LeBlanc, M., 1999, Impact of Los Frailes mine spill on riverine, estuarine, and coastal waters in southern Spain: Water Resources, v. 33, p. 3387-94.

Adams, F. and Rawajfih, A., 1977, Basaluminite and alunite: a possible cause of sulfate retention by acid soils: Soil Science Society of America Journal, v, 41, p. 686-692.

Allison, J.D., Brown, D.S., and Novo-Gradac., K.J., 1991, MINTEQA2/PRODEFA2, a geochemical assessment model for environmental systems: Version 3.0 user's manual: U.S. Environmental Protection Agency, EPA/600/3-91/021.

Appelo, C.A.J., and Postma, D., 1993, Geochemistry, Groundwater and Pollution: Amsterdam, Balkema.

Bahr, J.M., and Rubin, J., 1987, Direct comparison of kinetic and local equilibrium formulations for solute transport affected by surface reactions: Water Resources Research, v. 23, p. 438-452.

Ball, J.W., and Nordstrom, D.K., 1989, Final revised analyses of major and trace elements from acid mine waters in the Leviathan Mine drainage system, California and Nevada-October 1981 to October 1982: U.S. Geological Survey Water-Resources Investigations Report 89-4138, 46 p.

---, 1991, User's manual for WATEQ4F, with revised thermodynamic data base and test cases for calculating speciation of major, trace, and redox elements in natural waters: U.S. Geological Survey Open-File Report 91-183, 189 p.

Ball, J.W., Runkel, R.L., and Nordstrom, D.K., 1999, Transport modeling of reactive and non reactive constituents from Summitville, Colorado: Preliminary results from the application of the OTIS/OTEQ model to the Wightman Fork/Alamosa River system, In U.S. Geological Survey Toxic Substances Hydrology Program--Proceedings of the Technical Meeting, Charleston, South Carolina, March 8-12, 1999--Volume 1 of 3--Contamination from Hardrock Mining, Morganwalp, D.W., and Buxton, H.T., eds.: U.S. Geological Survey Water-Resources Investigations Report 99 4018A., p. 305 312.

---, 2004, Evaluating remedial alternatives for the Alamosa River and Wightman Fork, near the Summitville Mine, Colorado: Application of a reactive-transport model to low- and high-flow simulations, In Zannetti, P., Ed., Environmental Science and Environmental Computing, v. II: Fremont, CA, Envirocomp Institute, Chapter 3, 54 p.

Bencala, K.E., and Walters, R.A., 1983, Simulation of solute transport in a mountain pool-and-riffle stream: A transient storage model: Water Resources Research, v. 19, p.718-724.

Bigham, J.M., and Nordstrom, D.K., 2000, Iron and aluminum hydroxysulfates from acid sulfate waters, In Alpers, C.N., Jambor, J.L., and Nordstrom, D.K., eds., Sulfate minerals-Crystallography, geochemistry, and environmental significance: Washington, Mineralogical Society of America, Reviews in Mineralogy and Geochemistry, v. 40, p. 351-403.

Broshears, R.E., Runkel, R.L., Kimball, B.A., McKnight, D.M., and Bencala, K.E., 1996, Reactive solute transport in an acidic stream: Experimental pH increase and simulation of controls on pH, aluminum and iron: Environmental Science and Technology, v. 30, p. 3016-24.

Buchanan, T.J., and Somers, W.P., 1969, Discharge measurements at gaging stations: U.S. Geological Survey Techniques of Water-Resources Investigations, book 3, chapter A8, 65 p.

Caine, J.S., 2003, Questa baseline and pre-mining ground-water quality investigation. 6. Preliminary brittle structural geologic data, Questa mining district, southern Sangre de Cristo Mountains, New Mexico: U.S. Geological Survey Open-File Report 03-280, 7 p.

Davis, S.N., Whittemore, D.O., and Fabryka-Martin, J., 1998, Uses of chloride/bromide ratios in studies of potable water: Ground Water, v. 36, p. 338-350.

DiToro, D.M., 1976, Combining chemical equilibrium and phytoplankton models - A general methodology, *In* Canale, R.P., ed., Modeling Biochemical Processes in Aquatic Ecosystems: Ann Arbor, Michigan, Ann Arbor Science, p. 224-243.

Driscoll, C.T., Baker, J.P., Bisogni, J.J, and Schofield, C.L., 1984, Aluminum speciation and equilibria in dilute acidic surface waters of the Adirondack region of New York State, *In* Bricker, O.P., ed., Geological Aspects of Acid Deposition: Boston, Ann Arbor Science, Butterworths, p. 55-75.

Driscoll, C.T., and Postek, K.M., 1996, The chemistry of aluminum in surface waters, *In* Sposito, G., ed., The Environmental Chemistry of Aluminum, 2nd Edition: Boca Raton, CRC Press, p. 363-418.

Dzombak, D.A., and Morel., F.M.M., 1991, Surface Complexation Modeling: Hydrous Ferric Oxide: New York, John Wiley and Sons, 393 P.

Fitts, D.D., 1962, Nonequilibrium Thermodynamics: New York, McGraw-Hill, 173 p.

Fuller, C.C., and Harvey, J.W., 2000, Reactive uptake of trace metals in the hyporheic zone of a mining-contaminated stream, Pinal Creek, Arizona. Environmental Science and Technology, v. 34, p. 1150-1156.

Gale, V.G., and Thompson, A.J.B., 2001, Reconnaissance study of waste rock mineralogy: Questa, New Mexico, Petrography, PIMA spectral Analysis and Rietveld Analysis: PetraScience Consultants Inc., January 31.

Hanley, H.J.M., 1967, Transport Phenomena in Fluids: New York, Marcel-Dekker, 509 p.

Hendershot, W.H., Courchesne, F., and Jeffreid, D.S., 1996, Aluminum chemistry at the catchment scale in watersheds influenced by acidic precipitation, *In* Sposito, G., ed., The Environmental Chemistry of Aluminum, 2nd Edition: Boca Raton, CRC Press, p. 419-449.

Herczeg, A.L., and Edmunds, W.M., 2000, Inorganic ions as tracers, *In* Cook, P., and Herczeg, A.L., eds., Environmental Tracers in Subsurface Hydrology: Kluwer Academic Publishers, Chap. 2, p. 31-77.

Kilpatrick, F.A., and Cobb, E.D., 1985, Measurement of discharge using tracers: Techniques of Water-Resources Investigations of the U.S. Geological Survey, book 3, chapter A16, p. 52.

Kimball, B.A., Broshears, R.E., Bencala, K.E., and McKnight, D.M., 1994, Coupling of hydrologic transport and chemical reactions in a stream affected by acid mine drainage: Environmental Science and Technology, v. 28, p. 2065-2073.

Kimball, B.A., Callender, E., and Axtmann, E.V., 1995, Effects of colloids on metal transport in a river receiving acid mine drainage, upper Arkansas River, Colorado, USA: Applied Geochemistry, v. 10, p. 285-306.

Knight, P.J., 1990, The flora of the Sangre de Cristo Mountains, New Mexico, *In* Bauer, P.W., Lucas, S.G., Mawer, C.K., and McIntosh, W.C., eds., Tectonic development of the Southern Sangre de Cristo Mountains, New Mexico: New Mexico Geological Society, 41st field conference, Sept. 12-15, 1990, p. 94-95.

Korzhinskii, D.S., 1959, Physicochemical Basis of the Analysis of the Paragenesis of Minerals: New York, Consultants Bureau, 142 p.

Lipman, P.W., 1981, Volcano-tectonic setting of tertiary ore deposits, southern Rocky Mountains: Arizona Geological Society Digest, v. 14, p. 199-213.

Livo, K.E., and Clark, R.N., 2002, Mapped minerals at Questa, New Mexico, using airbourne visible-infrared imaging spectrometer (AVIRIS) data–preliminary report: U.S. Geological Survey Open-File Report 02-0026, 13 p.

LoVetere, S.H., Nordstrom, D.K., Maest, A.S., and Naus, C.A., 2004, Questa baseline and pre-mining ground-water quality investigation. 3. Historical ground-water quality for the Red River Valley, New Mexico: U.S. Geological Survey Water-Resources Investigations Report 03-4186, 44 p.

Ludington, S., Plumlee, G.S., Caine, J.S., Bove, D., Holloway, J.M., and Livo, K.E., 2004, Questa baseline and pre-mining ground-water quality investigation. 10. Geologic influences on ground and surface waters in the Red River watershed, New Mexico: U.S. Geological Survey Scientific Investigations Report 2004-5245, 45 p.

McCleskey, R.B., Nordstrom, D.K., Steiger, J.I., Kimball, B.A., and Verplanck, P.L., 2003, Questa baseline and pre-mining ground-water-quality investigation. 2. Low-flow (2001) and

Snowmelt (2002) synoptic/tracer water chemistry for the Red River, New Mexico: U.S. Geological Survey Open-File Report 03-148, 166 p.

McCleskey, R.B., Nordstrom, D.K., and Naus, C.A., 2004, Questa baseline and pre-mining ground-water-quality investigation. 16. Quality assurance and quality control for water analyses: U.S. Geological Survey Open-File Report 2004-1341, 113 p.

Meyer, J.W., 1991, Volcanic, plutonic, tectonic, and hydrothermal history of the southern Questa caldera, New Mexico: unpublished Ph.D. dissertation, University of California at Santa Barbara, 287 p.

Meyer, J.W., and Leonardson, R.W., 1990, Tectonic, hydro-thermal and geomorphic controls on alteration scar formation near Questa, New Mexico: Guidebook - New Mexico Geological Society, v. 41, p. 417-422.

---, 1997, Geology of the Questa Mining District: Volcanic, plutonic, tectonic and hydrothermal history: New Mexico Bureau of Mines and Mineral Resources Bulletin Open File Report 431, 187 p.

Molycorp, Inc., [n.d.], Molybdenum, Questa, New Mexico—History: accessed July 6, 2005 at *http://www.molycorp.com.*

Naus, C.A., McCleskey, R.B., Nordstrom, D.K., Donohoe, L.C., Hunt, A.G., Paillet, F.L., Morin, R.H., and Verplanck, P.L., 2005, Questa Baseline and Pre-Mining Ground-Water-Quality Investigation. 5. Well Installation, Water-Level Data, and Surface- and Ground-Water Geochemistry in the Straight Creek Drainage Basin, Red River Valley, New Mexico, 2001-03: U.S. Geological Survey Scientific Investigations Report 2005-5088, 220 p.

Neal, C., Skeffington, R.A., Williams, R., and Roberts, D.J., 1987, Aluminum solubility controls in acid waters: the need for reappraisal. Earth and Planetary Science Letters, v. 86, p. 105-112.

Nordstrom, D.K., 1982, The effect of sulfate on aluminum concentrations in natural waters: some stability relations in the system Al_2O_3-SO_3-H_2O at 298 K: Geochimica et Cosmochimica Acta, v. 46, p. 681-692.

---, 2002, The Questa baseline and pre-mining ground-water quality investigation [abstract]: Geological Society of America Abstracts with Programs, v. 34, no. 6, p. 51.

Nordstrom, D.K., and Ball, J.W., 1986, The geochemical behavior of aluminum in acidified surface waters: Science, v. 232, p. 54-56.

Nordstrom, D.K., Ball, J.W., Donahoe, R J., and Whittemore, D., 1989, Groundwater chemistry and water-rock interactions at Stripa: Geochim. Cosmochim. Acta, v. 53, p. 1727-1740.

Nordstrom, D.K., and May, H.M., 1996, Aqueous equilibrium data for mononuclear aluminum species, *In* Sposito, G., ed., The Environmental Chemistry of Aluminum, 2nd Edition: New York, CRC Press, p. 39-80.

Nordstrom, D.K., McCleskey, R.B., Hunt, A.G., and Naus, C.A., 2005, Questa baseline and pre-mining ground-water quality investigation. 14. Interpretation of ground-water geochemistry in catchments other than the Straight Creek catchment, Red River Valley, Taos County, New Mexico, 2002-2003. U.S. Geological Survey Scientific Investigations Report 2005-5050, xxx p.

Nordstrom, D.K., and Munoz, J.L., 1994, Geochemical Thermodynamics, Second Edition: Boston, Blackwell Scientific Publications, 493 p.

Nordstrom, D.K., Plummer, L.N., Langmuir, D., Busenberg, E., May, H.M., Jones, B.F., and Parkhurst, D.L., 1990, Revised chemical equilibrium data for major water-mineral reactions and their limitations, *In* Melchior, D.C., and Bassett, R.L., eds., Chemical Modeling of Aqueous Systems II: Washington, American Chemical Society Symposium Series 416, p. 398-413.

Nordstrom, D.K., Roberson, C.E., Ball, J.W., and Hanshaw, B.B., 1984, The effect of sulfate on aluminum concentrations in natural waters: II. Field occurrences and identification of aluminum hydroxysulfate precipitates: Geol. Soc. Am. Ann. Mtg., Oct. 29-Nov. 1, Reno, NV.

Pinder, G.F., and Jones J.F., 1969, Determination of the ground water component of peak discharge from the chemistry of total runoff: Water Resources Research, v. 5, p. 438-445.

Rehrig, W.A., 1969, Fracturing and its effects on molybdenum mineralization at Questa, New Mexico: Dissertation to the University of Arizona, 194 p.

Robertson GeoConsultants, Inc. (RGC), 2000, Interim background characterization study, Questa Mine, New Mexico: report number 052008/6, June, 33 p.

Robertson GeoConsultants, Inc. (RGC), 2001, Background study data report, Questa Mine, New Mexico: report number 052008/12, prepared for Molycorp, Inc., 40 p.

Rubin, J., 1983, Transport of reacting solutes in porous media: Relation between mathematical nature of problem formulation and chemical nature of reactions: Water Resources Research, v. 19, p. 1231-1252.

Runkel, R.L., 1998, One-dimensional transport with inflow and storage (OTIS): A solute transport model for streams and rivers. http://co.water.usgs.gov/otis/: U.S. Geological Survey Water-Resources Investigations Report 98-4018.

Runkel, R.L., Bencala, K.E., Broshears, R.E., and Chapra, S.C., 1996a, Reactive solute transport in streams: 1. Development of an equilibrium-based model: Water Resources Research, v. 32, p. 409-418.

Runkel, R.L., McKnight, D.M., Bencala, K.E., and Chapra, S.C., 1996b, Reactive solute transport in streams: 2. Simulation of a pH-modification experiment: Water Resources Research, v. 32, p. 419-430.

Runkel, R.L., Kimball, B.A., McKnight, D.M., and Bencala, K.E., 1999, Reactive solute transport in streams: A surface complexation approach for trace metal sorption: Water Resources Research, v. 35, p. 3829-3840.

Runkel, R.L., and Kimball, B.A., 2002, Evaluating remedial alternatives for an acid mine drainage stream: Application of a reactive transport model: Environmental Science and Technology, v. 36, p. 1093-1101.

Runkel, R.L., Kimball, B.A., Walton-Day, Katherine, and Verplanck, P.L., 2003, When good tracers go bad: tracer-dilution sausage recipes revealed: Eos Transactions, American Geophysical Union, v. 84, Fall Meeting Supplement, Abstract H51C-1044.

Schilling, J.H., 1956, Geology of the Questa Molybdenum Mine Area, Taos County, New Mexico: State Bureau of Mines and Mineral Resources, New Mexico Institute of Mining & Technology, Campus Station, Socorro, N.M. Bulletin 51, 87 p.

Singh, S.S., 1969, Basic aluminum sulfate formed as a metastable phase and its transformation to gibbsite: Canadian Journal of Soil Science, v. 49, p. 383-388.

Singh, S.S., and Brydon, J.E., 1970, Activity of aluminum hydroxy sulfate and the stability of hydroxy aluminum interlayers in montmorillonite: Canadian Journal of Soil Science, v. 50, p. 219-225.

Smolka, L.R., and Tague, D.F., 1989, Intensive water quality survey of the Middle Red River, Taos County, New Mexico, September 12 - October 25, 1988: New Mexico Health and Environment Department, Surveillance and Standards section, Surface Water Quality Bureau, May, 87 p.

South Pass Resources, Inc. (SPRI), 1995a, Supplemental report: Discussion of the geology, hydrology, and water quality of the mine area, Molycorp Facility, Taos County, New Mexico: Scottsdale, Arizona, February 15, 15 p.

--- 1995b, Progress report of the geology, hydrology, and water quality of the mine area, Molycorp Facility, Taos County, New Mexico: Scottsdale, AZ, April 21, 19 p.

Steffen, Robertson, and Kirsten, 1995, Questa molybdenum mine geochemical assessment: SRK Project no. 09206, Lakewood, Colo., April 13, 44 p.

Stookey, L.L., 1970, Ferrozine - a new spectrophotometric reagent for iron: Analytical Chemistry, v. 42, p. 779-781.

To, T.B., Nordstrom, D.K., Cunningham, K.M., Ball, J.W., and McCleskey, R.B., 1999, New method for the direct determination of dissolved Fe(III) concentration in acid mine waters: Environmental Science and Technology, v. 33, p. 807-813.

URS, 2001, Final report, Molycorp Questa Mine site-wide comprehensive hydrologic characterization report: Denver, March, 95 p.

U.S. Department of Agriculture Forest Service, 2001, Wildland Urban Interface Areas in USDA FS Southwestern Region: Southwestern Region GIS Datasets, accessed July 22, 2004, from the World Wide Web at URL *http://www.fs.fed.us/r3/gis/datasets.shtml#regional*.

U.S. Geological Survey, 2004, Daily Streamflow for the Nation, USGS 08265000 Red River Near Questa, NM, accessed July 22, 2004, from

the World Wide Web at URL *http://nwis.waterdata.usgs.gov/nm/nwis/discharge*.

Vail Engineering, Inc., 1989, A geochemical investigation of the origin of aluminum hydroxide precipitate in the Red River, Taos County, New Mexico, June, 43 p.

Westall, J.C., Zachary, J.L., and Morel, F.M.M., 1976, MINEQL: A computer program for the calculation of chemical equilibrium composition in aqueous systems: Massachusetts Institute of Technology, Department of Civil Engineering, Tech. Note 18.

Western Regional Climate Center, 2005, Historical Climate Information: New Mexico Climate Summaries, Red River, New Mexico (Station Number 297323) accessed January 19, from the World Wide Web at URL *http://www.wrcc.dri.edu/cgi-bin/cliMAIN.pl?nmrriv*.

Yeh, G.T., and Tripathi, V.S., 1989, A critical evaluation of recent developments in hydrogeochemical transport models of reactive multichemical components: Water Resources Research, v. 25, p. 93-108.